Optimization of perovskite/c-Si tandem module for energy yield maximization under real-world conditions

Jacopo Finazzo

Delft University of Technology

TU Delft

Optimization of perovskite/c-Si tandem module for energy yield maximization under real-world conditions

by

Jacopo Finazzo

Student number: 5350174

In partial fulfilment of the requirements for the degree of

Master of Science
Sustainable Energy Technology

at Delft University of Technology

Supervisor:	Dr.ir. Rudi Santbergen
Daily Supervisor:	Manvika Singh
Project Duration:	February, 2022 - October, 2022
Faculty:	Faculty of Electrical Engineering, Mathematics and Computer Sciences

Cover: *Photovoltaic arrays in power plant* by Blue Solar Panel Board
(retrieved as free source from `https://www.pexels.com`)

TU Delft

J. Finazzo, *Optimization of perovskite/c-Si tandem module for energy yield maximization under real-world conditions* (2022).
The electronic version of this thesis report is available at `https://repository.tudelft.nl`.
This thesis work is scheduled to be presented and defended on Friday October 7th 2022 at 10:00 AM CET.

Thesis Committee:	Prof.Dr.ir. Olindo Isabella (Chair)
	Dr.ir. Rudi Santbergen (Supervisor)
	Prof.Dr.ir. J.A. La Poutré (External member)
	Manvika Singh (Daily Supervisor)

The project discussed in this report was carried out with the Photovoltaic Materials & Devices (PVMD) research group. The PVMD group is part of the Department of Electrical Sustainable Energy within the Faculty of Electrical Engineering, Mathematics and Computer Sciences at TU Delft.

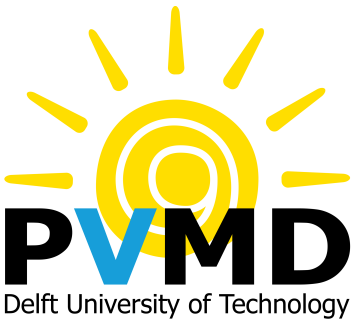

Acknowledgements

The Sustainable Energy Technology program was always my first choice in pursuing a Master of Science in engineering. The idea of being part of the TU Delft prestigious academic environment together with my interest for the topics, represented the perfect union to help shape my career at the service of science and society. Ultimately, my aspiration was to culminate this Master's degree with a thesis work on photovoltaic technology. Given the topics, tools and methodology adopted in this project, this has proven to be a challenging but quite stimulating experience that I've very much enjoyed.

I cannot be grateful enough for the guidance from Dr.ir. Rudi Santbergen and Manvika Singh as my supervisors. Thank you for your professionalism, understanding and for always helping me clear the skies when things seemed to get tricky. My appreciation also goes to Dr. Malte R. Vogt for his help with the PVMD Toolbox, and Stefaan Heirman for the technical help and great brainstorming sessions we've had in the ESP Lab. To the rest of the PVMD group, thank you for letting me be part of the family and for giving me this chance to work on cutting-edge topics.

During these two years, I have had the unique chance to meet so many incredible people. It is hard to explain the beauty of being in a place where everyone brings a part of their diverse past, culture and habit, only to find that we all share the same love for life and for what we are doing. What I have learned from all of you isn't comparable to any teaching in the classroom, and to you, I owe my success and joy from this journey. Among all events that have happened during this experience, the most unexpected yet wonderful one has been to meet Sofia. I feel so blessed to have met such an extraordinarily bright person, and so fortunate to now have you in my life. You have been by my side for my last steps towards this huge goal. My next one will be to do everything I can to make you, my unintended, as happy as you deserve.

To my parents, Alessandro & Raffaella: grazie per avermi reso la persona che sono oggi. Thank you for teaching me to always be kind, curious, to never settle, to always want more. There is no mathematical formula to express the incalculable support you have given me throughout my life and this journey, despite all the difficult times. I only wish one day to be able to give back all that you've given me.

Un giorno venne il Sole e disse: "E così sia.
Se proprio non mi volete, allora me ne vado via.
Io non vi chiedevo tanto, né croci né altare,
ma nemmeno un mondo in cui non possa respirare!"

(Lo Sciopero del Sole - E. "Erriquez" Greppi)

Abstract

Tandem technology has emerged as one of the most promising innovations in the field of photovoltaics. Higher conversion efficiencies than standard single-junction cells have already been achieved. Proving how these laboratory conversion capabilities translate into real-world performance is therefore a main interest drive within the photovoltaic research community.

Typically, photovoltaic device performance is assessed in Standard Test Conditions (STC). For the majority of climates, this is however not representative of actual operating conditions. With the aim of studying potential system applications, the energy yield prediction method adopted in this thesis analyzes tandem technology performance considering real-world conditions. For this scope, the PVMD Toolbox for PV system modeling is employed.

The tandem device investigated in this work is a perovskite/c-Si based structure in a two-terminal architecture. In particular, a TU Delft own poly-SiOx based crystalline silicon bottom cell is utilized in the configuration. This structure is implemented in the Toolbox to carry out Optical simulations from cell to module system level. Operating conditions are introduced through use of the Toolbox Weather and Thermal models. These recreate real-world illumination and climate settings for the selected locations of Reykjavik, Rome and Alice Springs. With an STC-optimized perovskite thickness of 515 nm, the hourly implied photocurrent density of the device is calculated and validated. The j_{ph} annual average is 1.92, 3.34 and 5.01 mA/cm^2 for the three locations, respectively. These values take into account a sub-cells current mismatch loss between 5 and 8% depending on location. To reproduce real-world cell electrical parameters behavior, the variable irradiance and temperature sub-cells J-V curves have been obtained. A poly-SiOx based silicon prototype was tested in laboratory settings and its curves then utilized in simulations after measurements validation.

The module annual energy yield is computed through simulations with the Toolbox Electric model. In terms of specific DC yield, the STC-optimized module delivers 820, 1,427 and 2,161 kWh/kWp/year in the three locations. The power mismatch lowering effect due to the fill factor gain compensates the current mismatch in this 2T configuration, reducing energy mismatch losses. This performance is then compared to a reference single-junction poly-SiOx based silicon module, to show how tandem technology potentially outperforms standard modules differently depending on climatic conditions. The tandem module is also assessed in terms of DC performance ratio (PR), exhibiting values over 0.94 for all three locations. The structure is then real-world optimized by varying perovskite thickness, with the goal of maximizing location-specific energy yield and PR. Slight improvements are obtained for the Reykjavik and Alice Springs locations, where the energy yield increases by few relative percentage points along with PR.

Contents

List of Figures

List of Tables

Nomenclature

Symbols and abbreviations

RES: Renewable energy source(s)

TWp: Terawatt-peak

PV: Photovoltaic

BoS: Balance of system

$CAPEX$: Capital expenditure

$c\text{-}Si$: Crystalline silicon

STC: Standard Test Conditions

$PERL$,$PERC$: Passivated emitter rear locally-diffused/cell

IBC: Interdigitated back contact

SHJ: Silicon heterojunction

$TOPCon$: Tunnel oxide passivated contact

AM: Air Mass index [-]

PSC: Perovskite solar cell

UV: Ultraviolet

$2T$: Two-terminal

$4T$: Four-terminal

$3T$: Three-terminal

$CSPC$: Carrier selective passivated contact

W: Watts

AOI: Angle of incidence [°]

PCE: Power conversion efficiency [-]

eV: Electronvolts

PR: Performance ratio [-]

$LCOE$: Levelized cost of electricity

AC: Alternate current

DC: Direct current

A: Absorptance []

R: Reflectance [-]

T: Transmittance [-]

EQE: External quantum efficiency [-]

DNI: Direct normal irradiance [W/m^2]

DHI: Diffuse horizontal irradiance $[W/m^2]$

GHI: Global horizontal irradiance $[W/m^2]$

J-V: Current (density) - voltage

EVA: Ethylene-vinyl acetate

ARC: Anti-reflective coating

IZO: Indium zinc oxide

S: Sensitivity map

I_{ph}, j_{ph}: Photogenerated current/current density $[A, A/m^2]$

Φ: Photon flux [photon/m^2/sec]

q: elementary electron charge [C]

ESH: Equivalent sun hours []

ASA: Advanced Semiconductor Analysis software

GUI: Graphical User Interface

κ_T: Temperature coefficient [%/℃]

ΔT: Temperature differential [℃]

λ: Wavelength [nm]

V: Voltage [V]

I_0: Saturation current $[A/m^2]$

R_s: Series resistance [Ω]

R_{sh}: Shunt resistance [Ω]

n: ideality factor [-]

$T℃$: Temperature [℃]

k_b: Boltzmann constant $[m^2kg/s^2K^1]$

$W(z)$: Lambert W-function

V_{th}: Thermal voltage [V]

P_{DC}: Direct current power [W]

$(A)EY$: (annual) Energy Yield [Wh/year]

SEY: Specific Energy Yield [Wh/Wp/year]

G_{POA}: Plane of array irradiance $[W/m^2]$

P_{mpp}: Maximum power point [Wp]

η: Efficiency [-]

A_M: Area of the module $[m^2]$

kWh: Kilowatts per hour

1

Introduction

The following Chapter presents the background and postulates behind the research questions of this work. Section 1.1 includes an overview of current trends in the global energy sector and photovoltaic technology. Section 1.2 is a review of crystalline silicon technology and recent high efficiency developments. In section 1.3, perovskite compounds are described along with their potential for photovoltaic applications. The topic of tandem PV technology is introduced in section 1.4 with a review of state-of-the-art structures. In section 1.5 the reasoning behind the research topic of energy yield prediction is given, and the PVMD Toolbox for energy yield simulations is presented in 1.6. Finally, the objectives of this study are defined in section 1.7 and the report structure outlined in section 1.8.

1.1. Background

Professor and geochemist Wallace S. Broecker is recognised to have popularized the term *Global Warming* through his 1975 Science Magazine issue on the topic of climate. It has since then been widely adopted to address the impact of human activities on average surface temperature changes on Earth [1], [2]. The growing demand for fossil fuels to drive our energy-intensive sectors has in fact led to faster depletion of primary energy sources. The consequence to combustibles consumption has been a threatening increase of greenhouse gases concentration in the atmosphere [3]. The climate change issue arises from compounds such as carbon dioxide, methane and nitrous oxide acting as a layer that traps heat radiating from the planet surface, influencing regular climate cycles [4].

Despite the dramatic impact of the SARS-CoViD-19 pandemic on human activities, emerging markets and evolution of living standards are expected to maintain our energy requirements on an upward growing trend [5]. Therefore, transitioning to an environmentally sustainable way of powering our society has become as much of a necessity as it is a challenge. Driven by continuous technological developments and ambitious plans such as the 2016 Paris Agreement, renewable energy sources (RES) have become the main ingredient towards an emissions-neutral

energy system. Among these types of technologies, solar energy is possibly one of the renewable sources with the greatest potential.

Roughly 23,000 terawatts of energy from the Sun reach our planet's surface every year [6]. This suggests that it could be possible to feed a major part of the world's yearly total energy needs through photovoltaic systems and other solar harvesting technologies [7]. In its 5-year forecast between 2020 and 2025, top energy and climate association SolarPower Europe anticipates in fact global installed PV capacity to pass the 1.5 TWp milestone (Figure 1.1) [8]. This is only considering a less optimistic scenario, and mostly shouldered by the fast-growing economies of China and India [8]. In general, photovoltaic technology is the RES technology that has displayed the most impressive learning curve trend. Prices per PV module keep declining with higher experience in terms of installed capacity. Energy produced through PV systems has therefore been exponentially increasing worldwide thanks to economies of scale, but also through exploitation of better performances in different climates and conditions.

Partly affecting this extraordinary technological run is the fact that the rest of the PV system components, the so-called Balance of System (BoS), still accounts for up to more than 50% of total project CAPEX [9]. It becomes evident how crucial it is for research to push towards increasing the system production yield per unit area of the PV array. The goal can be achieved through further enhancing the performance of modules themselves. This includes techniques as single or dual-axis tracking systems, implementation of bi-facial technology, thermal heat-sink systems to prevent overheating and development of higher efficiency modules. Within the latter is where the concept of tandem modules, and therefore the focus of this work, comes into play.

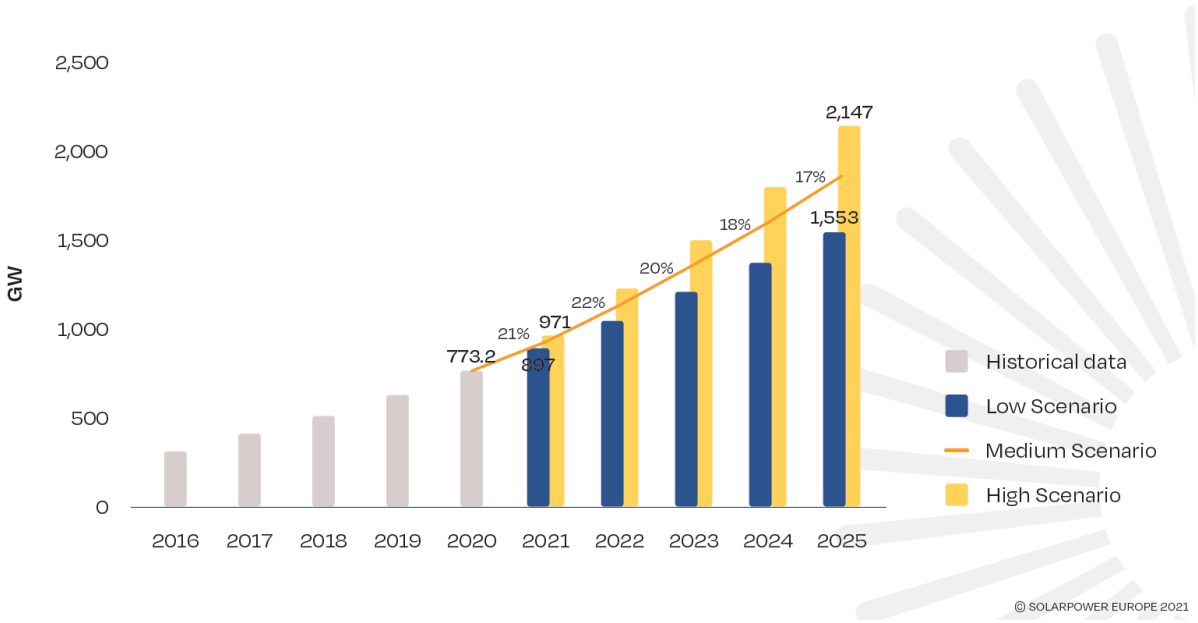

Figure 1.1: Global total solar PV market scenarios (2021-2025) [8].

1.2. Crystalline silicon technology

Silicon is the most widely used material for production of photovoltaic single-junction solar cells. Albeit rare to be found in its pure form, it is one of the most abundant elements in the Earth's crust [10]. Thanks to decades of extensive research and development, nowadays conventional crystalline silicon-based (c-Si) modules found on the market can reach up to about 22% of standard test conditions (STC) efficiency [11]. Through laboratory prototype cells, a record of 24.7% STC efficiency had been held for 15 years by passivated emitter rear locally-diffused cell (PERL) developed by Zhao et al. at UNSW Sidney [12], [13]. Then in recent years, research revolving around silicon heterostructures has allowed to reach a highest value of 26.7% with interdigitated back contact heterojunction cells [14], [13].

What emerges is the trend on investigating different c-Si structures while aiming at higher efficiency. Some of these structure concepts include the mentioned PERL/PERC cells which look at reducing surface recombination losses through emitter passivation and dielectric layering [12]. Interdigitated back contact (IBC) cells on the other hand exploit the idea of avoiding shading losses at the front by moving the metal contact grid structure to the back. Here, localized contacts isolated through p/n diffused and passivation layers are responsible for carrier collection [15]. Considerate attention has also been focused on development of silicon heterojunction cells (SHJ). These cells are based on crystalline silicon wafer which is passivated on top and bottom with hydrogenated amorphous silicon [16]. These higher-bandgap layers are kept as thin as possible to lower parasitic absorption, and are used for carrier collection [16].

Along the lines of the PERC solar cell concept, in recent years a new type of silicon-based structure called TOPCon has emerged. The technology had first been introduced by researchers' work at Fraunhofer Institute for Solar Energy Systems in 2013 [17]. TOPCon stands for tunnel oxide passivated contact, as in the fact that this cell features an additional passivating layer that allows to increase efficiency of the cell by further enhancing carrier collection. The structure of the cell is similar to the PERC concept, however it features a silicon dioxide (SiO_2) layer as the surface passivating layer between the main crystalline silicon absorber and the cell's contacts [17]. In Figure 1.2, a simple standard structure of TOPcon crystalline silicon solar cell is depicted. Typically, for TOPCon cells contacts are made of polycrystalline-silicon (poly-Si) or other variations such as polycrystalline-silicon oxide (poly-SiOx) or carbon (poly-SiCx). These act as carrier selective passivating contact (CSPC) layers. The advantage of using a contact layer such as poly-SiOx for example is that the cell designer can tune its bandgap in order to reduce the parasitic absorption losses by varying the x quantity of oxygen. Another advantage of this type of cells, featuring CSPCs, is that they are compatible with high-termal budget silicon production processes, as the compounds are formed at high temperatures [18]. This allows for a potentially more efficient manufacturing adaptation in the industry. Currently, state-of-the-art TOPCon structures have proved a record efficiency of 25.7% as achieved by Jinko Solar for an n-type cell [19].

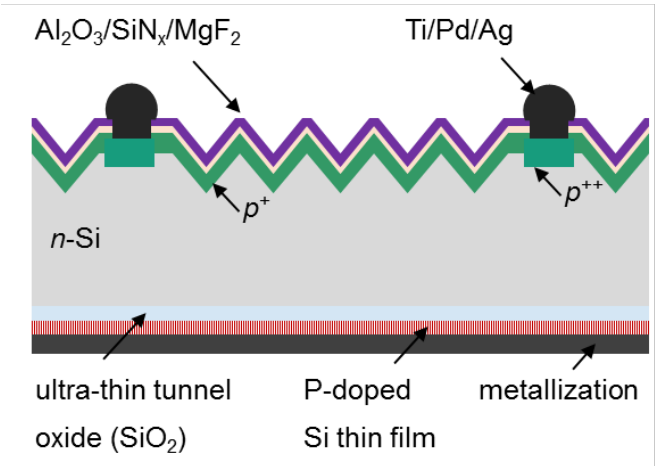

Figure 1.2: Example of standard n-type TOPCon solar cell structure featuring poly-Si CSPCs [20].

Single junction crystalline silicon cells are consequently reaching the theoretical conversion efficiency limit identified by the Shockley-Queisser theory. While this represents a great scientific achievement, it is synonym of a need for technologies and structures that aim at even higher performances for commercial PV applications. The Shockley-Queisser limit strongly depends on the type of spectrum incident on the device, and it was originally elaborated for direct bandgap *p*-*n* semiconductor junctions [21]. For crystalline silicon structures, a 2013 study from Richter et al. had assessed a theoretical boundary of 29.4% under AM1.5 illumination in standard test conditions [22]. However, practically this value is recognised to be around the 27% mark [23].

1.3. Perovskite technology

Perovskite compounds have gained extensive interest in recent years as one of the fastest-emerging materials for photovoltaic applications. PV cell prototypes based on perovskite absorbers have in fact seen a rapid growth in record efficiencies from first values in the range of 2 to 4% between 2006 and 2009, to 25.7% in 2022 [13], [24]. This caps an astonishing progress of more than 600% increased laboratory efficiency in roughly 15 years.

Perovskites are organic-inorganic crystal structures based on the generic form ABX_3. A typical perovskite crystalline structure is depicted in Figure 1.3. A is an organic compound, such as methylammonium ($CH_3NH_3^3$), B is a metal (often lead), while X is a halogen [26]. A and B are the cations where X is the anion. Many advantages have allowed to identify perovskites as a promising material. They are bandgap-tunable and show a steep boundary in their optical absorption profile, but also feature properties such as long carrier diffusion length and low non-radiative recombination [26], [27]. Other than that, they are a potentially very inexpensive type of absorber to fabricate. Perovskites are therefore great candidates to side with crystalline silicon in production of future highest efficiency commercial single-junction PV modules, but also a potentially optimal absorber in silicon tandem applications.

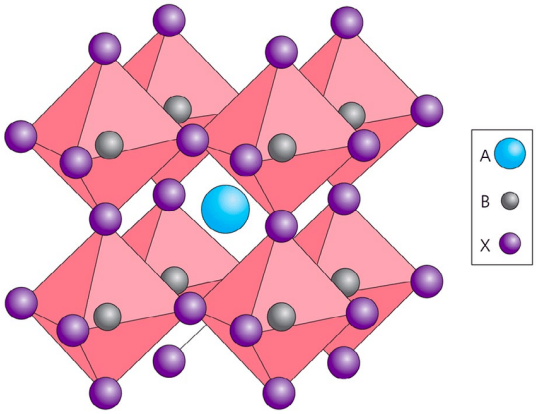

Figure 1.3: Typical perovskite crystal compound structure, with representation of *A*, *B* and *C* elements [25].

Current research on perovskites is focusing on various aspects with the goal of turning the material into an industry-friendly technology. Developers are aiming at substituting lead as a cation, which is currently present in most high efficiency prototypes, to assess toxicity concerns. The biggest challenge is however possibly to solve degradation issues linked to perovskites being exposed to agents and illumination. The compounds are in fact highly sensible to UV radiation, which in time contributes to absorber degradation and losses in efficiency [28]. Proper encapsulation of perovskite-based modules is essential to protect the material from moisture which damages the compound structure [29]. Some state-of-the-art perovskite solar cell (PSC) devices have been developed with a range of few thousands of hours of continuous operation, which is however not yet competitive against established technologies [30]. New approaches and extensive research are therefore needed to improve stability in order to match the industry standard lifetime of PV modules.

1.4. Tandem solar cell technology

The already mentioned Shockley-Queisser limit is the theoretical boundary that defines how any *p-n* single-junction semiconductor-based solar cell is unable to reach ideal conversion efficiencies. In Figure 1.4 such limit is quantified through efficiency balance calculations, resulting from various types of losses. Efficiency is expressed as function of bandgap energy, for a typical AM1.5 spectrum. As it appears, the most relevant losses come from spectral mismatch issues. In particular, *non-absorption* of photons below the cell bandgap and *thermalization* processes in the lattice due to absorption of higher energy photons [31]. Furthermore, additional losses come from issues such as fill factor non-ideality but also voltage, shading and carrier collection losses [31].

1.4.1. Working Principle

The concept of silicon tandem solar cells emerges from the aim of addressing bandgap-related spectral mismatch losses. From a structural point of view, tandems are considered to be the

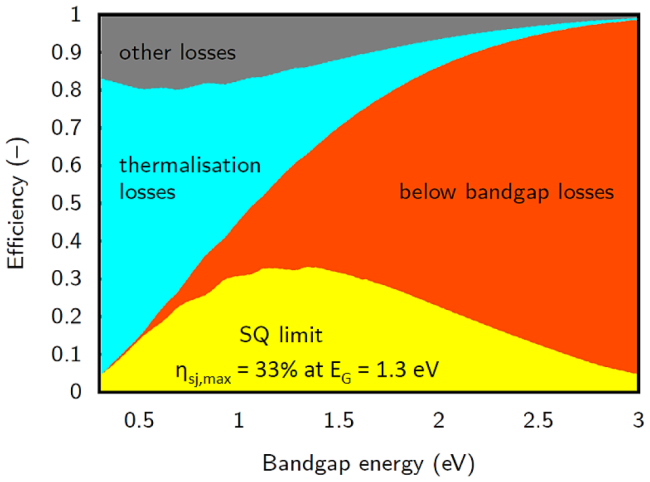

Figure 1.4: Detailed balance limit of efficiency based on the Shockley-Queisser limit [31].

simplest form of multi-junction technology cells, with a two-cell design. The idea is in fact to stack the cells on top of each other, where the top one features a high bandgap and the bottom cell a lower one. This reduces the thermalization issue, thanks to the top cell being able to more efficiently convert higher energy photons, leading to fewer thermal dissipation in the bottom cell lattice. Moreover, the top cell is transparent to photons with an energy below its bandgap, which are absorbed by the bottom cell. Figure 1.5 shows a simple schematic of the working principle for tandem cells. As a result, compared to values for singl-junction cells, the theoretical limit for two-cell tandems can reach up to more than 40% conversion efficiency [32]. Thanks to their attractive potential to increase output without increasing surface area of the cell, tandems have consequently gained substantial attention over the years.

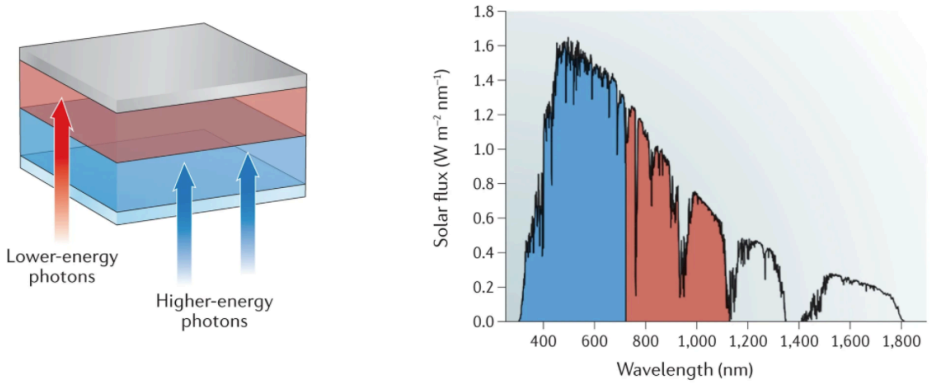

Figure 1.5: Working principle of tandem solar cells with theoretical spectral target of sub-cells [33].

1.4.2. Tandem cell architectures

Tandem solar cells can be structured with different architectures, where connection and optical management between the two sub-cells are the main varying parameters. So other than focusing on materials, tandem research and development highly focuses on optimizing the structure itself. The most commonly studied configurations are the two-terminal (2T) and four-terminal (4T) tandems.

The 2T architecture is a monolithic structure featuring a series connection among the sub-cells. Output voltage is the sum of the two cell voltages, while the current is limited by the lowest photogenerated current in the tandem [34]. The structure is in fact very sensible to irradiance, spectral and temperature variations [35]. Although the easiest configuration to manufacture, 2T requires extensive optimization work in order to maximize the overall photo-current and damper the mismatch issue.

4T tandems on the other hand are unbound from this current limiting issue, as the sub-cells are mechanically stacked and connected in parallel. A greater manufacturing challenge is however proper of this type of configuration, as the two sub-cells need to be optically separated from each other [36]. In other words, the top cell structure and the upper contact of the bottom cell need to be transparent to photons reaching the lower cell, in order to avoid high parasitic absorption losses. This is quite challenging and a solution would be to use an optical splitter such as a dichroic reflector in order to redirect usable wavelengths towards the respective cells [36]. For commercial use, this would however be a very expensive solution.

As of recently, a new interesting type of three-terminal (3T) configuration is being studied. This architecture doesn't require current matching, while still being a monolithic structure and no extra contact layers leading to parasitic absorption are needed [37].

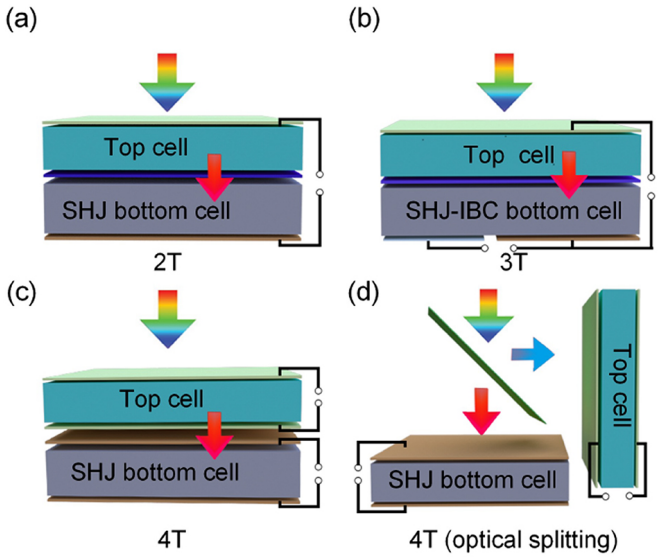

Figure 1.6: c-Si-based examples of tandem architectures: 2T (a), 3T (b), 4T (c) and optically splitted 4T (d) [38]. The c-Si cell used here is a silicon heterojunction structure.

It is ideally meant to combine the advantages of both 2T and 4T architectures. An overview of these different architectures is presented in Figure 1.6.

1.4.3. Sub-cells materials

Different materials to be coupled as top cell have been investigated for silicon tandems with promising STC efficiency ratings. Some of the most common ones include the already introduced perovskite compounds, but also gallium arsenide (GaAs) and indium gallium phosphide (InGaP). Although this work will focus on perovskite-on-silicon tandems, it is noteworthy to point out that all of these combinations with silicon as a bottom cell have already experimentally passed the single-junction theoretical efficiency limit (in both 2T and 4T configurations) [39], [40], [41].

As per the silicon bottom cell, SHJ cells have been the most investigated type in high performance tandems, thanks to their high efficiency and achievable short-circuit current density [42]. Theoretically however any type of c-Si structure could be utilised. As the ultimate goal in tandems research is to push for cost-effective and competitive modules, it is quite relevant to consider cells that would make industrial integration of the technology more viable. This includes types of cells whose production steps are more consistent with affirmed industrial techniques for silicon cell production [43].

Within this dominion, some interest has been placed on the crystalline silicon bottom cells featuring carrier-selective passivating contacts (CSPCs) as introduced in Section 1.2. Placed on both top and bottom of the silicon absorber, CSPCs aim at increasing efficiency of the cell while also being compatible with high-termal budget silicon production processes [44]. CSPC cells currently considered in c-Si tandem applications include the three already mentioned polycrystalline silicon compounds (poly-Si, poly-SiO_x and poly-SiC_x). The main disadvantage of using CSPCs based cells in tandems is the parasitic absorption on top of the c-Si absorber, as an n layer is required for electron collection on the top of the sub-cell. Design optimization techniques are therefore needed to limit such losses. Within this thesis work, perovskite/c-Si tandem cells utilising this type of passivating contact layers are considered. In particular, the crystalline silicon structure implemented in the tandem is a poly-SiOx based c-Si TOPCon cell that was designed and developed at TU Delft [45].

1.5. PV system energy yield

During research and development phase of new and affirmed PV technologies, it is common practice to adopt standard test conditions (STC) to predict module efficiency at beginning of life. STC are an industry standard for fixed operating conditions, and recorded device performances are used to compare technologies' efficiencies and compile datasheets. In detail, standard test conditions include irradiance of 1000 W/m^2 at constant 25°C and zero airflow (no wind) [46]. Moreover, the spectrum considered for illumination of the device is based on

AM1.5 and modules or cells are placed at a normal angle of incidence (90°AOI) [46].

While the STC practice is a great way of establishing a widespread industrial standard for consistent PV cell and module testing, actual world climates can differ sensibly based on a vast number of factors and STC are therefore not representative. During the course of the day, the Sun's position changes constantly and so does the AOI on PV modules. The spectrum and intensity of incident light varies along with the composition of global irradiance, with a high dependence on sky conditions. Other atmospheric factors such as temperature and wind strength fluctuate during the day and this influences the thermal response of the module and its performance. Furthermore, all these conditions feature moving trends according to seasons, resulting in multiple degrees of variability for module performance over the whole year.

Consequently, the reasoning behind performing energy yield calculations for PV systems is justified. Yield predictions take into account generation fluctuation over the year and result in forecast energy output for specific climate areas around the globe. Assessing the energy yield of PV systems during development is of utmost importance for both research and economical motivations. From a financial point of view, elaborating on the expected yearly output can make the difference between an economically feasible project and one that would bring losses. This is very relevant during the growth phase of innovation technology and benefits ease of integration for PV on the grid. Secondly a real-world, location-specific performance analysis can be a much more reliable and application-accurate way of assessing PV modules' potential. This is especially significant when comparing new and different technologies or architectures. For emerging PV tech that aim at commercialisation such as tandems, this type of focus brings many advantages. The modules can be optimized with the aim of delivering maximum yield in real-world conditions. Confronting yields and performances from different areas on the planet can then help define how the new technology can target the market and eventual location-specific design foresight.

1.5.1. Tandem solar cells energy yield research overview

In this subsection, a brief overview of the status quo on energy yield studies for on-silicon tandems is presented with reference to relevant literature. Tandem structures have already been proven to be more efficient in standard test conditions than single junction cells. Researchers are therefore aiming at demonstrating whether this means that a higher energy output can also potentially be obtained in terms of real-world performance.

M. Hörantner and H. Snaith have studied the predicted energy yield of metal-halide perovskite absorbers on top of a silicon heterojunction cell. Their approach is based on optimisation of the tandem analysis under varying illumination conditions for different locations. The objective, is to set ground for guidance of real-world yield design of tandems. Structures considered are the monolithic 2T and stacked 4T. For both architectures, they first elaborate on optimal thickness and bandgap of the perovskite top cell in order to maximize power conversion efficiencies (PCEs) with AM1.5 spectrum. Due to high currents delivered by the SHJ cell, they

opt for a maximum perovskite layer thickness of 1.2 μm, with bandgaps of 1.65 eV and 1.8 eV for 2T and 4T configurations respectively. The findings show that at all locations, the cells are able to deliver a sensibly higher yield than both perovskite and SHJ cells alone. In the best case, the best efficiency-optimized tandem is able to deliver up to 30% higher yield than its single junctions counterparts. Moreover due to spectral variations in infrared richness and blue shift diffuse radiation depending on typical local sky conditions, they also elaborate on location-specific perovskite bandgap adaptation. When compared to the AM1.5 spectrum optimization, they show interesting results on relative yield gains when modifying the bandgap to a real-world optimal value, especially for a fixed mounting system and 2T configuration [47].

H. Liu et al. on the other hand offer a comprehensive view on silicon-based tandems, evaluating performance of different structures with different top cells. Their analysis is relevant in terms of studying many different types of module architectures and showing their potentials and drawbacks in wider geographical areas around the globe. The structures considered are mainly GaAs-Si and perovskite-Si in 2T, 4T module configurations as well as 3T, areal matched (AM) and voltage matched (VM). Compared to the single-junction version of all respective absorbers considered, tandem STC efficiencies reach much higher values. Then, they consider the cell performance ratio (PR) to assess the system real-world efficiency relative to STC. Four specific climate zones based on NASA satellite data are assumed for field simulations, and tandems are evaluated based on their average performance. Their conclusion is that 2T (and the similar AM) structures are in general very sensible when moved around the globe and may require location-specific design. Their current-matched requirement results in lower than expected performance ratio in areas where irradiation is higher. 4Ts are not as heavily affected by different climates and are more uniform in terms of PR. On average they also output higher yield than the 2T architecture. This is however not valid specifically for perovskite-on-silicon tandems. Even if their PR results lower in 2T, overall expected yield is still higher. Another finding is that 3T and the similar VM are very promising for real-world applications. They can increase performance and reduce structure complexity compared to 4T [48]. This research work will serve as main reference for the PV system performance analysis carried out in Chapter 4.

1.5.2. Energy yield prediction softwares and models

As the analysis of energy yield is a relevant part of both research and project practices, several yield prediction models have been developed in past years by research institutes. Such softwares are able to compute yearly yield starting from the design of the PV system itself and local atmospheric conditions. They can be based on different approaches and algorithms, and some of the most notable ones are presented below.

PV Syst

PV Syst is possibly one of the most popular softwares for system design and performance prediction. It has been developed at the University of Geneva by Swiss engineer M. Villoz and physicist A. Mermoud. It's a software meant for engineers, architects and research institutes. It offers a quite comprehensive package to design PV systems starting from requirements. It

allows for different PV module technology selection and BoS elements integration such as the inverter but also storage. Weather data utilised for yield prediction is retrieved from Meteonorm, and shading scene to take into account surroundings and horizon can also be implemented. Finally, the package is completed by a system ageing prediction feature and a total economic evaluation of the project. As of recently, bifacial technology has also been included within the software's PV module database. However, mostly conventional types of module technologies are available so the software is not suitable for studying emerging cell types [49].

System Advisor Model

The System Advisor Model (SAM) has been developed by the U.S. Department of Energy's National Renewable Energy Laboratory (NREL) as an open source software. It is a techno-economic software utilised to model different types of renewable energy systems, such as PV but also wind power, biomass and fuel cells. It is meant as an aid for decision-making processes among project engineers, managers and policy analysts. The SAM provides with system performance predictions and LCOE estimates, mostly for utility, grid-tied projects. As with PV Syst, this software doesn't allow simulation for innovative PV technology, and it is not used for off-grid or hybrid systems [50].

Hybrid Optimisation Model for Electric Renewables

HOMER is a software meant for continuous optimization of renewable system configurations, including PV technology, wind energy and other auxiliary generating units (such as gensets). As the SAM, it was developed by NREL but later turned and optimised by HOMER Energy. It is used for micro-grid projects in which a combination of the above technologies is employed. However, again it still only features conventional silicon PV modules [51].

1.6. The PVMD Toolbox

The PVMD Toolbox is a Matlab®-based simulation tool developed by the Photovoltaic Materials and Devices research group at Delft University of Technology. The idea behind the Toolbox is to create a comprehensive model to correctly predict energy yield of all types of photovoltaic devices, including emerging technologies, from cell level to system level [52]. Its development has seen continuous joint effort from researchers within the PVMD group as well as MSc alumni including E. Garcia-Goma, J. Extebarria, Z. Wang, A. Nour El Din. The version of the Toolbox employed within this work is the latest update.

1.6.1. Structure of PVMD Toolbox

Figure 1.7 represents the structure of the Toolbox. As shown, the core of this software is made of five models that simulate the Optical, Thermal and Electrical behavior of the PV cell and module. These three main blocks are introduced below. As of recently, it has also been completed with a conversion model which features system simulations with cabling and inverters

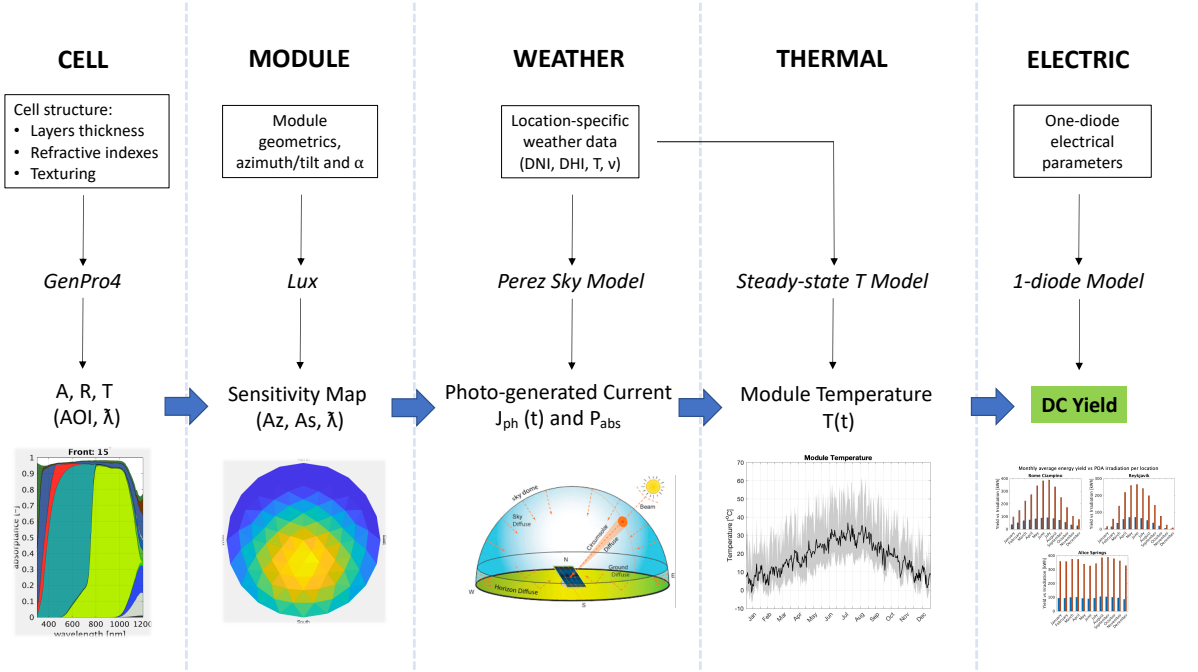

Figure 1.7: Structure of the PVMD Toolbox for energy yield calculations.

for AC yield prediction which however falls out of the scope of this work.

1. Optical simulation

Cell

At cell level the Toolbox is based on the *GenPro4* software, the model for simulating interaction of light radiation in solar cells developed by Santbergen et al. Many of the available optical simulation softwares are based on either wave or ray optics. While wave optics models solve Maxwell equations rigorously considering the electromagnetic wave nature of light, ray optics approximates light as rays and allows for ray tracing technique simulations. *GenPro4* is a model where both ray and wave optics are combined allowing to accurately simulate the external quantum efficiency (EQE) of solar cells. Outputs of the simulation are therefore the spectrally and angle resolved absorptance (A), reflectance (R) and transmittance (T) of the device as function of the wavelength. The implied photocurrent at STC can also be retrieved. *GenPro4* can in fact be used for STC optimization and current matching technique applications which is very relevant for this work [53].

In *GenPro4* the cell is represented as a 1D structure, where each layer is defined in terms of thickness and complex refractive index ($n + ik$), from top to bottom. For flat interfaces between layers, the software uses the net-radiation fluxes method for calculating R, A and T. For surface-textured layers, *GenPro4* uses the scalar scattering model developed by Jager et al. and extends the net-radiation method by subdividing the angular intensity distribution hemisphere in sub-fluxes [53], [54].

When defining the structure of the cell, the software lets the user declare the stack elements as both normal *layers* or *coatings*. This is quite relevant as it allows to correctly take into consideration the effect of wave interference. When the element is defined as *layer*, it is processed as *incoherent* sub-stack (non-lattice matched) and therefore interference effect is not considered. This happens when the thickness is higher than the coherence length of the incident radiation, or $> 1\mu$m [53]. *Coatings* are *coherent* elements, usually at the interface between incoherent layers, and for them the software computes interference. The advantage of *GenPro4* is that it can simulate virtually any type of cell structure and is therefore suitable for studying emerging technologies such as tandems.

Module

With the module part, the user is able to define the structure and geometrics of the PV module, made up of the implemented cell type. As input for the Toolbox, it is required to state details such as the module cell matrix (rows and columns), size of each cell but also module height, azimuth and tilt. Values for albedo (α) and module spacing also need to be declared, to take into account reflection from surroundings. The module simulation is based on the *Lux* ray-tracing software developed by Stantbergen et al. The ultimate goal of this model is to create a *Sensitivity Map*, which is the module surface's sensitivity to incident light as function of the hemispherical angle of incidence [55]. In other words, sensitivity could also be described as a tool to demonstrate how the module responds to the incident spectrum. This map is then plotted over a 2D representation of the sky dome as heat map. The sky dome hemisphere is discretized in triangular sky elements, where each element represents one direction of the light. According to geometry, surroundings and positioning of the module we are able to study to which irradiance directions the system is more sensible.

To do so, the ray-tracing simulation is performed by illuminating the module from every of these considered direction, and all reflections are taken into account. The Monte-Carlo ray-tracing approach is used for this task. The number of rays per direction has to be declared by the user, with a higher number providing more accurate results however with longer computational time. When a ray has either been totally absorbed by the cells or is escaping to infinity, the software stops tracking it. The represented sensitivity per each sky element is then expressed as ratio between absorbed power per unit cell area (I_{abs}) and the intensity of the ray (I_{dn}) [55]. For a free-horizon simulation of a single module, the output can be an average cell sensitivity for the whole module with good accuracy. In case we are interested in studying shadowing of certain cells due to surroundings, the software is now also able to run individual cell sensitivities to avoid hard approximations with an average map [56].

Weather

The Weather part is an irradiance model which allows to compute the incident irradiance on the PV module and output absorbed power per cell and incident photon flux. This is achieved through combination of the already obtained module Sensitivity Map, and a *Sky Map* [55]. To create a Sky Map, the toolbox uses the Perez irradiance model whose inputs are the DNI, DHI

and GHI values obtained through measurement arrays or Meteonorm. From that, it is able to generate the luminance distribution of sky diffuse and circumsolar light, which together with direct irradiance constitute the whole Sky Map [57].

Since input for reconstruction of the Sky Map can be real measured sets of data or Meteonorm-retrieved data, this model allows for simulation of the PV system in real-world conditions. The absorbed power from the Weather output is later used in the Thermal model, while the photon flux per each absorbing layer is used to calculate the hourly implied photocurrent. Since the work of Garcia-Goma, the model is now also able to simulate non-free horizons and take the *Shading Factor* into account [58].

2. Thermal

The absorbed power and photocurrent calculated through the Weather model are utilised as inputs for the Thermal model, along with atmospheric conditions data measured or retrieved from Meteonorm. The simulations allow to estimate the module operating temperature of the module through a steady-state, hourly-based model. Such temperature is necessary to compute the effective performance of the system.

In particular, the model on which the Toolbox bases its temperature calculation is the Fluid dynamic model [59]. This model is based on parameters that are not empirical and therefore it can include the effect of variable cell properties depending on temperature of operation. This allows simulation of technologies that have not yet been fully developed or commercialized, for which empirical parameters such as temperature coefficients are not known. For single module temperature calculations, the model employs the energy balance equations between front glass, solar cell and rear glass [59]. Inputs are ambient temperature, wind speed, module mounting characteristics and absorbed irradiance on the module. The model takes therefore into consideration the thermal heat transfer and parameters for radiative heat transfer, at all simulation time steps. To visualize the results of the simulation, the Toolbox produces a plot which represents the average module temperature throughout the year, along with daily minimum and maximum peaks.

3. Electrical

The Electrical part is the last step in calculation of the PV system DC yield. Inputs obtained from previous models are the module temperature and the photo-generated current. The Electrical part is based on a lumped-elements model that aims at obtaining the current-voltage curves of the module for each hour of the year. This is achieved through implementation of the Lambert W-Function and the one-diode model parameters, which are irradiance and temperature dependent, of the unit cell(s) utilised in the simulation [60], [59]. When dealing with a tandem structure, the Electrical model reconstructs J-V curves from the one-diode parameters separately for each sub-cell and then builds the tandem characteristic depending on its architecture.

Module temperature and one-diode parameters are used to assess the actual module performance under realistic atmospheric conditions. Then, along with the photo-generated current, the module external parameters are computed and maximum power point for DC hourly power output calculations, obtained [56], [60]. The annual DC yield can then be derived from this result as sum of the power output per each hour.

1.6.2. Limitations of the Toolbox

The Toolbox is a quite comprehensive tool that can actually be considered an unique software for complete PV system performance simulations. If compared to other established softwares as the ones previously presented, the many advantages brought by the extensive implementation of each part of the Toolbox makes it an innovative method for studying potentially any type of technology including emerging new structures and materials. The use of this Toolbox for the computation of the annual energy yield is therefore what differentiates the work conducted in this thesis (and at TU Delft in general) on tandem technology performance prediction from other studies. However, the models used can still present a few limitations.

One of them can be identified within the Weather part, and it is linked to a simplification of the spectral reconstruction system adopted in the irradiance calculations. Such reconstruction of the incident spectrum is based only on the sun position and altitude from which the AM index can be obtained. The Weather model uses in fact this data, based on the SMARTS spectral model [59], to compute the composition of the spectrum of the incident irradiance or photon flux. Future versions of the Toolbox will strive to improve the spectral definition in a more complex and detailed way.

Still within the Weather part, it is worth pointing out that for sky reconstruction the Perez model is also a more simplified one if compared to other models such as the Preetham model, which can perform better in the case for example of tandem structures simulations. This model can in fact take into account many extra factors which are ignored by the Perez model, such as the effect of atmospherical particles on the spectral composition of diffuse light. A first implementation of this model has been delivered by previous TU Delft MSc student M. Jayan which included turbidity and scattering effects for a more realistic rendering of the sky. It is however yet to be included in the Toolbox [61].

Then, the method of calculating module DC power output through its J-V curves obtained thanks to the one-diode model parameters is dependent on the accuracy of the way the latters are calculated. As it will be explained in Chapter 3, these cell parameters are currently extracted through a quite simple method whose validity can depend on many factors such as cell's J-V curve data availability and a few physical assumptions. Although it leads to reasonably accurate results with much lower computational effort required, new methods can be explored and included in the case of a study which requires a more granular degree of precision. Moreover, the parameter extraction model is still not currently included in the Toolbox and is

therefore not part of the user interface experience offered by the Toolbox.

1.7. Thesis objectives

In this section, the objectives of this work are finally presented. The main goal of this thesis is to predict and analyse the energy yield of a perovskite/c-Si tandem module in real-world conditions, and use these results to optimize the tandem structure in order to deliver the highest energy yield in specific locations around the globe. This is achieved through use of the PVMD Toolbox presented above.

Hence, the main research goal of this paper is defined as:

Optimization of perovskite/c-Si tandem module for energy yield maximization under real-world conditions

As sub-objectives for this work in support of the main research question, the following are defined:

1st sub-objective: within the first sub-objective, the aim is to implement the tandem structure as it will be defined and described in Chapter 2 on the PVMD Toolbox. Such implementation will lead to performing Optical and Thermal simulations of the device with the goal of setting the base for a comprehensive real-world system performance and energy yield prediction analysis.

2nd sub-objective: the bottom sub-cell utilised in this tandem structure is a poly-SiOx based solar cell that has been developed at TU Delft. The utilisation of this new type of cell is a particular trait of this study focusing on perovskite/c-Si tandem technology. Thanks to the physical availability of the device, an experimental process involving measurements on the real prototype has been carried out. The goal of this objective is to measure the cell's behavior for variable operating conditions, namely variable irradiance and temperature, in order to obtain its J-V curves for cell parameter extraction purposes. As the results of this extraction method serve as input for energy yield calculations, using real empirically-obtained parameters gives more realistic results of the tandem performance in real world conditions. This sub-objective therefore presents a quite singular link between experimental and simulation work, showing the innovative approach to energy yield modeling of this study.

3rd sub-objective: directly linked to the main goal of energy yield maximization, is the sub-objective of evaluating the energy yield performance of the tandem structure in real-world conditions. This is achieved by comparison of the performance to its standard test conditions behavior as well as against established a single-junction technology, in particular c-Si. Three locations scattered around the globe will be considered for this analysis, to provide a comprehensive idea of the technology's behavior in different parts of the world with variable climatic

conditions.

1.8. Thesis outline

The following section outlines the structure of this report in order to lay down the process followed to obtain the final objective of the project.

In Chapter 2 the structure of the tandem module is presented and analysed in higher detail with the aim of implementing it on the PVMD Toolbox. Therefore, simulation results obtained through the Toolbox for the Cell, Module, Weather and Thermal models are included. This aims at answering sub-question one.

Chapter 3 discusses the second sub-objective of this work. Within this Chapter, the experiment carried out for J-V characterization and parameter extraction of the c-Si bottom cell utilised in the tandem is presented. The characterization for the perovskite sub-cell is also discussed, as result of J-V simulations with ASA software.

In Chapter 4, the background behind the simulation with the Toolbox Electric model is explained. This also justifies the link between the experimental data gathered in Chapter 3 and the simulation work. Consequently, Electrical simulation with the Toolbox is ran in order to obtain first tandem module DC energy yield results for all locations considered, partly answering sub-question number three. A brief overview of considered DC losses is also provided.

In Chapter 5, the tandem energy yield performance is compared to the single-junction c-Si poly-SiOx based cell that is used as bottom cell in the tandem. The goal is to observe differences with an established type of technology. Then results of energy yield simulations are discussed in terms of DC performance ratio analysis. The system is studied for different cell structure variations with the aim of maximizing the performance of the module over the year at each of the locations. This Chapter aims at completing the discussion of sub-objective three along with answering the main research question of this thesis.

In Chapter 6, conclusions of this report are drawn where the answers to the main research question and relative sub-questions are summarized, along with recommendations for further studies on the subject.

2

Implementation of tandem structure in the PVMD Toolbox

This Chapter presents results from the first part of this work, which is the implementation of the tandem structure for optical and thermal simulations on the PVMD Toolbox. The outputs of these models are utilised within the Electric part and constitute the basis for energy yield calculations. In section 2.1, the structure of the tandem solar cell is presented in terms of architecture and layers composition, including details on the sub-cells adopted. Then, in section 2.2 this structure is first implemented on the GenPro4 software for Optical simulation of the single cell, then the module is constructed to obtain its illumination Sensitivity Map. Consequently, weather data from three specific locations around the globe retrieved from Meteonorm is employed to calculate plane of array irradiance and absorbed photon flux. This part contains a validation of results in terms of simulated photocurrent density values. Ultimately, hourly temperature of the module is computed through the fluid-dynamic model.

2.1. Structure of tandem solar cell

In this Section, the structure of the tandem cell on which the PV module is based upon is defined. The specifications, such as layers implementations, thicknesses and materials refractive indexes, for each element constituting the cell stack are subsequently implemented on the GenPro4 software to run the optical simulation.

2.1.1. Cell architecture

The perovskite/c-Si tandem structure utilised for the simulation is based on a previous study performed by M. Singh et al. [18]. It is a monolithic, mono-facial integrated 2T architecture. As explained in the previous Chapter, this type of architecture is the easiest to manufacture as it requires less complex processing steps [62].

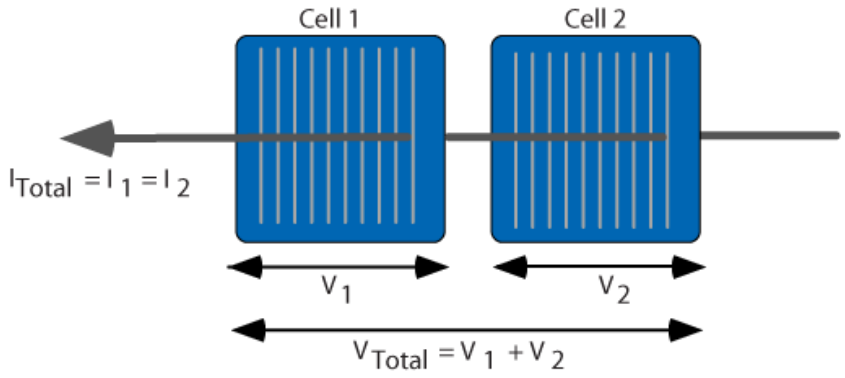

Figure 2.1: Demonstration of series connection between sub-cells in tandem structure. The resulting tandem V_{OC} is equal to the sum of the single cells' open-circuit voltages, while the output I is imposed by the lowest photocurrent in the series [63].

The resulting tandem cell is a series connection between the top perovskite (*cell 1*) and bottom c-Si (*cell 2*) sub-cells. A simplified representation of the electrical structure is shown in Figure 2.1. Due to the series connection, the total voltage output of the cell is the sum of the two single cells voltages. On the other hand, the photocurrent of the tandem cell is forced to the value of the lowest produced sub-cell photocurrent. This is represented as a typical J-V curve composition in Figure 2.2. To reduce power output losses, it is therefore necessary to optimize this structure. This can be done in standard test conditions by varying the thickness of one (or both) the absorber layers in the tandem. For constant irradiation, angle of illumination incidence, spectrum and temperature, the so called *current matching* optimization procedure is carried out, where the photogenerated currents of the two cells are matched [64]. This obviously sensibly reduces the current output capabilities of one or both sub-cells but it allows for maximization of the total tandem photocurrent, which is what is of interest in this case.

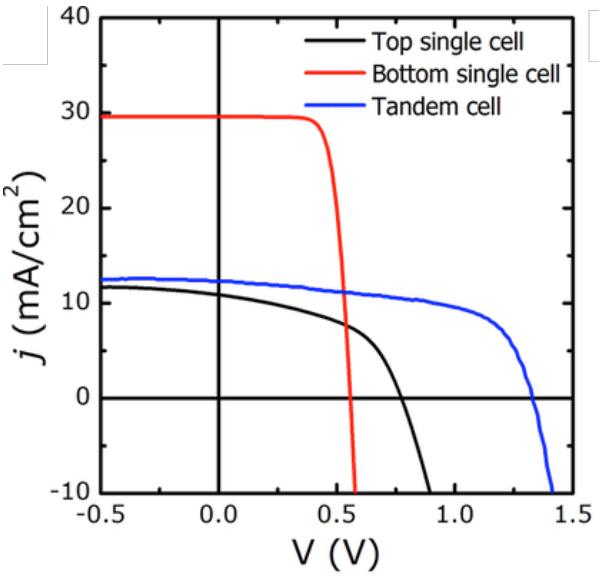

Figure 2.2: Example of tandem J-V curve composition from single top and bottom cell J-V curves. [63].

In real-world conditions it is however not always possible to maintain the current matching status and we incur into *current mismatch losses*. In fact, depending on factors such as irradiance, spectrum and angle of incidence variations during the course of the day, either the top or bottom sub-cell can deliver a higher or lower current and this scales down the resulting tandem j_{sc} if compared to the j_{sc} at STC. Even though this negative effect impacts the tandem 2T structure, in practice it is demonstrable that the mismatch loss is compensated by an increase in fill factor of the tandem J-V curve [65]. This means that out of a lower performing cell in terms of photocurrent, a more ideal value of maximum power point can be extracted. Fill factor is in fact minimized under current matching conditions and grows with the mismatch. This is why maximizing the current output by matching absorbers currents doesn't necessarily mean optimization of the tandem power output [64]. This topic will be further discussed in Chapter 4 as it is part of the electrical behavior of the tandem module.

2.1.2. Coating, encapsulation and back reflector

As the cell will implemented in a module, it is encapsulated with glass and ethylene-vinyl acetate (EVA) on both front and back sides. Although EVA is one of the most widely adopted encapsulants in photovoltaic cell manufacturing, a tandem structure featuring a perosvkite absorber may actually require a much more isolating material. This is because the cell needs to be kept dry from moisture, which would otherwise damage the perovskite absorber. Current research has been studying the application of *polyolefin*, an alkene polymer belonging to the class of synthetic resins that is expected to more efficiently protect the tandem cell from moisture infiltration [66]. However as this study does not focus on tandem manufacturing, the classic EVA method is adopted and its known optical characteristics utilized in simulations.

Over the top glass sheet, a thin and flat anti-reflective coating (ARC) is applied. It is common practice for commercial modules to be completed with front ARC in order to reduce reflective losses [67]. For this cell, magnesium fluoride (MgF_2) is employed thanks to its high transparency properties for wide wavelength intervals [68]. Since this material is not extremely resilient in outdoor applications, a type of MgF_2 with a refractive index close to other utilized anti-reflectants with more resistant coatings (i.e. silica) can be utilised at the front of the cell [69]. Although actually implemented at module level in manufacturing, ARC and glass/EVA encapsulation are considered here at cell level in order to evaluate their impact on cell optical behavior and light absorption. This is achieved through inclusion of these layers in the GenPro4 software.

Below the crystalline silicon cell, silver (Ag) is utilised as back-reflector to increase absorption in the bottom cell and reduce overall transmittance. Despite the quite wide thickness to ensure efficient reflection makes Ag technically an incoherent layer, its positioning in the stack allows GenPro4 to correctly simulate its behavior as both *layer* or *coating*, without any relevant proven difference. For simplicity and ease of simulation, Ag will therefore consistently be considered as lower *coating* to the bottom cell. For all materials employed in this tandem structure, Appendix A reports thicknesses and references for complex refractive indexes utilised to run

GenPro4.

2.1.3. Perovskite top sub-cell

The perovskite sub-cell features the $(Cs_{0.5}(MA_{0.17}FA_{0.83})_{0.95}Pb(I_{0.9}Br_{0.1})_3)$ compound as absorber layer. This is based on the monolithic tandem cell example from Sahli et al [70]. The 1.63 eV bandgap of this absorber is however blue-shifted by 20 nm in order to match the optical profile of the higher efficiency sub-cell from Zhang et al. [71]. The thickness of this absorber has been already optimized for highest STC current-matched performance by Singh et al. to a value of 515 nm for a 2T architecture. Simulation results comparing different perovskite thicknesses will be presented in further sections to show how this optimization leads to the highest possible resulting tandem photocurrent.

The top of the perovskite absorber is decorated with indium zinc oxide (IZO) as electrode but also ultra-thin tin oxide (SnO_2) and the fullerene C_{60}. The latter serves as electron transporting layer while the SnO_2 is a protective layer. As hole transporting layer, an ultra-thin organic coating of the widely studied Spiro-OMeTAD material is utilised [69], [72]. The tunnel recombination junction (TRJ) between the two sub-cells is realized with a $p+/n+$ hydrogenated nano-crystalline silicon stack as it is implemented by Sahli et al. [70]. Both these layers combined are 20 nm wide. Texturing is also employed on the coating layers of the top cell to simulate light trapping mechanisms and increase j_{sc}. The texturing technique is currently feasible in manufacturing of perovskite/c-Si tandems with 2T configuration. In 4T structures, it is still challenging to fabricate a textured perovskite top cell [18]. Each texturing pyramid element has a size of 5 um and a base angle of 52°.

2.1.4. Crystalline silicon bottom sub-cell

The bulk in the crystalline silicon bottom cell is 280 μm thick and implemented as layer on GenPro4. Its refractive index properties are based on Werner et al. [73]. As mentioned already, in this study a poly-SiOx based c-Si cell is employed. The absorber is therefore completed with carrier-selective passivating contacts, made of poly-silicon oxide. N-doped CSPC is placed on top and p-doped CSPC on the bottom. In order to recreate the diffusion effect between doped and un-doped regions in the silicon bulk, a diffusion effect of both n and p is implemented on GenPro4 [18]. The diffusion profile is achieved through an extinction coefficient which is wavelength-dependent and function of the free-carrier absorption coefficient. Then, below the c-Si absorber and the p poly-SiOx CSP contact, a new layer of tin oxide is employed. Texturing is also implemented in the silicon cell to maximize the j_{sc}. A cell with this type of structure has been physically designed and created at Delft University of Technology. The produced cell therefore serves as reference for optical and electrical behavior simulations discussed further ahead in this report.

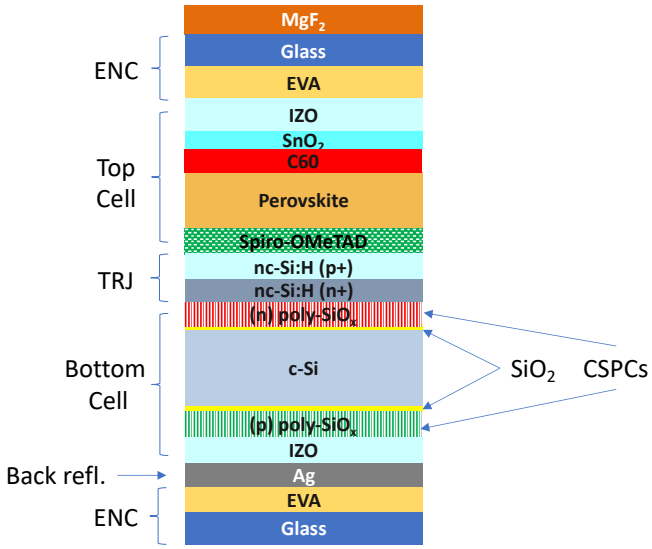

Figure 2.3: The perovskite/c-Si tandem cell structure as implemented in this study (Figure re-adaptation from [18]).

2.2. Tandem simulations with PVMD Toolbox: from Optical to Thermal

2.2.1. Cell simulation

After implementing the cell stack structure as described above on GenPro4, the software is ran to obtain A, R and T profiles. This simulation recreates the STC settings when the cell is laying flat with respect to incident light. The A, R, T functions are drawn according to varying wavelength. The number of rays considered in the simulation is maximized to 1000 and the wavelength step interval is reduced to a minimum of 10 nm. This increases accuracy of results, although it also affects computational effort inducing longer simulation times. The software runs optical simulations from variable incident light angles (up to 87°) in order to obtain photocurrent values as with variable real-world AOIs.

Through the absorptance profile under AM1.5 spectrum, the absorbed photons function per each element of the cell stack is obtained. By integrating it, GenPro4 calculates the implied STC photocurrent density, and consequent implied photocurrent density of the tandem. Moreover it is possible to study the effect of parasitic absorption in non-generating layers. For this structure, the layers stack was previously optimized in terms of thickness to reduce parasitic absorption losses by Singh et al. [18].

In Figure 2.4, the absorptance profile at STC is shown as function of the wavelength, for each

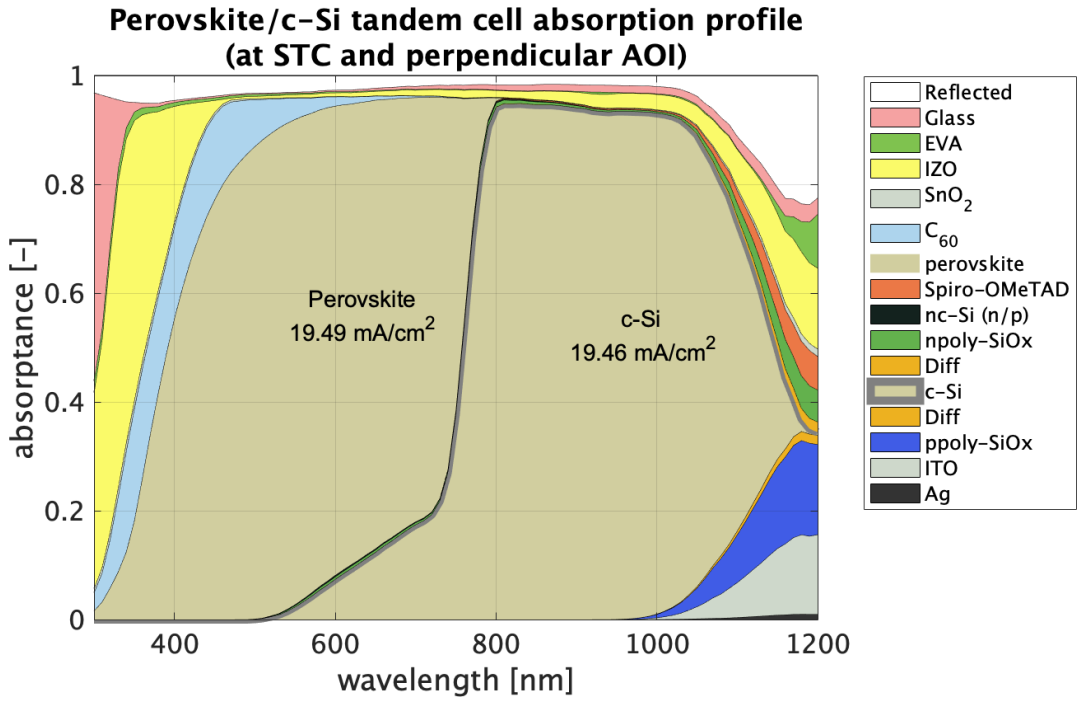

Figure 2.4: Absorptance profile for the current-matched perovskite/c-Si tandem stack with corresponding values of photocurrent.

layer and coating in the structure. In the ultraviolet region, most of the radiation is absorbed by the glass and IZO layers. The perovskite profile is also smoothed by the presence of the C_{60}. As expected we also have parasitic absorption from the CSP contacts in the silicon cell that increases with higher wavelength. In particular, the front-facing n-type poly-SiOx CSPC features the lowest possible thickness aiming at avoiding high parasitic losses at the front side. The bottom-facing p-type contact has a much more emphasised parasitic absorption in the infrared region where the absorption function of c-Si reaches a cut-off.

M. Singh et al. demonstrated that for this structure, the implemented 515 nm perovskite layer allows for highest photocurrent matching with the c-Si cell at STC. In particular, the optimized perovskite thickness allows a matched value of 19.5 mA/cm^2 for this 2T tandem. This has also been validated in this study. Figure 2.5 allows to compare how varying the thickness of the perovskite absorber affects current generation in the cells and the tandem. At 515 nm it is clearly visible that the two sub-cells photocurrents are closely matched. As introduced earlier, this is however not valid anymore when the incident illumination angle and spectrum vary from the ideal STC at 0° AOI and AM1.5 ones respectively. This factor will become relevant when considering the cell's behavior under real-world conditions.

2.2.2. Module simulation

After simulating the tandem at cell level, the structure implemented in GenPro4 is used as base to form a 12-by-6 cells module sample. The single cells dimensions are set with a 15.675 cm x 15.675 cm squared shape. Including cell spacing and borders, the total area occupied by

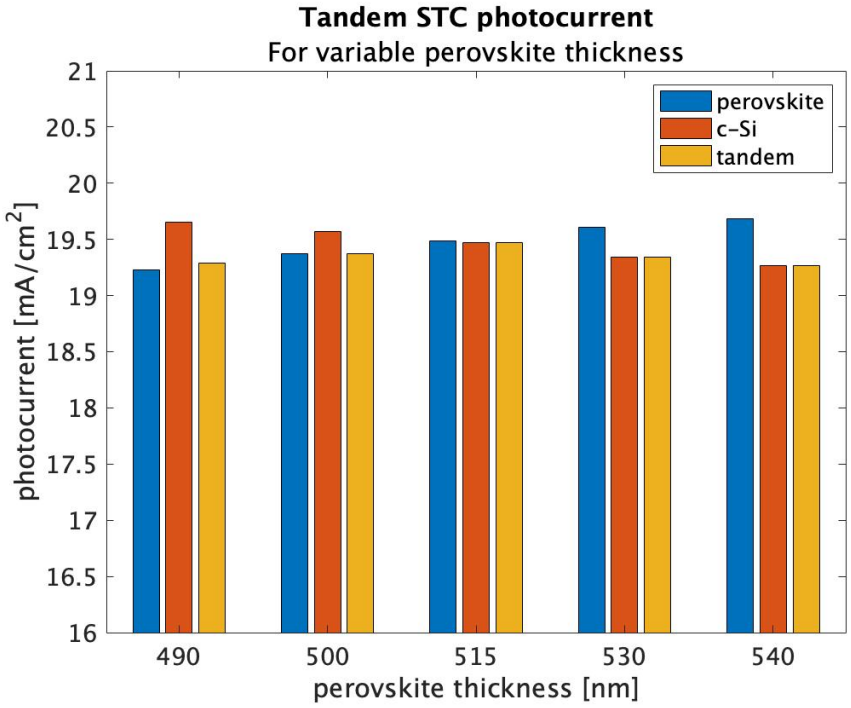

Figure 2.5: Perovskite and c-Si absorbers photocurrents comparison for different perovskite thicknesses, and resulting 2T tandem photocurrent output.

the module structure is 1.89 m^2, meaning that a percentage of this space results in potential optical (active area) losses. In particular, roughly 6.4% of the module area does not contribute to light absorption. Ahead of the module optical simulation with the Lux software, the Toolbox builds a three-dimensional geometry of the module as an array of cells and employs the *rectabox* function to shape it. The module as structured is then tilted with an angle of 27° and mounted off the ground at a 0.5 m height. Although this tilt angle is not the optimal value for the locations considered in this study, to maintain consistency in comparing our results the angle will be kept constant. Azimuth orientations considered are however both south-facing (0°) and north-facing (180°) according to which hemisphere the location of the simulation belongs to. Moreover, albedo to account for surroundings reflectance is set to the standard default value of 0.2. This can be considered a typical value for free-horizon, generic-ground simulations. All module geometry specifications and module imaging reconstruction are reported in detail in Appendix B.

The output of the simulation through Lux software is the Sensitivity Map (S) plotted over the hemispherical sky dome, for both azimuth orientations (Fig. 2.6). These results are based on a ray-tracing computation with a default 5000 rays per each direction of light. The represented S features the average sensitivity of the 72 cells in the module. As a free horizon with no shading from surrounding objects is considered, it can be assumed that the average cell S is accurate with a very small amount of error [56]. If we were to consider a non-free horizon, the single cell sensitivity simulation would have been preferred for higher precision. As it is evident from the maps, the origin of the incident rays highly influences how the module responds to irradiance,

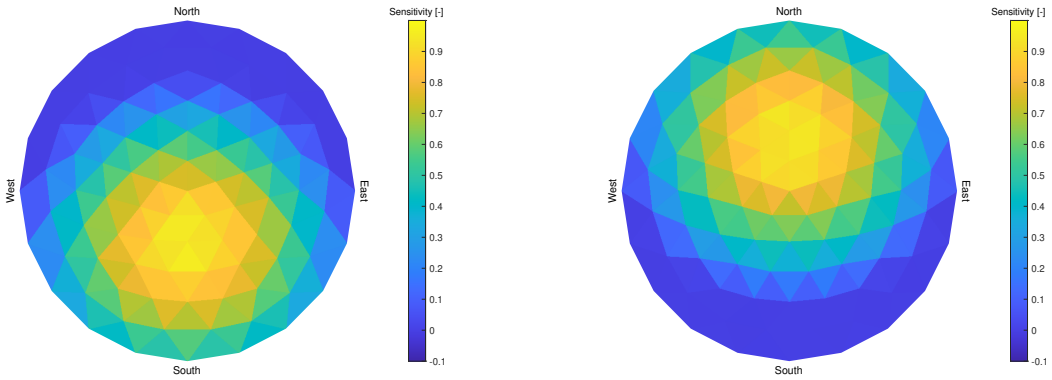

Figure 2.6: Module average cell sensitivity map for 0°and 180°azimuth orientations.

which is a relevant factor when considering actual conditions, sun position and global horizontal irradiance (GHI). The sensitivity output of this model is in fact also wavelength-dependent.

2.2.3. Weather simulation

Real-world conditions to simulate the performance of the cell are introduced through the Weather model. Location specific atmospheric data is utilised as input along with the Sensitivity Map. The former is retrieved from the Meteonorm database and it contains hourly values of DNI, DHI, GHI and sun position among others, for a full year.

The locations considered in this study are Reykjavik, Iceland (64°0848 N, 21°5624 W), Rome Ciampino, Italy (41°4758 N, 12°3550 E) and Alice Springs, Australia (23°420 S, 133°5212 E). Such locations are consistent with previous studies from Singh et al. and M. Jahyan [18], [61]. They represent, respectively, typical high-latitude and mid-latitude northern hemisphere climates and southern hemisphere tropical climates. This is in order to provide a wider-scope analysis of energy yield simulations around the globe.

Through the Perez model, the Weather simulation allows to recreate illumination settings to which the module is exposed. Yearly irradiation values obtained through the sky model and Meteonorm have also been validated against typical PV potential data maps (such as Solar Atlas) for the locations [74]. As a result, hourly values of power absorbed by the module and absorbed photon flux from incident light are obtained. The former will be employed within the Thermal model. It is expressed in terms of total absorption in each cell, in W/m^2. The (effective) absorbed photon flux on the other hand is necessary to compute the hourly values of implied photocurrent density generated by the two sub-cells. From the Weather model, values of photon flux are expressed as an array of hourly sample values for each absorber layer. This means that the number of photons per hour is assumed to be constant during each second of that hour. The two hourly sub-cell photocurrents can therefore be obtained through the

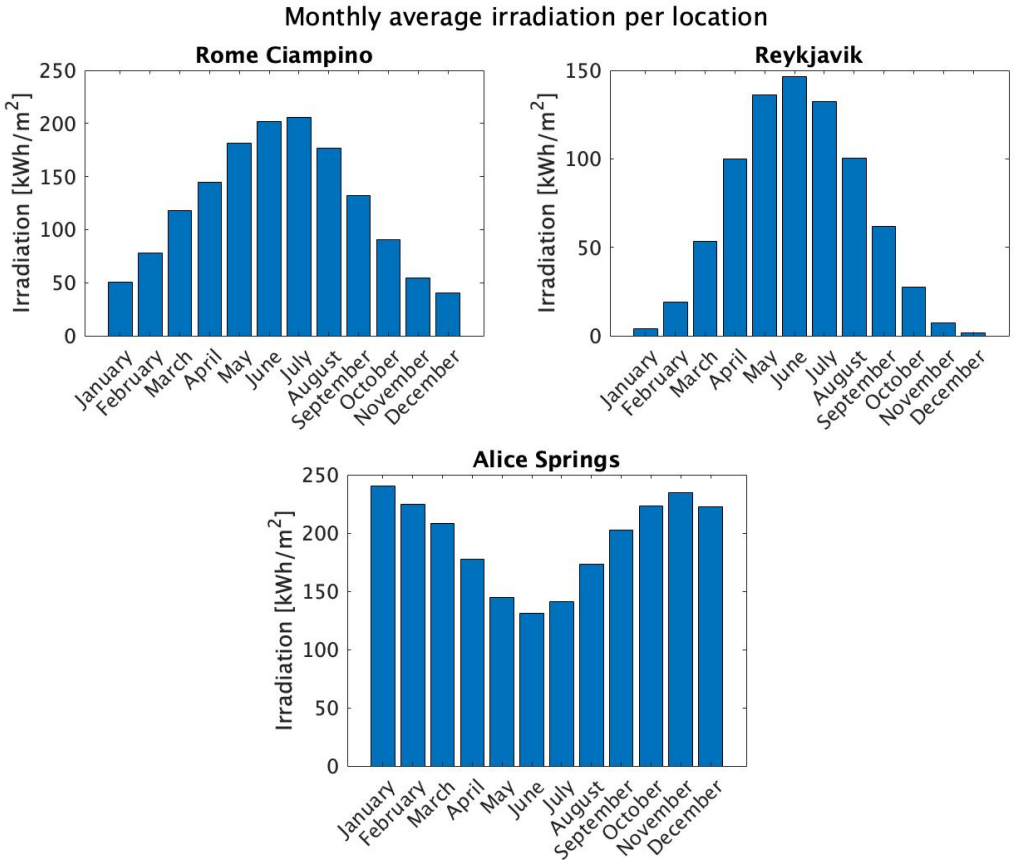

Figure 2.7: Monthly average irradiation as simulated for the locations of Reykjavik, Rome Ciampino and Alice Springs.

following equation

$$j_{ph,i}(t) = \Phi_{ph,i}(t) * q \tag{2.1}$$

where $\Phi_{ph}(t)$ is the hourly photon flux absorbed by the i-sub-cell and q is the elementary charge constant.

The photon flux absorption characteristic of each cell depends on the absorption simulated in the Cell part of the Toolbox. The equation employed to calculate the photocurrent is considered valid under the assumption that each absorbed photon generates one pair of electron-hole carriers [31]. As output of the Weather model, $\Phi_{ph}(t)$ is expressed in photons per hour per square meter. Equation 2.1 therefore requires a dimensional correction to obtain photocurrent values in mA/cm^2. This was originally a source of error as the implemented Weather model Matlab® script for the Toolbox did not display the correct units for the photon flux output, resulting in overestimation of photocurrent values.

Confirming results' validity from the Weather simulation is necessary as these photocurrent output values are employed in the Electrical model. Therefore, in order to validate simulation results, a check between obtained photocurrent values and theoretical expected photocurrent is carried out. The calculation of the theoretical value for comparison is based on the capacity factor definition for PV devices. For each of the three locations, it is easily possible to estimate the yearly amount of equivalent sun hours (ESH_y), or the number of hours for which we have an irradiation of 1,000 W/m^2. This is obtained through calculation of the total irradiation. Then, through the following simple calculation

$$current\ ratio = \frac{ESH_y(t)}{h_y(t)} \tag{2.2}$$

where $h_y(t)$ is the number of hours per year, we obtain a theoretical *current ratio*. Such ratio defines the proportion between the average theoretical yearly photocurrent delivered by each module cell and the STC current, where irradiation is constant at 1,000 W/m^2. It is therefore a representation of the theoretical average current difference between real-world and STC simulation. As this ratio is calculated based on the yearly irradiation per location considered, it delivers a different expected current value at each location. In table 2.1, the ratios for the three considered locations are shown. The expected average photo-current is therefore calculated through multiplication of the STC optimized 19.5 mA/cm^2 tandem current and the ratio. The simulated average photocurrent on the other hand is obtained as yearly average of the least of the two sub-cells currents, in the 2T configuration, per each hour. Such average also includes the parts of the day in which the device does not output any current. Results of this validation method confirm the outcome of the simulations so far. It is possible to observe a small discrepancy in the values of expected and simulated average photocurrent per each location. This deviation oscillates between a very error within ∼1% for Rome and Alice Springs, and a ∼3% overestimation in Reykjavik. Due to the minor scale of these errors, they can be credited to approximations in the simulation method such as for the irradiance reconstruction model.

Location	POA Irradiation [kWh/m^2/year]	Current ratio [-]	Expected avg. photo-current [mA/cm^2]	Simulated avg. photo-current [mA/cm^2]
Reykjavik	849	0.097	1.89	1.92
Rome Ciampino	1,495	0.171	3.33	3.34
Alice Springs	2,280	0.260	5.07	5.01

Table 2.1: Yearly POA irradiation, current ratio, expected photocurrents and simulated photocurrents for the three considered locations.

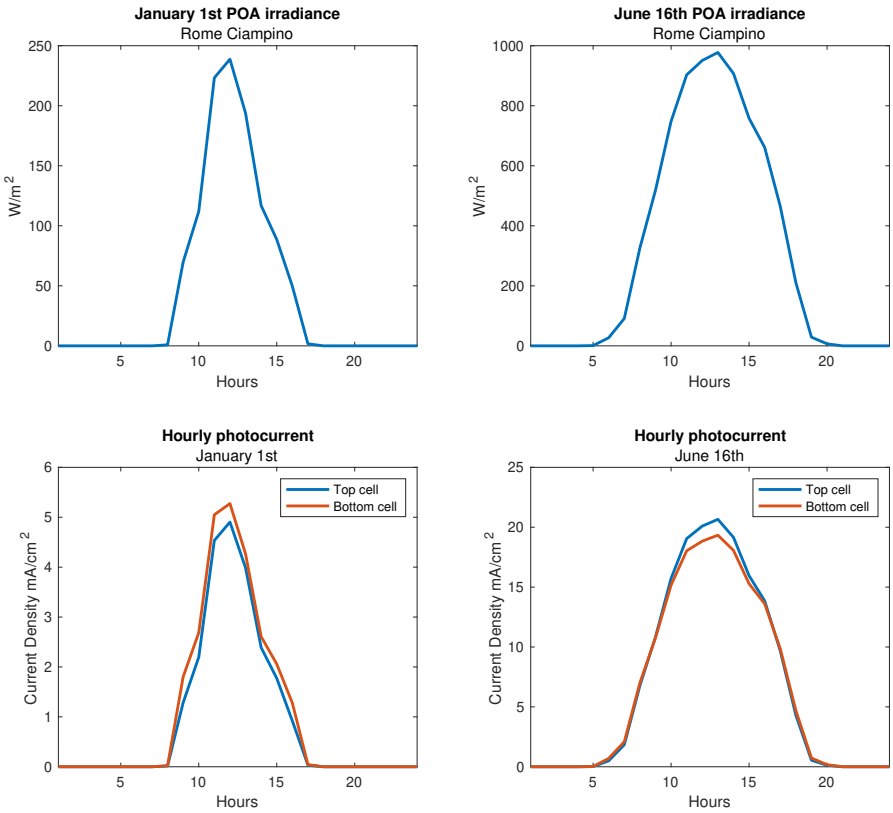

Figure 2.8: Comparison between low irradiation (winter) and high irradiation (summer) days for the Rome location. Per each day, the photocurrents produced are compared between each other and their trend compared with daily irradiance variations.

To further examine these results and check for validity and consistency, a comparison between a single winter day and summer day is carried out as well. In this case, the sole Rome Ciampino location is taken as example for simplicity.

The goal is to ensure that valid current outputs are aligned with the irradiance hitting the plane of array, hence checking validity of the model and the Toolbox simulation. We are therefore not looking at yearly average photocurrent values, but more specifically the hourly output. In Figure 2.8, irradiance profiles for January 1st and June 16th are shown. These two days are chosen as representatives of low and high daily irradiation, respectively, and therefore offer two different perspectives on photocurrent generation. Underneath, the corresponding generated hourly photocurrent for that day is represented, for both sub-cells. It is clearly visible how on the summer day, at high irradiance values that come close to the STC conditions, the j_{ph}s imitate the optimized photocurrent value of 19.5 mA/cm^2. The single cells' hourly photocurrent values also show how the mismatch issue propagates during the course of the day. Depending on the season and therefore typical GHI and spectrum due to sun position throughout the day, the cause of the mismatch can be either the top or the bottom cell not producing enough photocurrent. This is visible in the photocurrent graphs as the cells alternate in the current

limiting role depending on the day.

2.2.4. Thermal simulation

As the hourly weather data obtained from Meteonorm reflects real-world conditions, the temperature effect on the photovoltaic module is also taken into account in energy yield simulations. The module temperature depends on many factors which are all included in the fluid-dynamic model implemented in the Toolbox. In particular, factors considered through this model include ambient, sky and ground temperature but also absorbed power by the cells and wind speed at module height. The energy balance equations from the fluid-dynamic computation allow to consider both radiative and convective heat transfer through encapsulation and cell structure.

The temperature is calculated cell-by-cell, and the output also shows module temperature calculated as average of minimum and maximum single cell temperatures at the corresponding hour. For the location of Rome, the module temperature function is represented in Figure 2.9. The average module temperatures simulated are 16.04℃, 36.86℃ and 45.57℃ for Reykjavik, Rome and Alice Springs respectively.

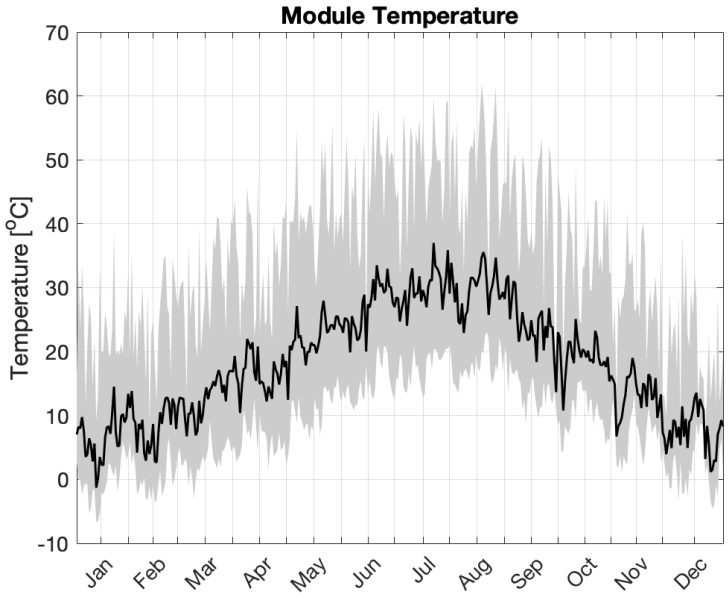

Figure 2.9: The function describing module temperature variations throughout the whole year, in Rome Ciampino. The black line represents the average temperature between the maximum and minimum daily temperatures (represented by the grey line).

2.3. Conclusion

This Chapter has described the process of simulating the perovskite/c-Si tandem structure adopted in this work through the Optical and Thermal parts of the PVMD Toolbox. The goal was to answer the first sub-objective of this thesis, or the implementation of the tandem structure within the Toolbox for Optical to Thermal simulations.

First, the structure of the tandem unit cell has been presented, in order to understand its architecture and materials composition. Then such structure has been implemented on the GenPro4 optical simulation software to obtain the cell's absorptance behavior. For STC conditions, the previously optimized tandem structure in terms of perovskite thickness has also been demonstrated to deliver an implied photocurrent density of 19.5 mA/cm^2 at 515 nm perovskite thickness.

The cell has then been used to construct a 72-cells module, for which a Sensitivity Map was calculated through the Lux software. For real-world Weather simulations, three locations around the globe are considered to study the module performance, namely Rome Ciampino, Reykjavik and Alice Springs. The Weather simulation has been ran utilizing previous outputs of the Cell and Module simulations in order to obtain hourly absorbed power and photons values. The photocurrent delivered by the module can be calculated from the Weather model output. The average photocurrent values per each locations have been calculated to be 1.92, 3.34 and 5.01 mA/cm^2 for Reykjavik, Rome and Alice Springs respectively. These values have been validated through a theoretical evaluation.

Finally, a Thermal simulation of the module is carried out through the fluid-dynamic-based Toolbox model. Hourly temperature values are used in successive simulations to take actual operative performance into account. Average module temperatures simulated came out to be 16.04℃, 36.86℃ and 45.57℃ for Reykjavik, Rome and Alice Springs respectively.

3

Sub-cells J-V curves with experimental characterization of c-Si bottom cell

Ahead of the Electric simulation of the tandem module that will be discussed in Chapter 4, this Chapter introduces the current-voltage (J-V) characterization of the two sub-cells employed in the tandem structure. In particular, in order to simulate real-world performance of the module it is necessary to obtain the temperature and irradiance-dependent one-diode cell parameters of both cells. This is achievable through an analytical parameter extraction method based on variable temperature and irradiance J-V curves of the cells. Such method along with its application within the PVMD Toolbox and the one-diode theory will be introduced in Chapter 4. Therefore, for this purpose, in section 3.1 the ASA-simulated J-V curves for the perovskite top cell are presented. Then in section 3.2, the curves for the silicon bottom cell are shown as a result of the measurement experiment on the poly-SiOx based silicon cell produced at TU Delft. Finally, section 3.3 includes a discussion on the validation of the experimentally retrieved silicon cell J-V characteristics.

3.1. Current-voltage curves for the perovskite top cell

The perovskite cell utilised for this tandem structure has already been presented in the previous Chapter. The objective here is to characterize the cell as a single independent device in terms of variable irradiance and temperature J-V curves. As the standard test conditions don't provide enough information on the behavior of a solar device for changing operative conditions as in real-world applications, considering multiple curves other than the single STC one allows for a more accurate representation within this work's modeling approach. However, due to the physical unavailability of the perovskite cell for experimental measurements to obtain such variable condition curves, the latter have been adapted from [61] as previously retrieved through the Advanced Semiconductor Analysis (ASA) software simulation tool developed at TU Delft. ASA is an opto-electronic simulation device that can be used to solve semiconductor equations for both crystalline and amorphous structures and therefore allow for J-V characterisation [75].

The structure of the cell is implemented in the software, then the curves calculated for different illumination and temperature conditions.

The curves are generated keeping one of the two variables, either temperature or irradiance, constant at its STC value, while the other varies between specific values and vice versa. Although it is a software simulation and therefore might differ from the real cell measurements, the advantage is that a wide range of operating conditions can be set to simulate the J-V behavior in a simple manner. When temperature is fixed at 25℃ irradiance is varied with regular intervals between 200 W/m^2 and 1000 W/m^2. On the other hand, when irradiance is kept constant at 1000 W/m^2, temperature is varied again with regular intervals between 15℃ and 55℃ . The reader should note that as ASA varies the irradiance, only intensity variations are simulated. This means that the spectrum incident on the cell is scaled compared to the standard AM1.5 spectrum, hence no spectral variations are considered. Results of the perovskite cell simulations are shown in Figures 3.1 and 3.2 for variable temperature and irradiance, respectively. The large number of these curves represents a quite comprehensive set of data that can be used to extract the perovskite parameters with a reasonable accuracy. The more accurate the parameters, the more the Electric simulation of the cell within the Toolbox will give precise results.

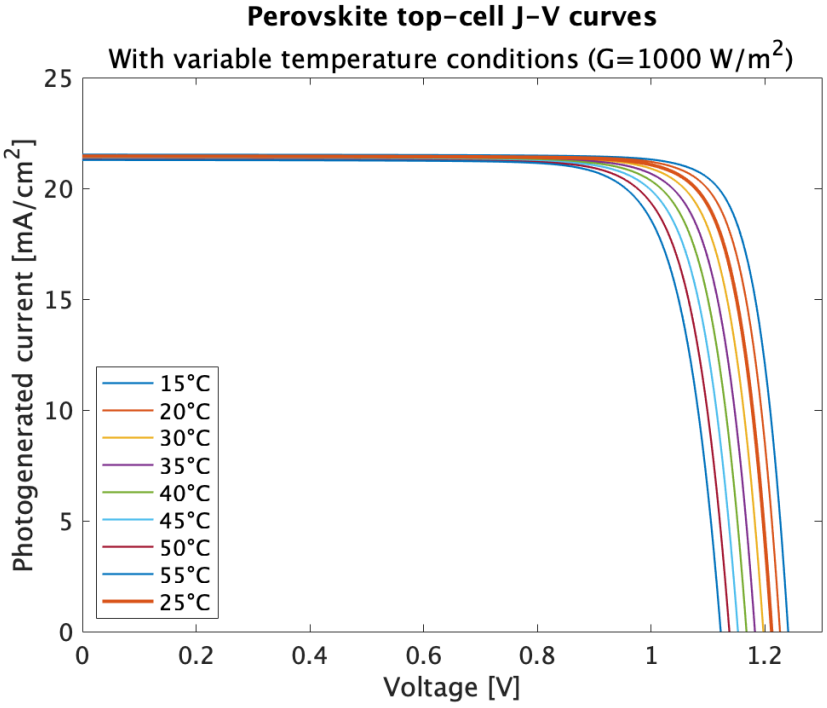

Figure 3.1: J-V curves for perovskite top cell simulated through ASA software. Each curve corresponds to a different temperature value of the cell. The wider orange curve represents the STC J-V curve.

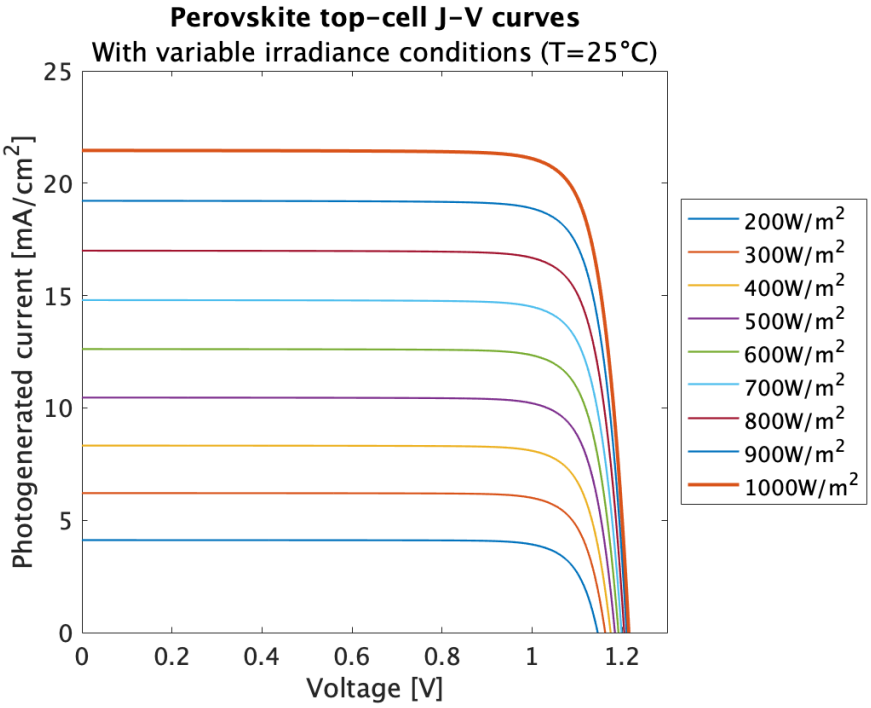

Figure 3.2: J-V curves for perovskite top cell simulated through ASA software. Each curve corresponds to a different irradiance value of the cell. The wider orange curve represents the STC J-V curve.

A literature scan for theoretical and experimental results has also been done, in order to validate similarly structured perovskite behavior for variable temperature and irradiance [76], [77], [78]. Such experimental measurements can obviously differ from ASA simulated J-V curves. For example, typical perovskite cell prototypes feature a linearly growing trend between the short-circuit current point and maximum power point, which in ASA is simplified to be more ideally constant. Having a physical device on which to perform measurements would therefore lead to much more precise results. Nevertheless, the general trend of the curves for variable conditions is confirmed. In addition, from a numerical point of view it was possible to validate the temperature curves by obtaining values of maximum power point from the characteristics simulated through ASA and comparing with literature retrieved power temperature coefficients. A temperature coefficient of about -0.21%/°C resulting from the ASA curves simulation can be confirmed by some typical perovskite values in the range of -0.10% to -0.2% per °C [79].

3.2. Current-voltage curves for the c-Si bottom cell

As for the perovskite sub-cell, it is needed to obtain J-V curves for the crystalline silicon bottom cell utilised in this tandem structure. The c-Si cell in object is the already introduced TOPCon device featuring poly-SiOx carrier selective passivating contacts, developed at TU Delft. Therefore in this case, the physical availability of the device has allowed to perform experimental measurements on the cell and obtain real J-V characteristics. The goal is the same as for the perovskite, which is to characterize the cell under variable temperature and irradiance conditions. This was achieved through an experimental set-up with equipment avail-

able at the TU Delft Electrical Sustainable Power Laboratory.

It is noteworthy to mention that as for the ASA-implemented perovskite cell previously introduced, the c-Si cell utilized in these measurements serves as reference to calculate the electrical parameters of the bottom cell. The types of layers, absorber and CSPCs constituting the cell are the same as explained in Chapter 2. However, the measured external parameters of the cell (Fill Factor, efficiency, photocurrent generated, voltage output,...) may differ from the simulated ones and are not utilized in the final energy yield calculations. The latter are in fact results of the Toolbox simulation.

3.2.1. Experimental set-up

The main piece of equipment utilised for the experiment is the WACOM Solar Simulator. With the use of special mirrors, this simulator is able to produce very high quality composite light through halogen and xenon lamps [80]. The light rays that the unit produces feature a very similar spectral distribution to that of the Sun [80]. Some differences are still visible when comparing the spectrum of the WACOM to the Sun's AM1.5 (Fig. 3.3), which is obviously quite typical in artificial solar simulators. However, the integral of the measured WACOM spectral irradiance adds up to about 1,080 W/m^2 against the 1,000 W/m^2 of the AM1.5 spectrum, so less than a 10% deviation. The instrument is shown in the measurement set-up adopted for this experiment in Figure 3.4. The WACOM is interfaceable through a LabView based software GUI, on which the user is able to set multiple details and requirements for the measurements.

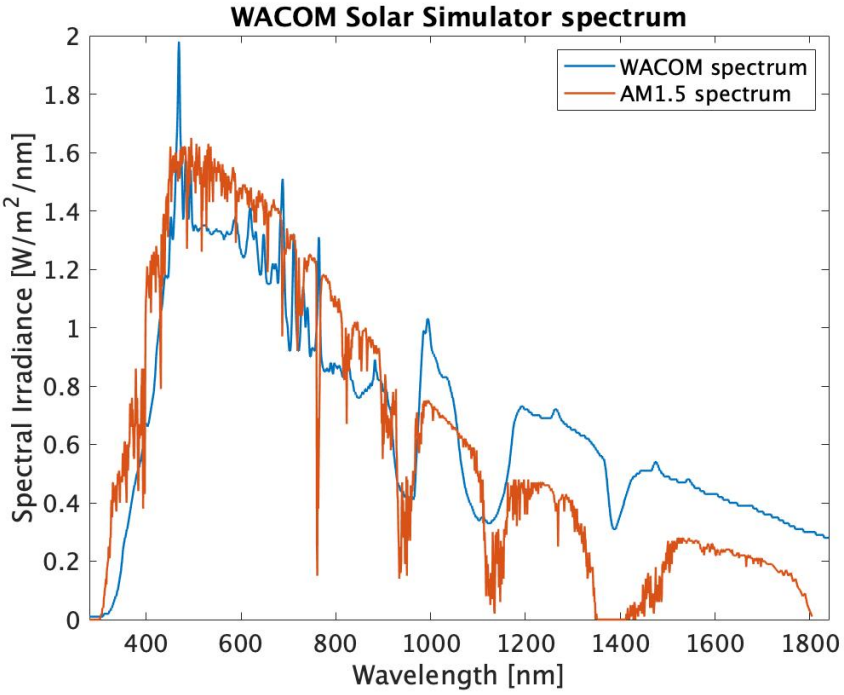

Figure 3.3: The WACOM Solar Simulator spectrum compared to the standard AM1.5 spectrum.

Figure 3.4: The WACOM Solar Simulator measurement set-up with the gold-plate NIP stage for variable temperature measurements, underneath the cells' wafer.

The stop/go commands on the measurements can be given directly through the software, which controls the simulator's illumination shutter. When the latter opens and the cell is illuminated, the software performs J-V sweeps by varying the voltage on the cell within a specific user-set range. Results of the measurements include open-circuit voltage, short-circuit current, maximum power point, efficiency and Fill Factor of the cell.

Variable irradiance and temperature are not a condition that automatically changes on the simulator as in real-world. Therefore it is necessary to utilise specific equipment when measuring the cell. For variable temperature measurements, the WACOM is configurable with a gold-plated NIP stage that is controlled through the simulator's JULABO cooler in order to adjust temperatures. Through the GUI, the user can insert various values of temperatures with a minimum of 15℃ and maximum of 55℃. For variable irradiance measurements, it was necessary to adopt irradiance filters on top of the cell when placed under the simulator. For this purpose, 3 "polka dots" filters have been utilised (shown in Fig. 3.5). The surface of the filters features a mesh of very small holes that allow for a precise scaling down of the intensity. This type of filter is much more accurate than other typical filters (such as *neutral density* filters) as it doesn't affect the transmitted spectrum. Hence their transmittance functions are only imperceptibly wavelength-dependent. Such functions have been measured through the PerkinElmer® LAMBDA 1050 Integrating Sphere available in the ESP Laboratory and reported in Appendix D against a reference standard neutral density filter. The slight variations of the transmittance function are caused by the small imperfections over the surface of the filter glass. Three white covers for the filters for secure handling of the devices and a structure holding the filters in place over the cell have been 3D printed. The necessary height of the holding structure was calculated in order to give enough areal space between cell and filter

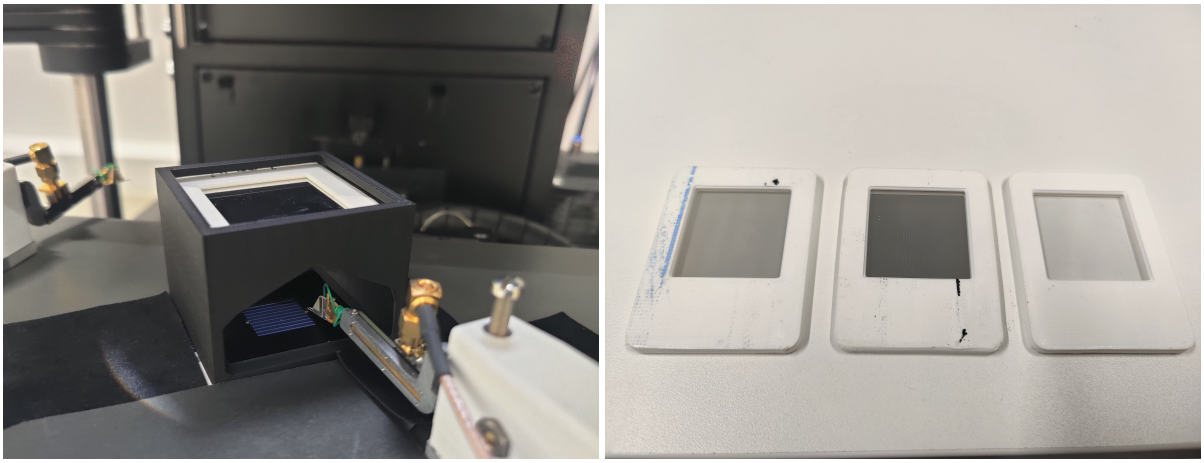

Figure 3.5: The irradiance measurement set-up, featuring: (on the left) a 3-D printed holder for the irradiance filters, custom-made to fit over the c-Si cell. (on the right) the irradiance filters utilised to scale down the intensity hitting the cell, mounted inside 3-D printed white covers for proper handling (note the different luminosity of the glasses, according to the filter's transmittance capability).

for the meshing pattern to correctly spread light over the solar cell device. Respectively, as measured through the LAMBDA 1050 the three filters deliver 200, 500 and 800 W/m^2 irradiance values, which together with the standard WACOM's 1000 W/m^2 allow for four variable irradiance measurements.

Finally, the cell utilised for the measurements is the single-side textured c-Si poly-SiOx based cell shown in Figure 3.6. The area of the cell is roughly 3.92 cm^2 and features back and front (framed) metallizations for contact connections. The 3D printed structure for the filters was designed specifically to fit the dimensions of the cell's mask, to avoid shadowing or any other type of optical losses during measurements. Then the wafer was directly placed on the gold-plated stage, which was used for both temperature and irradiance measurements, and remained stable thanks to a vacuum holding system integrated in the stage itself, for precise setting of the equipment.

3.2.2. Measurements results

With the goal of obtaining as many J-V characteristics as possible, the whole range of temperature allowed through the NIP stage was exploited. The sweeps were performed for variable temperatures, in constant steps of 5°C. At this point, irradiance was kept constant at 1000 W/m^2 as it is output by the WACOM simulator. Results of these measurements are shown in Figure 3.7. As expected from theoretical considerations, the increasing temperature negatively affects the cell's efficiency. The short-circuit current of the cell slightly increases due to a higher photocurrent generated, thanks to the bandgap lowering effect with higher temperatures. However, the open circuit voltage is reduced more sensibly and this affects the maximum power point of the cell if compared to STC. The curves shown in the figure were constructed based on 300 data points gathered through the J-V sweep.

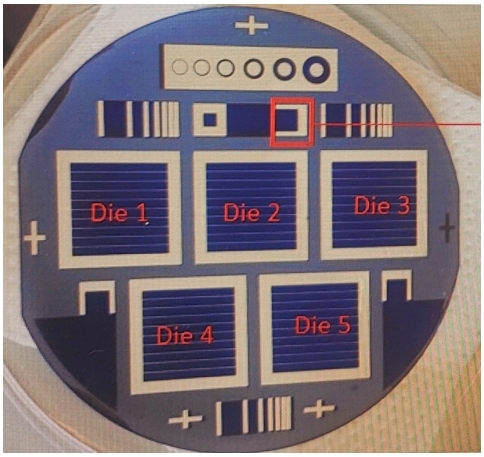

Figure 3.6: The silicon wafer containing the cells produced at TU Delft. The cell utilised for these measurements corresponds to die no. 4 (best-performing cell on the wafer).

For the variable irradiance measurements, the gold-plated stage was kept at a constant 25°C temperature and the J-V sweeps with same number of data points performed for the 4 different irradiance values. The filters were substituted one by one on the holder and the cell illuminated with each of them. Results of these measurements are shown in Figure 3.8. As the irradiance intensity on the cell is reduced, it is visible how the curves exhibit a much lower photogenerated current density.

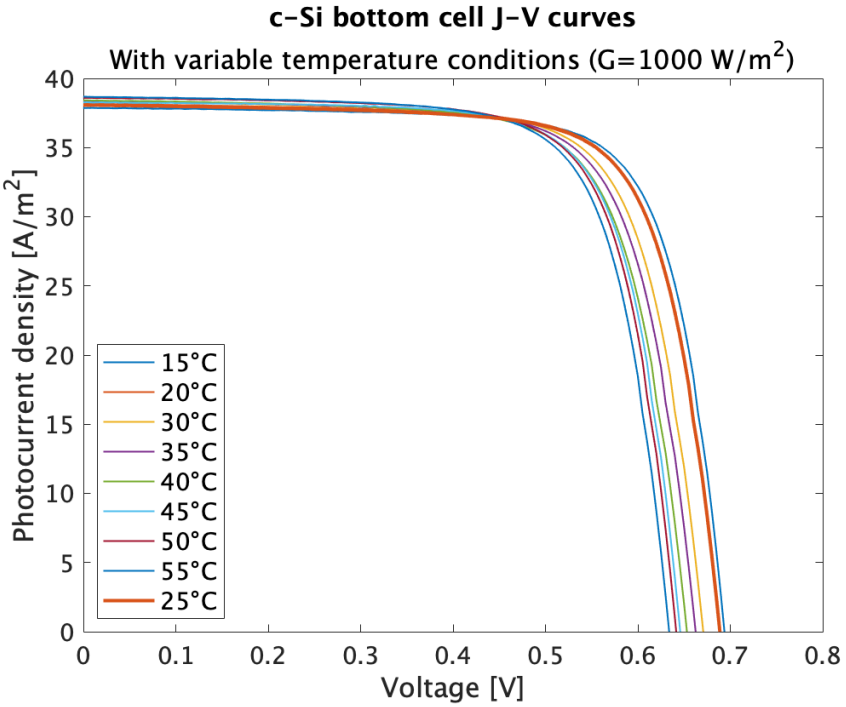

Figure 3.7: J-V curves for c-Si bottom cell measured through the WACOM. Each curve corresponds to a different temperature value of the cell. The wider orange curve represents the STC J-V curve.

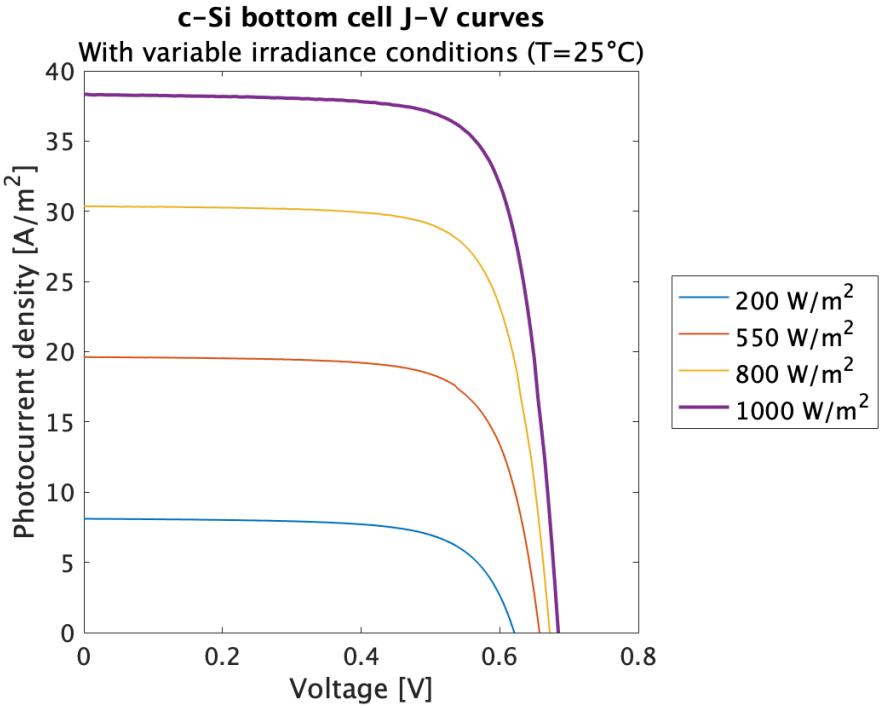

Figure 3.8: J-V curves for c-Si bottom cell measured through the WACOM. Each curve corresponds to a different irradiance value hitting the cell. The wider purple curve represents the STC J-V curve.

3.3. Validation of experimental measurements results

As a first method of ensuring that the results can be consistent and accurate when conducting this type of experiment, it is necessary to calibrate the WACOM Solar Simulator instrument through two default cells. This can be seen as a first step to contribute to consistency of the obtained results. These default cells are two filtered and un-filtered silicon reference cells with specific expected values of V_{oc} and I_{sc} which the software detects for Standard Test Conditions settings at 25℃ and 1000 W/m^2 irradiance. This is carried out once the simulator is ready for operation. When the calibration procedure is complete, the user can install its own measurement stage under the simulator and perform the experiment. These reference cells have also been used to confirm the measured transmittance values of the filters employed.

3.3.1. Temperature measurements

To validate the J-V curves obtained through temperature variations, the best method is to compare the empirically obtained temperature coefficients of the poly-SiOx based silicon cell employed, with other devices featuring the same technology. In this case, other validated TOPCon solar cells' temperature coefficients retrieved from literature serve this purpose. The power temperature coefficient represents the percentage loss of power per ℃ variation of temperature with respect to the module cell power [81]. This value is always negative in photovoltaics, meaning that an increase in temperature compared to the standard 25℃ leads to a lower power output of the cell. It can be empirically obtained through simple calculations comparing STC power output of the cell with different temperatures. For this cell, the STC maximum

power point is reached at a voltage of 0.57 V and a current of 0.136 A, or 0.077 W power. When compared to a different temperature, such as the upper 55℃ limit, the power output is reduced to 0.070 W, a decrease of approximately 9.1%. Consequently, the empirically obtained power temperature coefficient can be estimated through the following equation

$$\kappa_T = \frac{P_{loss}[\%]}{\Delta T} \tag{3.1}$$

where P_loss is the power loss percentage and ΔT is the temperature differential between STC and 55℃ (= 30℃) [82]. For this temperature variation, we obtain a value of -0.303%/℃. When repeating the same procedure with other temperature variations, a small deviation is noticeable (the coefficient improves by as much as +0.009%/℃). However we can confidently assume the temperature coefficient to be approximately equal to the worst temperature case value of -0.303 %/℃. This value is in line with other literature retrieved temperature coefficients for TOPCon solar cells. In fact, typically devices featuring this type of technology exhibit a coefficient within the range of -0.3%/℃ or below, which is under other industrial photovoltaic devices such as typical mono-crystalline solar cells [83], [84]. Hence, the analysis shown in this paragraph helps prove the validity of the experimental set-up for temperature variable measurements.

3.3.2. Irradiance measurements

The photogenerated current that a solar cell produces when exposed to illumination can be theoretically predicted. A theoretical calculation of the j_{ph} and comparison to the measured photocurrent values is therefore a method that can be employed to validate the irradiance measurements both in STC and variable irradiance conditions.

The photogenerated current j_{ph} for a cell illuminated with AM1.5 spectrum at STC can be calculated through the following equation [31]

$$j_{ph} = -q \int_0^{inf} EQE(\lambda)\ \Phi_{1.5}(\lambda)\, d\lambda \tag{3.2}$$

where $EQE(\lambda)$ is the wavelength-dependent external quantum efficiency of the cell, $\Phi_{1.5}(\lambda)$ is the wavelength-dependent photon flux for STC AM1.5 spectrum. Typically, for silicon cells this integral is evaluated over a wavelength interval of λ=[300,1200] nm [31].

Consequently, to perform this validation the silicon cell's EQE was obtained through an instrument that measures the cell current under monocromatic illumination. The EQE function of the cell is reported in Appendix D. The photon flux on the other hand can be derived from the relation to the measured spectral irradiance of the WACOM solar simulator previously shown.

Equation 3.2 can also be expanded to include the irradiance intensity scaling-down effect resulting from the use of filters. This is achieved through inclusion of the transmittance function ($T(\lambda)$) of the filters in the equation, as a multiplying coefficient. Although the measured filter transmittance is practically constant throughout the wavelength range, for correctness in the calculations its wavelength-dependent function is multiplied in the integral. Consequently, photocurrent calculations are carried out for all four irradiance conditions considered and their results compared in Table 3.1 to the measured currents.

The theoretical photocurrent values are consistent with the measured ones, both at STC and with the use of the three filters. Slight deviations can still however be noted. For STC conditions, this can be credited to the reasonable measurement error that is inherent to the experimental setting adopted. In addition to this, when using the filters there is another smaller source of error that leads to higher measured photocurrent values if compared to their theoretical counterparts. A part of the light hitting the cell is reflected, especially in the wavelength ranges between [300,400] nm and from 1050 nm on, approximately. Reflected beams running in the same direction of incident light are therefore partially reflected back onto the cell after hitting the filter from below. Linked to this, is also the scattering effect caused by the front texturing of the cell. Hence the actual final irradiance to which the cell is exposed is slightly higher than the value the filter should deliver, which causes photogenerated current to slightly increase. Moreover, measurement setting is slightly more sensible to this reflective effect error when employing lower irradiance filters as the error increases. For example, when considering the 20% transmittance (200 W/m^2) filter, 80% of the light reflected by the cell to the filter is reflected back into the cell again. The opposite occurs instead for the 80% transmittance filter. These sources of error can also been validated by taking into consideration the measured reflection function $R(\lambda)$ of both the cell and the filters. However, due to the quite imperceptible variation that this experimental error induces in the measurements, the J-V results obtained can still be considered valid with a certain level of confidence.

Irradiance [W/m^2]	Theoretical j_{ph} [mA/cm^2]	Measured j_{ph} [mA/cm^2]	Relative error
1000	37.56	38.32	2.02%
800	29.71	30.35	2.15%
500	19.18	19.61	2.24%
200	7.89	8.10	2.65%

Table 3.1: Comparison between the theoretical calculated photocurrents and the measured photocurrents for the poly-SiOx based c-Si bottom cell. The biggest part of the relative error is due to the measurement set-up, the remaining error comes from the reflective effect of the filters.

3.4. Conclusion

This chapter has presented the current-voltage curves of the two tandem sub-cells. In particular, the curves have been gathered for variable temperature and irradiance conditions. Such curves will be employed further to describe the behavior of the cell in real-world conditions. Through this Chapter, the second sub-objective of the thesis has been answered.

For the perovskite top cell, the J-V curves were retrieved through the ASA software and literature validated. For the c-Si bottom cell, an experiment was carried out to perform variable irradiance and temperature J-V curves measurements on the physically available poly-SiOx based silicon cell produced at TU Delft. Such experiment included use of multiple instruments, including irradiance filters and a temperature variable plate, and a thorough validation system was therefore adopted in order to assess reproducibility and consistency of the measurement results. The validation procedure brought positive results for all types of measurements, confirming the correctness of the J-V curves obtained.

4

Tandem module Electrical performance: annual energy yield prediction

In this Chapter, the application of the Electric models from the PVMD Toolbox is discussed. Both the tools and results linked to the simulation of the electrical behavior of this tandem module are presented. In section 4.1, the background leading to the Electric simulation is briefly introduced. In particular, the one-diode cell model that applies to both sub-cells and the circuit parameter extraction method employed to describe the tandem's behavior for variable operating conditions are explained. This topic is linked to the previously presented J-V analysis for the perovskite and c-Si cells. In section 4.2 the Electric simulation method through the Toolbox itself is presented, then first energy yield results for the STC-optimized structure are shown in section 4.3. In section 4.4, an overview of the system DC losses considered when predicting the energy yield is given.

4.1. Background: cell one-diode model and parameter extraction method

Within this work, we are interested in simulating and analysing the performance of the defined module structure in real-world conditions. In contrast to standard test conditions, real-world operating conditions are variable and this influences the output of the PV system. In particular, a PV system in real-world applications cannot produce the same constant power output as if it was under STC. So far, this has been taken into account for the tandem module through simulation of its optical and thermal performance with the PVMD Toolbox. In Chapter 3, results have been shown to describe how the two tandem sub-cells current-voltage characteristics behave when the operating conditions are changing. At this point, the goal is to adopt a method that allows to take this behavior into account from an electrical performance point of view, starting from the J-V results previously obtained.

The electrical behavior of a solar cell can be described through its equivalent circuit model. Each component in this circuit depicts a parameter that characterizes the cell. Two models

exist: the one-diode and two-diode models. The two-diode model is more accurate but also computationally complex. It is therefore more convenient when performing simulations with the Toolbox to adopt the one-diode model (shown in Figure 4.1) for behavior simulation purposes. The one-diode circuit model comprises of five parameters which are used to construct the J-V characteristic of the cell using the following equation

$$I = I_{ph} - I_0 \left[exp\left(\frac{q(V + IR_s)}{nk_bT} \right) - 1 \right] - \frac{V + IR_s}{R_{sh}} \tag{4.1}$$

Equation 4.1 is an implicit equation, where the output current of the cell (I) is represented as function of voltage (V) but depends on the following cell parameters

- I_{ph} [A/m^2]: is the photogenerated current, or the current that is generated in the cell through electron-hole pair formation from absorbed photons. In the one-diode equivalent circuit model, it is represented as a DC generator.
- I_0 [A/m^2]: is the saturation current, which represents the current originated from all types of recombinations happening in the cell emitter
- R_s [Ω]: is the cell series resistance, or the resistance that comes from all ohmic losses in the cell bulk as well as contact resistances, on back and front of the cell
- R_{sh} [Ω]: is the shunt (or parallel) resistance of the cell, which represents the current losses due to defects in the cell absorber.
- n [-]: is the ideality factor of the cell, which helps identify the main recombination mechanism in the cell and shows how closely the cell, when assumed to behave as a diode, follows the ideal diode characteristic (ideally $n = 1$).
- T [K]: is the cell temperature.
- q, k_B: are the electron charge and Boltzmann constants, respectively.

As these parameters describe the single cell characteristic, they can be extended to define the characteristic of a tandem structure or even a whole module or system, according to the architecture and cells connection type. Moreover, the parameters defined are sensitive to temperature and irradiance variations. This means that equation 4.1 can be used to generate the cell J-V curves when these conditions are varying. This concept is applied in this work through the use of the cell parameter extraction method.

The goal of the parameter extraction method is to obtain the coefficients of two polynomial functions per each parameter. These two functions will then describe the parameter's behavior for variable temperature ($X(T)$) and irradiance ($X(G)$) conditions, respectively. Many parameter extraction systems exist, such as numerical, curve-fitting and analytical methods. Due to lower complexity, lower computational weight and reasonable accuracy, the analytical method is generally preferred. It allows to explicitly calculate the cell parameters through physical assumptions, such as for shunt and series resistances [61]. The analytical method utilised to obtain the parameters for this study case is based on the Matlab® script developed by previous

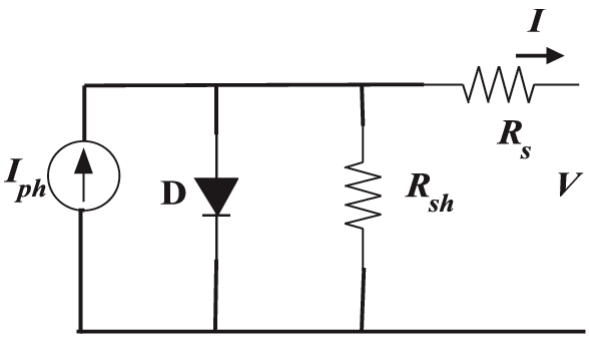

Figure 4.1: The cell one-diode equivalent circuit model.

TU Delft MSc students A. Nour El Din and M. Jayan [60], [61]. However, its discussion falls out of the scope of this work.

As inputs for this script, the J-V curves characteristics of the cells in object have to be employed. The analytical method utilizes in fact a curve-fitting technique to obtain the most accurate possible polynomial representation of each parameter. For all curves used as input to the script, the model fits the reconstructed one-diode current equation by optimizing the coefficients values. That is why it is necessary to provide, as many curves as possible where one of the two conditions varies while the other is kept constant as explained in Chapter 3. The more the curves utilised as input to extract the parameters, the more precise the method should be. Consequently, the polynomial functions generated are used as reference to reconstruct all possible temperature and irradiance conditions that happen in real-world.

In the case of a tandem structure as for this study, each of the two sub-cells is analysed and cell parameters extracted individually. The Electric model of the PVMD Toolbox is in fact programmed to build the J-V curves of the tandem via simulation of the two separate cells' sets of parameter coefficients as explained in the following section.

4.1.1. I-V curve Electrical simulation with PVMD Toolbox

After obtaining the parameter polynomials, it is possible to advance to the simulation of the module through the Electric part of the Toolbox. The two sets of parameter coefficients, for variable irradiance and temperature and for each of the cells used, are loaded on the Toolbox. Then Electric model utilizes the parameters coefficients to reconstruct the I-V (from now on, current instead of density is considered) curves of both the sub-cells, and consequently of the whole tandem. This is achieved with two main steps. First the temperature dependent and irradiance dependent coefficients are coupled in order to obtain a single parameter function of both variables. As explained in [60], [85], this function can be obtained for each parameter as in equation 4.2

$$X(G,T) = \frac{X(G)X(T)}{X(STC)} \tag{4.2}$$

where X can be any of the one-diode cell parameters $(I_{ph}, I_0, n, R_s, R_{sh})$.

Once the parameters coefficients are expressed as function of irradiance and temperature, the parameter values can be estimated through the Toolbox simulation for each possible operating condition. In particular, the parameters are calculated for each hour of the year according to respective values of illumination and weather conditions. The second step is the implementation of the Lambert W-function to reconstruct the I-V curves. As the one-diode model equation is an implicit equation, it is computationally expensive to resolve the cells characteristics for a whole year energy yield simulation. Hence, the Toolbox uses the Lambert W-function to explicitly represent the cell's current output as a voltage-dependent function [59], [86]. In general, the Lambert W-function is expressed as $W(z)$, shown in equation 4.3

$$W(z) = x,\ z = xe^x \tag{4.3}$$

For photovoltaic applications, this allows the following rearrangement of the current-voltage function as in equation 4.4

$$I = \frac{R_{sh}(I_0 + I_{ph}) - V}{R_{sh} + R_s} - \frac{nV_{th}}{R_s} W(z) \tag{4.4}$$

and the z in this case is defined as in equation 4.5

$$z = \frac{R_{sh}R_s I_0}{nV_{th}(R_{sh} + R_s)} exp\left[\frac{R_{sh}}{R_{sh} + R_s}\frac{R_s(I_{ph} + I_0) + V}{nV_{th}}\right] \tag{4.5}$$

The J-V curves can then be obtained for each hour of the year from hourly parameter values. Subsequently, the Toolbox constructs the total I-V curve of the tandem based on the cell architecture used (in this case, 2-Terminal). An important detail to reiterate, is that at this point the Electric model takes into consideration the hourly photocurrent obtained through the GenPro4 software and the Weather model, and not the photocurrent as it was simulated or measured for the single sub-cells while obtaining the I-V curves presented in Chapter 3. This allows to take into consideration spectral variations from real-world illumination data. Through the tandem I-V curve the software identifies maximum power points, or the DC power output of the module $(P_{DC}(t))$.

The flowchart of this modeling approach is depicted in Figure 4.2. Here, the reader can see how the Electric part of the Toolbox intertwines previous simulation outputs with the experimental work conducted. Through the Toolbox GUI for the Electric model it is also possible to set module specifications for bypass diodes and metallizations. For the latter, the default settings are assumed to be valid for this type of module structure while no bypass diodes are considered as we are in a free-horizon setting.

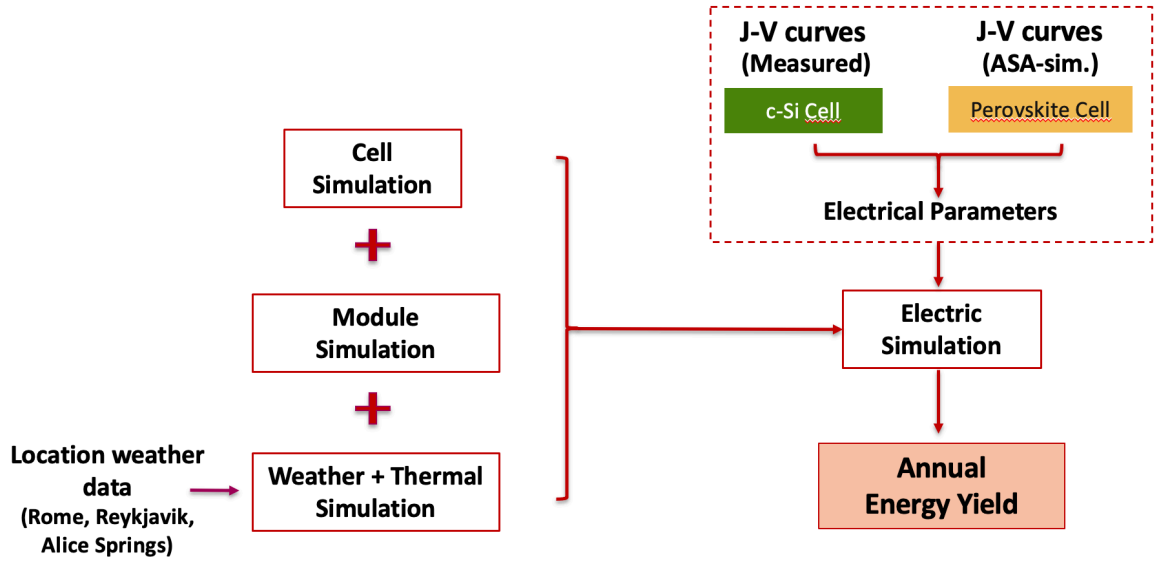

Figure 4.2: The flowchart describing the link between simulation tools and results of the I-V sub-cells characterization, all conveying in the Electric part of the Toolbox. The final objective is the prediction of the tandem module energy yield.

4.2. DC Energy yield prediction results for the STC-optimized tandem structure

In this subsection, results of the energy yield prediction for the STC-optimized structure of the tandem as presented in Chapter 2 are shown. The tandem module configured within the Toolbox is simulated in the three locations considered in this study, therefore taking into account real-world conditions. The Optical and Thermal outputs of the precedent Toolbox simulations are used as inputs together with the cell parameters functions depending on variable irradiance and temperature to deliver the electrical behavior output of the system.

The Electric simulation can be ran over the span of a whole year, and data is collected hourly. The hourly P_{DC} output of the module can therefore be visualised to help understand the yearly trends in DC power output performance. For ease of representation and analysis, Figure 4.3 represents the average monthly DC yield versus the monthly irradiation hitting the plane of array of the module.

It is visible how the monthly energy delivered by the module follows the evolution of weather and seasonal variations during the year. At the same time, in the months that feature a lower irradiance but also lower average temperature, the module's output performance slightly improves in terms of ratio with the monthly plane of array (POA) irradiation. This is because of the lower impact of the temperature effect on the module. The higher the average module temperature, the worse the relative performance of the system will be. Across the whole year, the energy yield produced by the module is 413 kWh/year in Reykjavik, 718 kWh/year in

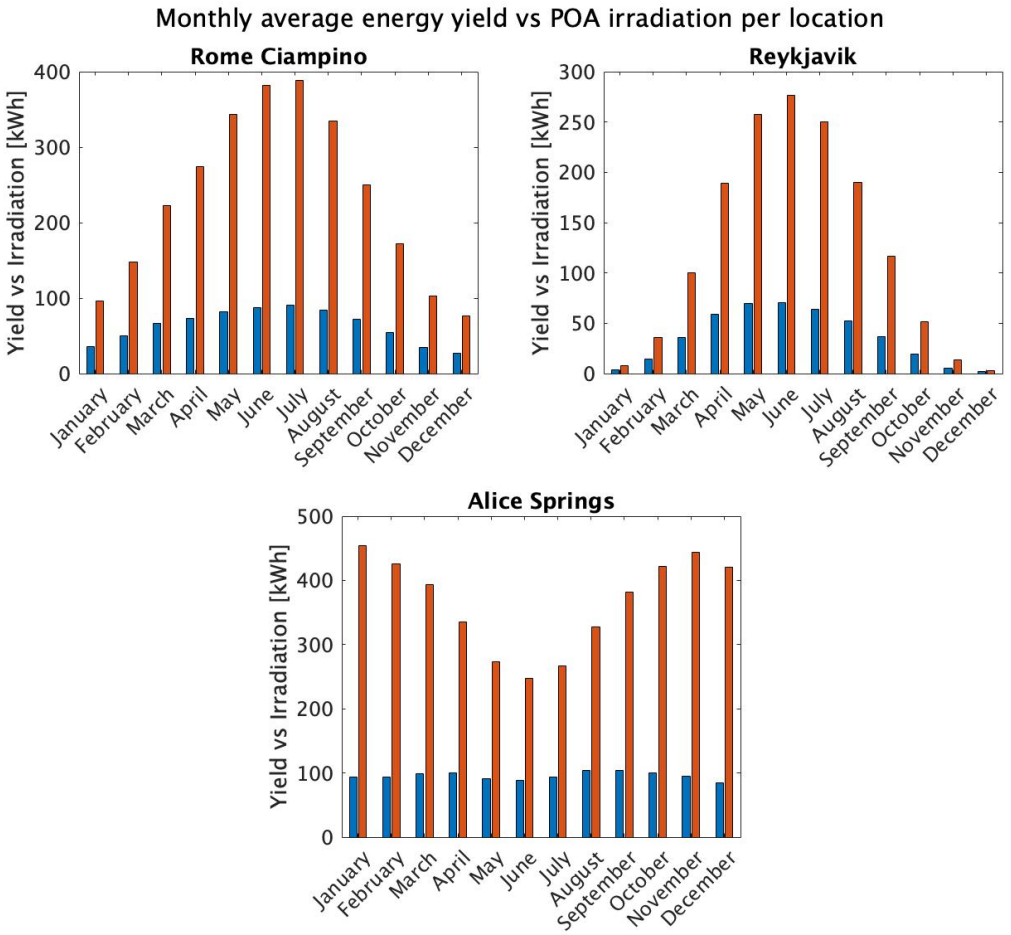

Figure 4.3: The monthly average DC yield of the tandem module (blue) versus the monthly average irradiation the plane of array (red) for each of the three locations considered.

Rome Ciampino and 1,087 kWh/year in Alice Springs.

In Table 4.1 the results of the energy yield prediction simulations are also reported in terms of specific energy yield. The specific energy yield is an important indicator for assessment of PV systems performance in real-world conditions. It is defined as the quantity of energy that is produced per each kWp of system rated peak power during the course of one year. Therefore it can be easily calculated through:

$$SEY_{sys} = \frac{AEY}{P_{sys,rated}} \tag{4.6}$$

where AEY is the annual energy yield and $P_{sys,rated}$ is the STC rated peak power of the system, in this case the simulated P_{mpp} of the tandem module which is 503 Wp.

Location	Specific DC energy yield [kWh/kWp/year]
Reykjavik	820
Rome Ciampino	1,427
Alice Springs	2,161

Table 4.1: The annual specific energy yield predicted for the tandem module system in Reykjavik, Rome and Alice Springs

4.3. DC yield losses overview

The final energy yield values obtained through the Electric model simulation are a result of the whole system performance prediction through the PVMD Toolbox. Such numbers therefore are short of a certain percentage of lost yield. From the Optical to the Electric part there is a propagation of losses that are taken into account through the models implemented in the Toolbox. It is in fact important to evaluate a PV module's performance while considering these elements that can limit its conversion efficiency capabilities and real-world performance. The justification for this lies behind the need to express simulation results that can predict real-world applications in the most realistic way possible. Some of the factors affecting final energy yield results have been already mentioned in this work, but an overview will be provided here based on the categories of losses in PV systems including *fundamental, optical, electrical* and *system* losses. As this study focuses on results of the DC yield of this module structure, it is noteworthy to mention that system losses in this case are considered without the impact of DC/AC conversion, array interconnection and cabling losses. This brief overview of losses from predicting PV modules energy yield with the PVMD Toolbox is based on considerations discussed in the MSc thesis work by Y. Blom and the PVMD Toolbox analysis paper in the works by M. Vogt et al. [59], [87].

Fundamental losses

Fundamental losses include *thermalization*, *below-bandgap* and *emission losses*. These losses are calculated in the first step as they provide the first maximum limit to the solar cell performance. The Toolbox has already been validated in terms of fundamental loss impact calculations or both single-junction solar cells and tandem cells [21], [88]. Within the fundamental losses realm, the Toolbox also features a *gain component* which applies the Urbach's rule, or the fact that the non-ideality of the cell implies a lower emission [89].

Optical losses

The group of optical losses includes all those losses that lead to photons hitting the module area while not being able to generate an electron-hole pair, hence no photocurrent is generated. Part of the optical losses are *reflection, transmission* and *non-generating layers parasitic absorption losses*, which are taken into account and calculated in the Optical model simulation in the Toolbox. The cell absorption function that defines how incident photons lead to photogenerated current is obtained through the GenPro4 software and it already includes the impact of these losses. Secondly, this category also includes non-active area types of losses.

These losses emerge at module level. When defining the module structure with the Toolbox, we consider cell spacing and module geometry which includes borders with the structure sides. As mentioned in Chapter 2 in the module simulation results section, the whole module area is 1.89 m^2. The active area however is lower, equal to the number of cells (72) multiplied by their square-shaped area. This loss can be expressed in percentage of incident power loss. Module performance calculations in this report are based on the module area, hence active area losses are considered in terms of illuminated area loss.

Within the module structure definition, in the Electric part of the Toolbox it is possible to define metallization on the cells, or the space covered by fingers, bus-bars and in general metal contacts between the cells. The consequent loss due to metallization is expressed as a percentage of power lost due to the contacts shading factor and it is considered in the DC power output calculations in the Toolbox.

Electrical losses
Electrical losses include *ohmic* and *recombination* losses. Ohmic losses are calculated through the one-diode model parameters of the cell, in particular through Shunt and Series resistances, in the Electric model simulation where these parameters are inputs. Recombination losses on the other hand are losses caused by electron-hole recombination processes which are however not included in the PVMD Toolbox models yet.

System losses
Among system losses, in this work only two types are considered: *interconnection* and *mismatch* losses which are treated separately below. The first type of loss is taken into account in the Electric model when the user defines the ohmic resistance of the metallization utilised in the cells interconnection. This loss is therefore expressed as power loss and depends on the resistance total value.

Consequently, at this point we can now define a *cell-to-module* (CTM) efficiency comparison. Meaning that we can observe what is the total loss in terms of efficiency when utilising the tandem cell as building block for a module. The single tandem cell features a simulated STC efficiency of 28.4%, while the whole module efficiency is 26.6%. The CTM reduction is roughly 6%. Generally, in commercial PV modules this value is below the 10% mark, with a minimum reached with optimized metal wrap-through modules (CTM loss of 2-3%) [90], [91]. The two efficiencies are obtained considering the active area of the cell and module area, respectively and calculated with the following equation 4.7

$$\eta_i = \frac{Pmpp_i}{A_i \; G_{STC}} \tag{4.7}$$

where i indicates either the cell or module, A is the device area and G_{STC} the STC irradiance.

4.3.1. Mismatch losses and fill factor effect

The mismatch loss is considered based on various factors within the module structure. It has not been discussed previous to the definition of the cell-to-module efficiency as these losses do not affect the overall device STC efficiency calculation but they affect performance in real-world conditions. The mismatch loss comes from the cells composing the module delivering a different maximum power point at the same time, which constitutes a limitation in the overall module power output. This can happen due to variations in irradiance hitting the cells for example with partial shading. Nevertheless, the latter is not much of an issue in this study as we are considering an horizon-free landscape and the irradiance hitting the cells is basically the same over the whole module.

Our interest focuses on the type of mismatch loss happening in tandem cell structures, which has already been briefly presented in previous Chapters. In a tandem stack, mismatch can occur between the two sub-cells other than among all the module's cells. Even without partial shading, this can impact the module performance. The j_{sc}s of the two sub-cells in the module are matched at STC. However, with variable irradiance, spectrum and temperature conditions as in real-world applications, this is not always kept true. One of the two cells can deliver a higher photocurrent, for example when illumination conditions feature a much stronger spectral composition to which the cell's EQE is more sensible and the other's isn't. The whole resulting tandem J-V curve is affected as in a 2T series connection the lowest current dictates the output.

However the resulting tandem *power mismatch* caused by the current mismatch is mitigated by the *fill factor effect* gain. The definition of power mismatch is the relative difference between the tandem power when it is considered in 2T configuration and 4T configuration, hence where there's no current matching constraint. A gain in fill factor means that when the j_{sc}s of the sub-cells are not matched as it happens in variable conditions compared to STC, the fill factor may increase which results in a final tandem J-V curve with a much more steep knee shape although the lower short-circuit current [92], [87]. With a higher fill factor, a more efficient (or closer to ideal) maximum power point can be extracted from the J-V characteristic, hence the lower power mismatch.

To understand the impact of this effect, in Figure 4.4 the behavior of the tandem's fill factor compared to the mismatch peaks is shown over the course of a week in June, for the location of Rome. The STC calculated tandem fill factor is also reported as reference for the fill factor variations. The fill factor values were obtained through the following ratio (eq. 4.8), calculated hourly

$$FF(t) = \frac{P_{DC}(t)}{V_{oc}(t) I_{sc}(t)} \tag{4.8}$$

wher $DCP(t), V_{oc}(t)$ and $I_{sc}(t)$ represent the hourly extracted DC maximum power point, open-circuit voltage and short-circuit voltage of the module. Such time vectors are obtained directly

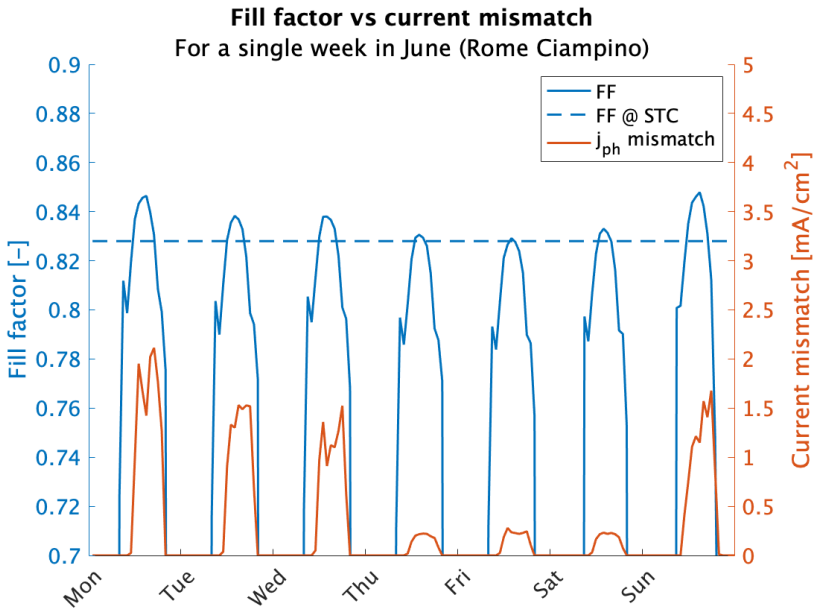

Figure 4.4: The fill factor effect explained through the comparison in fill factor vs current mismatch variations during the course of a week in June, location of Rome.

with the Electric simulation. The current mismatch on the other hand is simply calculated as the hourly difference between the photogenerated current in the top and bottom cell. The reader should note that the location of Rome was taken as example to show the fill factor effect, but a similar conclusion can be reached looking at the trends in the other two locations. When the current mismatch is highest during the week, the fill factor increases if compared to STC which results in a lower loss in terms of power output. The occasions with highest current mismatch can therefore be often well compensated by the relative increase in fill factor. These considerations could however raise the hypothesis in research that optimization of tandem structures should look at power matching conditions rather than current matching. The latter doesn't in fact necessarily translate into higher yield in outdoor applications [92]. This will in fact be the main point discussed further in this work.

Current mismatch and power mismatch of the module can be quantified considering the results obtained so far. A numerical comparison between current losses and power losses can further illustrate how the fill factor gain is an important effect to consider when evaluating 2T tandem performance. It is in fact common to overestimate the current mismatch loss impact when said effect is ignored [59]. This happens when performing optical performance simulations of the device only. This study therefore highlights that to correctly assess energy yield prediction results it is necessary to consider the tandem from an electrical point of view, or where the fill factor effect is tangible. To show this mismatch comparison, a similar analysis as conducted by M. Vogt et al. [59] is carried out. The current mismatch is quantified considering the hourly mismatch sum between top and bottom cells with respect to the sum of the bottom cell current only. The short-circuit current mismatch calculation presented is proper of an optical analysis only. Hence it is the mismatch that affects the implied tandem photogenerated cur-

Location	Short-circuit current mismatch loss [%]	DC power mismatch [%]
Reykjavik	7.95	1.3
Rome Ciampino	5.69	0.9
Alice Springs	6.70	1.1

Table 4.2: Quantification of annual losses caused by the mismatch in current between top and bottom sub-cells, compared to the power mismatch loss reduced by the fill factor effect.

rent values simulated in Chapter 2. The (DC) power mismatch on the other hand is evaluated considering its definition, briefly explained previously, as the power loss going from 4T to 2T configuration. In a 4T configuration, the power of each individual sub-cell can be considered. Table 4.2 reports values of this comparison. It can be seen that the current mismatch is quite high, however the reduction of this loss thanks to the fill factor effect is visible in the resulting DC power mismatch, which is very low. This demonstrates that in energy yield analysis, when considering the mismatch loss issue it is more accurate to take into account the power mismatch rather than the current mismatch, as the former more precisely describes the loss in final yield. In particular, the power loss is highest in Reykjavik which is also the location featuring the lowest specific yield.

4.4. Conclusion

In this Chapter, the Electric simulation of the tandem device adopted in this study has been discussed with the aim of presenting first energy yield simulation results. With this analysis part of the third sub-objective of this thesis has been answered.

Firstly, an overview on the theoretical background behind the application of the cell one-diode parameter extraction method has been provided. This was necessary in order to explain how variable temperature and irradiance J-V curves for both sub-cells are necessary ahead of simulations with the Electric part in the PVMD Toolbox. The curves are in fact utilised to obtain the mentioned parameters which can help describe the electrical behavior of the cell when operating in variable real-world conditions.

Then, the Electric model simulation of the tandem module was performed to obtain energy yield results, for the three locations considered. The highest yield is obtained in Alice Springs, with a value of 1,087 kWh/year. Then in Rome 718 kWh/year and Reykjavik 413 kWh/year. An overview of the DC losses that are considered up to this energy yield calculation was also provided. In particular, the effect of the fill factor gain was explained and shown in relation to the mismatch issue in this 2T tandem configuration. The quantified power mismatch was found to be sensibly lower than the current mismatch between the two sub-cells, proving how the fill factor effect balances the losses in current in a tandem configuration. Additionally, this analysis proves how the power mismatch is a much more accurate parameter to assess

mismatch losses in energy yield analysis.

5

Real-world performance analysis and optimization of tandem module

In this Chapter, the final objective of this thesis work is discussed. From the results obtained in the previous Chapter, the study of this perovskite/c-Si tandem module structure is broadened. The real-world performance of the module structure implemented is analysed with the final aim of maximizing the yearly energy yield and consequently, the system's *performance ratio*. Such analysis is carried out according to the following structure. In section 5.1, the tandem module energy yield results predicted through the Toolbox are compared to those of a c-Si single-junction based module implemented within the Toolbox. The differences in energy yield show how tandem technology can offer improvements over established technologies in real-world applications. Then, section 5.2 presents the topic of performance ratio analysis for the tandem structure as it was simulated in Chapter 3 and introduces the need for real-world optimization. Finally, in section 5.3 the tandem is studied for different perovskite thicknesses with the aim of maximizing energy yield per location and the performance ratio, answering the main research question of this report.

5.1. Comparison with single-junction module performance

To begin a deeper analysis of the real-world performance of the tandem, a technology comparison in terms of energy yield prediction is carried out. It is useful to observe the differences between the tandem structure and the performance of a single-junction technology solar cell. In particular, we compare to a silicon poly-SiOx based solar cell of the same kind as employed in the tandem structure. Together with observing the differences in performance among the cell types, this comparison can also contribute to the justification of tandem technology research when demonstrating how it can potentially increase the power output per unit area with respect to its single-junction solar cell counterparts. It can also show how different technologies perform in different climates and consequently how we can aim at exploiting each cell type behavior in real-world applications.

Comparing different systems performances is possible through running the Toolbox again for the single-junction c-Si cell alone, hence utilising the same PV modeling approach. The process starts by implementing the cell layers on the GenPro4 software, and the simulation can then be ran for all five parts as previously considered for the tandem structure. All three locations are considered again in the performance simulation as to more comprehensively compare the results to the ones previously obtained for the STC-optimized tandem.

Ahead of the energy yield results, in Table 5.1 some specifications for the module utilised to run the simulations are gathered. The structure of the module itself is the same for both c-Si and tandem technology, in order to make the comparison valid and consistent. In other words, a 72-cells c-Si module is implemented. All geometrical and metallization parameters of the module structure are the same as for the tandem. The efficiency reported for the sub-cell is calculated from the resulting STC power rating of the module, which is also reported in the Table. It should be noted that these values are obtained through simulation of the implemented cell structures within the Toolbox and do not correspond to any experimentally measured device. Although STC efficiencies of the cell and tandem can be validated in terms of values range in literature of similar technologies [93], the prediction of the cells and modules performances as implemented on the Toolbox provide insights on a potentially optimal case. Here, we don't take into account for example losses of the actual physical cell or module which emerge after fabrication of the structure and that are featured when measuring the cells and modules experimentally. Only the losses implemented in the Toolbox as discussed in the previous Chapter are considered. Nevertheless, these calculations already prove that the tandem configuration is able to deliver approximately 31% extra power output in STC if compared to the c-Si module.

To understand if this STC gain also translates into real-world performance improvements, we look at annual energy yield results for both modules. In Figure 5.1, the bar plot indicates total DC power output over a full year for the three locations of Rome, Reykjavik and Alice Springs. Above each result for the tandem module, the relative gain in terms of yield is indicated with respect to the c-Si module. It can be observed that the performance improvement is much more evident in a location like Alice Springs rather than in Reykjavik. The reason for this is the fact that tropical and equatorial regions feature a much more blue-rich spectrum and lower air mass index.

Technology	Module area [m^2]	STC module efficiency [%]	STC module power rating (P_{mpp}) [Wp]	STC P_{mpp} gain [%]
c-Si (poly-SiOx)	1.89	20.4	385	-
pvk/c-Si Tandem	1.89	26.6	503	+31

Table 5.1: Specifications for the c-Si single-junction vs tandem comparison. The table reports STC efficiency and power rating of both technologies, together with the STC power output gain obtained from the tandem.

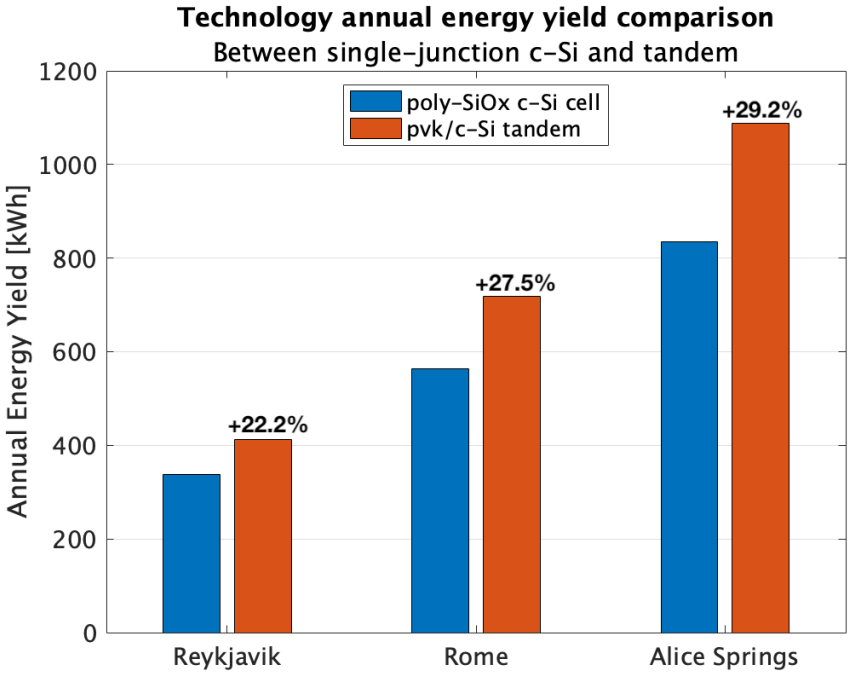

Figure 5.1: Comparison between c-Si and tandem module energy yield simulated for the three locations. The relative increase in annual yield is reported over the tandem module value.

The presence of the perovskite top sub-cell, which is spectrally more reactive to higher energy photons, increases the output in those areas more evidently. Moreover, the better performance from the tandem compared to the c-Si module in higher average temperature locations can be explained with module temperature considerations. Here in fact the tandem exhibits lower average module temperatures throughout the year against the reference module, which is theoretically due to reduction of thermalization losses in the tandem structure [59].

In addition to the energy yield value comparison, the Table below (5.2) compares the specific energy yields of the two different technologies. In all locations, the tandem specific yield is smaller than the c-Si counterpart, while the performance is still comparable to the reference. Location and therefore climate and illumination conditions play the most important role in this specific yield comparison. This can be seen in the reduction of the relative loss towards the location of Alice Springs.

Location	c-Si SEY [kWh/kWp/year]	Tandem SEY [kWh/kWp/year]	Relative gain/loss [%]
Reykjavik	847	820	-3.2
Rome Ciampino	1,458	1,427	-2.1
Alice Springs	2,171	2,161	-0.5

Table 5.2: Comparison between tandem module specific energy yield and reference c-Si module.

5.2. Tandem module DC performance ratio analysis

Observing the values of DC power output and annual energy yield is a great way to assess the behavior of PV systems when considering real-world applications. However, in photovoltaics there is another parameter that can add more to the energy yield analysis, especially when it comes to seeking performance optimization. Such parameter is the *performance ratio* (PR) and it is used to complete the PV system outdoor field performance characterization along with annual energy production. The performance ratio describes how a PV system can perform in real-world applications compared to its STC behavior, which is of great interest within this study [48], [94]. It can be in fact expressed, in its simplest form, as the ratio between the typical real-world efficiency of the system and its STC efficiency. The values of PR range between 0 and 1 (or expressed in percentage), where 1 means that the device is able to produce the same amount of energy outdoor as if it was in standard test conditions. Rarely, theoretical values of performance ratio can also be over 1 where particular location and weather conditions allow the system to perform better than in STC over the span of time considered. PR is also of great importance when conducting financial prediction analysis for PV systems.

Typically, the performance ratio is assessed for a whole system such as residential/commercial installations, PV parks and power plants. This means that usually the calculation of this parameter is done empirically from the incoming irradiation on the module, to the final AC yield of the system. As a result, the final percentage takes into consideration all possible losses that occur in the physically implemented PV system. Therefore, due to the many loss mechanisms that chip away at the operational efficiency, studies have demonstrated that an AC performance ratio for a PV plant is in practice almost never over 0.9 [95]. Values of performance ratio for typical PV systems such as standard c-Si-based ones used to be in the range of 70% before the 2000's. Recent progresses in photovoltaics and BoS efficiency combined have raised this average to oscillate between 80% and 90%, depending on technology, system architecture type and location [96], [95].

As explained in Chapter 4, the Toolbox as it is evaluates many of the losses that affect final power output on both the DC and AC side and consequently performance ratio evaluation, although a few are still not included. One of them is the light polarization effect. In the Toolbox, light is assumed to be unpolarized. However, in real systems we can estimate an extra reflection loss due to this effect from 2% up to 5% on the performance ratio calculations, depending on sky conditions [97]. This effect is also particularly complicated to model into an energy yield simulation system as the Toolbox. Moreover, it is noteworthy to reiterate that in this study the sole DC power output of the tandem module is taken into consideration for performance analysis. This means that when calculating the PR of the module in real-world conditions, some quite relevant losses are not taken into consideration. In particular, when calculating an AC yield based performance ratio, the DC/AC conversion has a great impact on the final percentage. Part of these losses are due to DC and AC cabling and inverter (with maximum power point tracking) efficiency. Linked to this is the arrangement of the PV system itself. Some losses are due to the type of connection between the modules (e.g. string connec-

tion) and limitation of the system output from the maximum power point mismatch between the modules. In real-world PV plants or rooftop systems it is also quite impossible to avoid shading losses from accidental object interactions, surroundings or even other modules in the system. As a reminder, in this work simulations are carried out considering a completely free horizon, hence possible shading losses are not included.

In summary, when comparing a single module DC output to a whole system's final AC output, literature references report a possible lowering in terms of performance ratio percentage of up to more than 10%, when considering all the extra losses [97], [98], [99]. Consequently, what is expected as result of the DC performance ratio analysis for this tandem module's yield is for the results to be generally higher than typical PV systems values. Hence the reader should note that when considering a whole system made of tandem modules of this kind, at the AC point of interconnection (POI) the PR will most likely show lower values in any location considered. This can be further explored in future studies looking at energy yield analysis of tandem modules.

For this analysis, performance ratio reference values will be the work introduced in Chapter 1 on tandem outdoor potential theoretical comparison by H. Liu et al. [48]. In their study, multiple types of tandem architectures are analysed, including perovskite-on-silicon, and different locations around the world are considered. Hence, it is a valuable source to validate results obtained through the Toolbox simulations. Moreover, their theoretical comparison is based on simulations that use an illumination spectrum approximated with the SMARTS model, which is the same as it is utilized by the PVMD Toolbox. The type of performance ratio analysis in their work is also based on the same assumptions that only DC single-module output is considered, with no optical, shading or other system losses included. Therefore, results higher than typical PV plant performance ratios are obtained.

5.2.1. DC performance ratio calculations and analysis

To proceed with performance ratio analysis, in this study we define the parameter through the following equation [94], [100]:

$$PR_{DC} = \frac{AEY}{\eta_{M,STC}\ A_M\ G_{POA}} \tag{5.1}$$

where AEY corresponds to the module's Toolbox-predicted DC annual energy yield, $\eta_{M,STC}$ is the module's STC efficiency, A_M is the area of the module and G_{POA} is the yearly POA irradiation for the location considered. The denominator in this equation represents the reference yield, hence the relation and source of normalization with respect to STC performance for the performance ratio. In other words, it is the ideal energy yield that the module would produce if it was constantly working at its rated power output.

Location	Energy yield [kWh/year]	Performance ratio (from eq. 5.1) [-]	Performance ratio (from real-world η) [-]
Reykjavik	413	0.968	0.960
Rome Ciampino	718	0.956	0.947
Alice Springs	1,087	0.948	0.939

Table 5.3: Performance ratio values calculated for the three locations, from annual energy yield values and STC device performance.

From the simulated STC efficiency, irradiation and energy yield values previously obtained, the PR is therefore calculated for each of the three locations. Table 5.3 reports PR values for the STC-optimised tandem structure. Together with results of these calculations derived directly from the Toolbox simulation, Table 5.3 also reports PR values obtained through the ratio between the average operative efficiency of the module and the STC efficiency. This is a manual check carried out to assess results consistency. The average operative efficiency can be computed based on each location's typical weighted average irradiance and temperature, to consider the effect of low irradiance/high temperature losses on the performance ratio. This can be done for example by ovveriding irradiance and module temperature values with each location's average in the Toolbox simulations. Results between the two different PRs are slightly deviated due to the different calculation methodology, while still exhibiting the same trend.

We can observe that the highest value of performance ratio is obtained in the location of Reykjavik. The explanation for this lies behind the characteristics of the weather conditions differences between the locations and the real-world behavior of the module. Generally locations closer to the equator experience higher average temperature conditions over the year which negatively affect the module performance. A higher module temperature causes operating efficiency to be lower, consequently reducing the power output of the module during hotter hours. This is not the case for Reykjavik, where temperature reaches lower values during the course of the year. In fact, the lower average module temperature (approx 16.04℃) is well below the standard 25℃ which theoretically causes improvement in performance. Such improvement is however partly negatively compensated by the lower average irradiation per year. In Rome and Alice Springs, temperature loss is relevant (average temperatures of 36.86℃ and 45.57℃, respectively) but the irradiance loss is much smaller thanks to a better average irradiation. According to H. Liu et al., in extreme high altitude regions it is even possible to achieve a DC performance ratio higher than 1 through temperature effect gain [48]. Nonetheless, this is of course affected by the lower overall yearly energy yield performances in higher latitude areas.

The presence of the poly-SiOx passivated cell as bottom cell in the tandem is also playing a quite relevant role in the final performance ratio evaluation. TOPCon cells in general offer a better performance in higher temperatures, which is also reflected in a lower high temperature loss in the warmer climates of Rome and Alice Springs. This has also been introduced along with temperature coefficient calculations in Chapter 3. Such coefficient is in fact generally

lower compared to other c-Si structures (up to -0.15%/°C difference). With this remark, a benefit of employing TOPCon cells in tandem structures is highlighted.

In Figure 5.2, results of the analysis by Liu et al. are shown for their 2T perovskite/c-Si tandem configuration, in terms of performance ratio and energy yield. Both parameters are represented in the form of a probability distribution plotted over a geographical map of the world. If we consider the geographical areas of the three locations from this thesis work, the probability of their respective DC PRs showing the same values and trends as in Table 5.3 is quite good. It is highest in the high altitude region of Reykjavik, and closer for Rome and Alice Springs, with a lower value. At the same time, their representation of energy yield values distribution can be compared to results of the Electric simulation carried out within the Toolbox. Energy yield in H. Liu et al. is expressed in the form of yield per area. It is then required to divide the three yields previously obtained with the tandem module area (1.89 m^2). This equals to 216 kWh/m^2, 380 kWh/m^2 and 571 kWh/m^2 for the locations of Reykjavik, Rome Ciampino and Alice Springs, respectively. Using the lower heat map in Figure 5.2 as a guide, these values can be validated with a good degree of approximation.

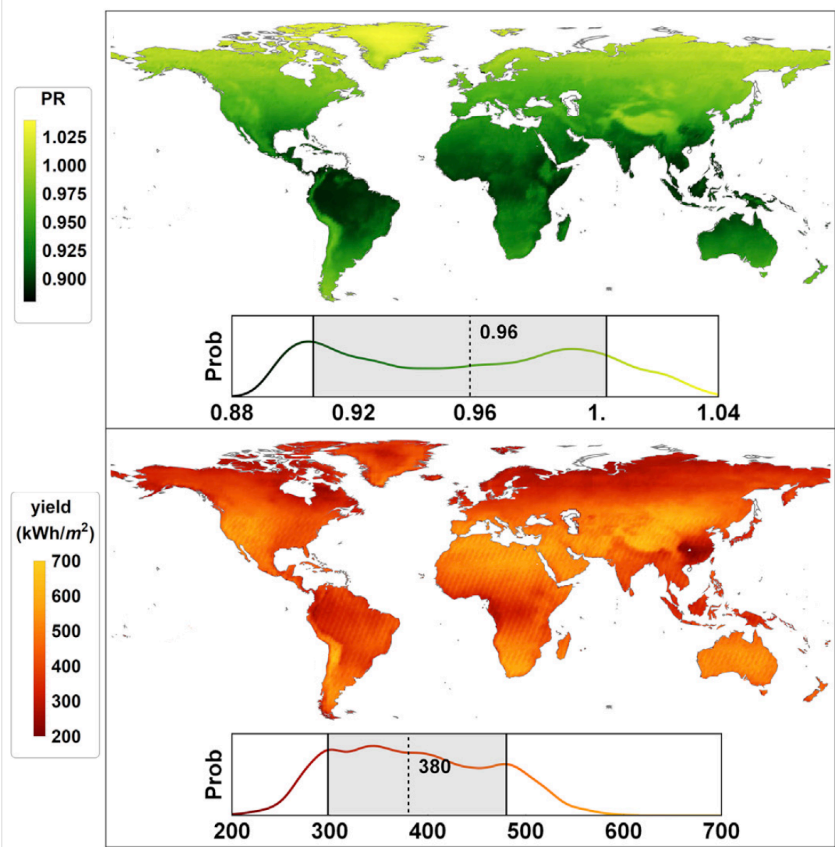

Figure 5.2: The performance ratio and energy yield analysis as it is carried out by H. Liu et al. PR and EY values are represented as a probability distribution heat map plotted over a geographical world map, to identify different climate areas [48].

5.3. Optimization of tandem module real-world DC performance

In this Section, the final objective of this thesis work is treated. The analysis of the tandem module system has been discussed already through presentation of energy yield and performance ratio results. The values obtained however come from simulations that consider an STC-optimized tandem structure, where the tandem cell is implemented with characteristics that aim at delivering the optimal 2T photocurrent resulting from the two sub-cells when irradiance, temperature and illumination spectrum are kept constant throughout the simulation.

In previous Chapters, it has already been stressed out that these parameters are not applicable when performing energy yield calculations as the variations in weather conditions throughout the whole year, per each location, are taken into consideration. Consequently, when simulating an STC-optimized structure to obtain real-world energy yield predictions it can be confidently assumed that the results are not optimal. The aim here is however not to seek the highest value of energy yield possible in general, as it would be otherwise easy for example to simply propose to install all PV tandem systems in a location like Alice Springs where yearly irradiation allows for highest values of energy extracted. The goal is to maximize the performance of the tandem module at the different locations considered to explain how variations in the cell structure can help reach higher outputs, for different climatic conditions. Furthermore, as in this work the performance ratio factor is also adopted as a parameter to assess outdoor module performance, we look at how the optimization of the tandem structure can help increase such parameter at each different location. This modeling approach can therefore help provide a comprehensive picture of the PV system behavior as we aim at implementing and introducing tandems as a commercial type of technology for energy production worldwide.

5.3.1. Effect of perovskite thickness variation on energy yield

From a modeling approach point of view, the most immediate and effective way of changing the performance of a PV cell (and consequently module) is to play with absorber thickness variations. In particular, just as it was done when seeking STC-optimization it is possible to change the model cell structure by increasing (or decreasing) the thickness of the perovskite top-cell absorber layer. The difference with the STC optimization method however lies in the ultimate goal. While for the latter the aim is to obtain a current matching condition between sub-cells in order to reduce mismatch losses at STC, the optimization for real-world conditions looks at maximizing the energy yield output from the system. This equals to finding the optimal structure when accounting for all operational conditions losses that can reduce the performance of an STC-optimized cell.

The procedure therefore consists in simulating the Electric model for the tandem module multiple times, or for each variation in which the cell features a different perovskite absorber thickness. In particular, the range of thicknesses adopted for this analysis is based on the study on real-world photocurrent output optimization by M. Singh et al. [18], where the same tandem structure is adopted and therefore a partial validation of results will be made possible.

However to do so, it is necessary to again employ the Toolbox to first simulate optical and thermal behaviors of the new type of cell. Firstly, the layered structure of the tandem is then once more implemented on the GenPro4 and the absorptance function calculated at different perovskite thicknesses. Then the same module structure is generated for simulation with the Lux software, and the climate conditions applied with the Weather and Thermal models. Finally, when running the Electric model the same one-diode parameters that were previously calculated for the STC-optimized structured are employed. This is possible thanks to the fact that the c-Si bottom cell has not changed. It is however relevant to mention that an assumption is made here for the perovskite one-diode parameters. Variations of the perovskite thickness are in fact only considered to affect the photogenerated current, while the other parameters remain unchanged. Theoretically, other parameters can also change, together with open circuit voltage. The photogenerated current is in fact calculated through Optical simulations within the Toolbox, however in order to obtain more realistic parameters that are thickness-dependent, it would be necessary to simulate (or measure) J-V curves for the perovskite cell at each of the considered thicknesses.

The perovskite absorber thicknesses considered are within the range of 450 nm to 650 nm, varied in constant steps of 25 nm [18]. Hence, 10 different cells are simulated and the results compared, including the STC-optimized one at 515 nm. All the locations of Reykjavik, Rome and Alice Springs are studied, as it is interesting to observe what is the effect of varying the perovskite thickness and how it is possible to deliver the maximum performance in each of the three areas. Figure 5.3 reports the trends of the specific energy yield functions normalized with respect to the module peak power, depending on the perovskite thickness, for the three locations. In the three graphs, the optimum can be easily identified.

The range considered is populated enough to give a proper idea of the trend, and the optimum can be approximated with an acceptable degree of precision. Of course a much higher granularity of samples would bring a higher precision in finding the optimum, however with barely perceptible variations in final energy yield values. For a comparison to STC, the values of specific yield for the 515 nm initial thickness are highlighted.

In Reykjavik, the optimum thickness is 600 nm, which is much higher than the STC-optimized one. This is because the illumination conditions in that area feature a less strong blue component in terms of spectrum, as the AM index values are much higher on average. Hence, the perovskite needs to be thicker to compensate the absorption of the stronger infrared component by the silicon sub-cell, and consequently increase power output. The optimal value of specific energy yield reached here is approximately 827 kWh/kWp/year. In Rome on the other hand, the optimal value of thickness is observed to be the same as in the STC-optimized structure. Here on average air mass, spectrum and irradiance are much more consistently similar to those that apply in STC thanks to the location altitude. Finally, in Alice Springs we see that a smaller perovskite absorber layer is needed to optimize the structure, at approximately 500 nm, due to the lower average AM and higher irradiation. Also, in opposition to Reykjavik here the infrared spectral component is much weaker than the blue one. This delivers an annual

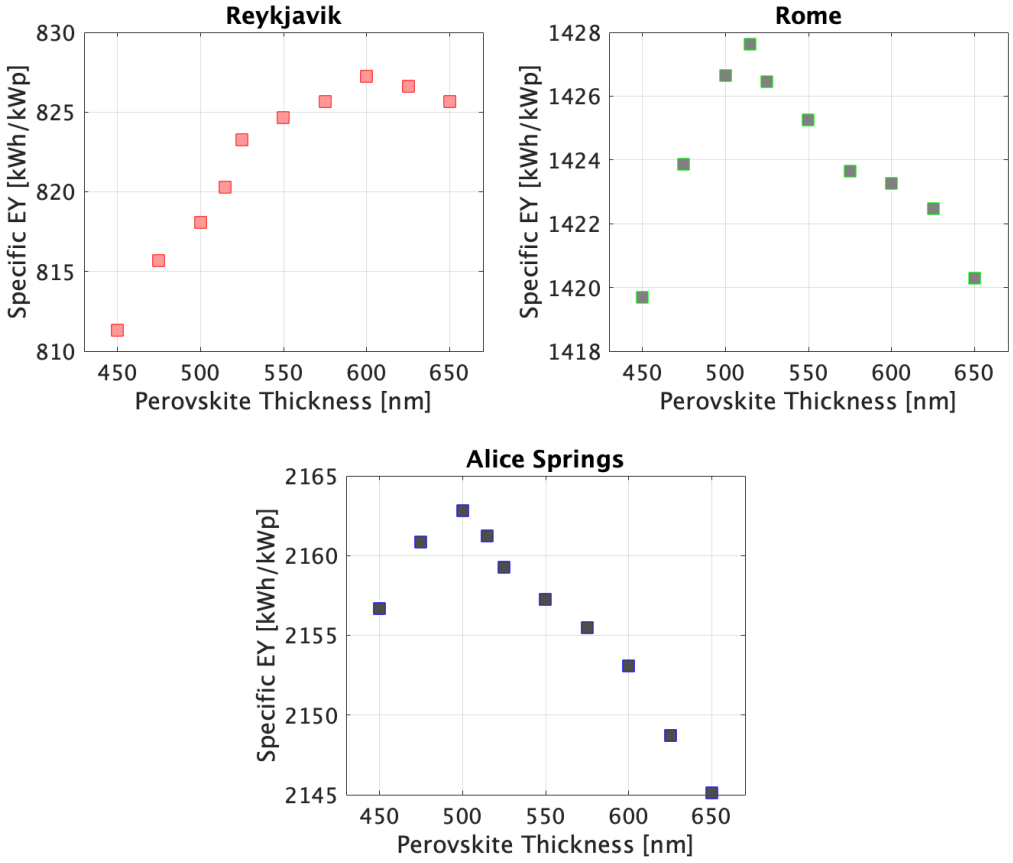

Figure 5.3: The specific energy yield as predicted for the three locations, for variable perovskite thicknesses.

specific yield of 2163 kWh/kWp/year.

As previously introduced, validation of these results is possible by comparing with the real-world optical performance analysis carried out by M. Singh et al. The cell utilized in their study is the same as presented in this work, and the locations considered (hence weather conditions) are also equal. Although in M. Singh et al results are expressed in terms of cell's photogenerated current output optimization depending on perovskite thickness, the trends observed when varying the thickness are supposed to show the same behavior, as increasing average current output also leads to higher energy yield values. Nevertheless, the optimal thickness for performance maximization is approximately the same for all three locations respectively.

5.3.2. Performance ratio of optimized tandem module

As it was done for the STC-optimized tandem structure, the performance ratio parameter is also adopted here to assess system performance together with energy yield analysis. The PR is calculated through the same equation previously introduced, though by taking into consideration the location-specific increase in energy yield production over the year resulting from the optimization procedure.

Location	Energy yield (real-world optimized) [kWh/year]	Performance ratio (real-world optimized) [-]	Relative PR gain [%]
Reykjavik	416	0.974	0.62
Rome Ciampino	718	0.956	-
Alice Springs	1,089	0.950	0.21

Table 5.4: Analysis of tandem module performance ratio after optimization for real-world energy yield maximization. A comparison in terms of relative gain from the STC-optimized PR is reported as percentage increase.

In Table 5.4, the optimization of performance ratio is summarized and compared to the non-optimized structure. The biggest leap in terms of PR improvement is visible for the location of Reykjavik. This is because the optimal perovskite thickness that delivers the highest yield is much more different than the STC-optimized thickness, hence the PR varies more sensibly. In Alice Springs, the difference is much less perceived as the ideal perovskite thickness is only slightly thinner than the original 515 nm, hence the contribution in terms of perovskite absorption variation to the energy produced over the year by the module is smaller. The module's PR in Rome remains unchanged as the optimal tandem structure is the same as in STC.

5.3.3. Considerations on tandem design optimization

The goal of the energy yield and performance ratio optimization analysis carried out in this Section serves the purpose of showing the potential of perovskite/c-Si tandem technology in different areas of the globe. As this PV technology is yet to be fully commercialized, the evaluation of such performances can aid manufacturers and research in the quest of targeting the best architectural and structural options to produce.

Customization of module design is linked to the topic of real-world and location-specific optimization. For technologies that are very sensible to typical climate and illumination conditions in some areas, manufacturers can consider the option of adapting the design of the tandem module starting from the cell. This includes the already discussed variation of perovskite thickness in order to increase/decrease photogenerated current in locations where the power mismatch is not optimized. Results obtained within this work show that the maximization of energy yield brings a quite marginal increase when we compare to the STC-optimized tandem cell structure. On average, this reflects in a gain of few percentage points over the standard yield. Considering the actual development of tandem manufacturing and commercialization, this gain would most likely not justify customization of design for many different locations as the benefits might not overcome the economical effort to carry out the process. More likely, the globe could be divided in a few climate areas for which the average optimal perovskite thickness is advised to be employed in the cell structure.

Together with perovskite thickness optimization, manufacturers and researchers can look into

perovskite bandgap variations. The tunability of the perovskite bandgap is in fact one of the biggest advantages of employing such material. It allows for a much more efficient use of the available illumination spectrum. So far, research has been focusing on optimizing perovskite bandgap according to STC conditions (such as for the cell design in this work). With the aim of maximizing real-world performance and annual energy yield, together with optimizing the thickness of the perovskite absorber, the perovskite bandgap can be adjusted to best fit the location area according to the typical illumination spectrum. By increasing the perovskite performance with the tuned bandgap [101] in tandem with the bottom silicon, the overall real-world efficiency of the module can be increased.

Finally, the c-Si bottom cell structure can also be considered for device optimization. Other than increasing the cell performance by further enhancing the TOPCon design, the thickness of the silicon absorber can be adjusted together with the perovskite one in order to possibly deliver higher power output.

5.4. Conclusion

In this Chapter, the ultimate objective of this thesis work has been expounded and its final outcome analysed. This Chapter concludes the answer to the third sub-objective and answers the main research question.

Energy yield results obtained in Chapter 4 have been analysed by first demonstrating the better performance compared to a reference c-Si module. Through all locations considered, the annual energy yield gain spans from 22.2% in Reykjavik, to a highest 29.2% in Alice Springs. In terms of specific yield, the tandem shows however a slight relative loss against the c-Si module. Successively, the performance ratio of the module has been analysed from the DC perspective. Reykjavik features the highest PR with a value of over 0.96, while the lowest is obtained in the location of Alice Springs.

Consequently, the goal was to optimize the tandem module performance in real-world conditions considering the three climate and weather reference locations. The effect of varying perovskite thickness is therefore simulated through the PVMD Toolbox, and final yield results compared to the STC structure. Improvement in terms of yield is achieved in particular in Reykjavik. Such values of energy yield are then used to re-calculate the performance ratio of the optimized system and to show the relative gain in real-world performance. A slight improvement for Alice Springs is shown, no improvement for Rome as the STC thickness is optimal for such location, and a higher improvement in Reykjavik.

6

Conclusions and Recommendations

In this Chapter, results achieved while aiming at answering the thesis objectives as explained in the first chapter are summarized. Moreover, recommendations for further studies on perovskite/c-Si tandem module energy yield are provided in section 6.4. The main research question set as goal for this thesis work was to achieve the

Optimization of perovskite/c-Si tandem module for energy yield maximization under real-world conditions.

In order to answer this, sub-objectives were defined and their respective answers are summarized in the following sections.

6.1. Implementation of tandem structure in the PVMD Toolbox

The first aim of this sub-objective was to define the structure of the tandem device adopted in this study. The 2T layers stack has been therefore detailed by explaining the presence of performance improving and protective layers, together with the composition of each sub-cell. This structure was then implemented in the PVMD Toolbox with the use of the GenPro4 software. Through this software, the cell's optical behavior was simulated and its absorptance, reflectance and transmittance functions obtained for different angles of incidence. These results are successively employed to calculate absorbed power and implied photocurrent of the device. As this optical simulation was carried out in STC, optimization of the cell was confirmed for a perovskite thickness of 515 nm and a 2T implied photocurrent of 19.5 mA/cm^2.

From this base cell structure, a 72-cells module was constructed and its geometry defined in the Toolbox. Considering module spatial positioning, the Lux software was employed to obtain the Sensitivity Map of the module. Such Sensitivity Map describes how the module responds to illumination depending on the angle of incoming irradiance and is used in irradiance and photocurrent calculations. This Map was simulated in the two different azimuth orientation

of South and North to account for the different hemispherical positioning of the considered locations.

Real-world conditions are applied in the Weather and Thermal models of the Toolbox. The first utilizes the Meteonorm data for DNI, DHI, GHI and sun position to reconstruct an illumination setting based on the SMARTS model to which the module is exposed. Results of these simulations allowed to compute the implied photocurrent density of the tandem. Such values are expressed on a hourly basis in the Toolbox. The average yearly simulated photocurrent density was found to be 1.92, 3.34 and 5.01 mA/cm^2 for the considered locations of Reykjavik, Rome and Alice Springs, respectively. These values of photocurrent include the effect of the current mismatch caused by the illumination variation conditions in the 2T configuration. Further in the report they have been quantified to be between 5 and 8% depending on location. To validate the results and the Toolbox calculations, a manual check was carried out on the photocurrent values. Considering yearly irradiation, a current ratio was obtained for all three locations describing the ratio between ideal STC photocurrent and theoretical average yearly photocurrent. With a small deviation, these calculations confirmed the results obtained with the Weather model. From the latter, absorbed power was also calculated for each module cell, leading to hourly temperature estimations through the fluid-dynamic model implemented in the Thermal model. The highest temperature is reached in Alice Springs, where the module operates at an average temperature of roughly 46℃. In Reykjavik the average operating temperature is on the other hand lower than the STC 25℃. These results are relevant as they showed an important effect on subsequent yield calculations.

6.2. Experimental characterization of poly-SiOx c-Si bottom cell

To take into account the behavior of the tandem with variable operating and weather conditions, the J-V curves at variable irradiance and temperature were gathered for each sub-cell. These allowed to extract the functions defining the one-diode parameters of the cell. For the perovskite top cell, such curves were retrieved from previously performed ASA software simulations, where the single-junction cell structure was defined and simulated under variable irradiance or temperature for a wide range of values.

For the poly-SiOx based silicon bottom cell, thanks to the physical availability of the device it was possible to characterize the variable conditions J-V curves through an experimental procedure. Such experiment involved use of technical equipment available in the ESP laboratory at TU Delft. The cell J-V sweeps were performed for variable temperatures employing a gold-plate NIP stage that allowed cell temperature variations from 15 to 55℃. The resulting curves exhibited a behavior typical of the temperature increase effect: slight increase of photogenerated current density, together with a more evident decrease of open circuit voltage. For the irradiance measurements, intensity reduction polka dots filters were placed over the cell at STC temperature, and the irradiance varied between 200, 500, 800 and 1000 W/m^2. As the irradiance hitting the cell diminished, the photogenerated current was scaled down and the

J-V curve flattened consequently.

Thanks to theoretical considerations, these measurements were validated before proceeding with the electrical simulation of the tandem. The variable temperature measurements were confirmed through comparison of the empirically obtained temperature coefficient with typical TOPCon solar devices. A temperature coefficient of approximately -0.303%/°C was calculated and validated. For the variable irradiance measurements, it was possible to compare the measured short circuit current of the cell to the theoretical photogenerated current calculable with the illumination spectrum, cell EQE and filters transmittance. Though a small error deviated the measured values from the theoretical ones, the curves can be confidently assumed to be correct for all irradiance measurements.

6.3. Energy yield prediction, real-world performance analysis and optimization.

The third sub-objective is directly linked to the main research question of this thesis. After performing Optical to Thermal simulations, and gathering the variable conditions J-V curves, the Electric part of the Toolbox was ran. From the J-V curves, a parameter extraction method previously implemented within the Toolbox allowed to obtain polynomial coefficients of the one-diode parameters to be used as input in the Electric model. For both perovskite and c-Si cell, these are used to reconstruct the hourly I-V curves which are then coupled in the final tandem curve. The reconstruction of these curves is dependent on the the photogenerated current as simulated through the Optical part of the Toolbox. From the I-V curves, the Toolbox extracts the maximum power point at each hour of the simulation and consequently the DC power output and annual energy yield is obtained. The specific energy yield for each location comes out to be 820 kWh/kWp/year in Reykjavik, then 1,427 kWh/kWp/year in Rome and 2,161 kWh/kWp/year in Alice Springs. These values take into consideration certain losses on the DC side that have been implemented in the Toolbox. An overview of these losses has been provided. This overview mostly focused on explaining how from an electrical point of view, the fill factor gain effect causes a compensation in current mismatch losses between the two sub-cells. This means that the final energy output of the system losses are reduced as the power mismatch is minimized with the fill factor effect, to small values between 0.9 and 1.3% loss. This proves how the power mismatch is a much more accurate parameter to assess mismatch losses in energy yield analysis. Together with energy yield calculations, the module simulated STC ratings are also obtained. At STC, the module delivers 503 Wp with a module efficiency of 26.6%.

Energy yield results were compared to a reference single-junction poly-SiOx based silicon module. In terms of absolute yield, the tandem proves to be better performing in all three locations considered. In particular, the highest increase in terms of yield is seen in Alice Springs where the more evident blue-rich part of the spectrum allows for up to 29% performance increase compared to the c-Si module. In terms of specific yield the tandem shows a relative loss per

kWh/kWp/year, highest in Reykjavik.

To assess module performance, the performance ratio parameter is considered in this study. Particularly, the DC ratio was calculated for the tandem system. As explained in Chapter 5, such PR is proper of the DC side single module performance. Therefore, although calculated in the same manner as for PV plants and systems, some losses are not taken into consideration. This led to an expected higher PR value than typical PV systems ones. The performance ratios for the locations span from the lowest 0.948 value for Alice Springs, where the highest average temperature causes operative losses, to a highest of 0.968 in Reykjavik where the low average temperature compensates the low irradiance losses on the module. The PR values obtained depend on many factors and vary across locations due to temperature but also different illumination conditions in terms of typical spectrum composition and AOI. Nonetheless, these results were validated through manual calculations and a literature reference work which also confirmed energy yield values for the tandem.

The main research goal was answered through the analysis carried out in Chapter 5. To maximize the performance of the module in real-world conditions, the tandem structure has been optimized depending on location-specific conditions, by varying the perovskite thickness. To do so, the PVMD Toolbox models have been run again for the different base cell structure, and all energy yield results compared. The variations of the thickness considered were in the range of the 515 nm optimized one, both thicker and thinner. For Rome it resulted that the STC thickness provided the maximized yield already. This is because the illumination spectrum and climatic conditions in Rome resemble the STC ones more than the other 2 locations. For Reykjavik, the most sensible variation of perovskite was seen to deliver the highest possible yield. The latter grows by few points percentage with respect to the STC-optimized yield when increasing perovskite thickness, leading to a consequent growth of PR of about 0.62%. This is because the infrared part of the spectrum is stronger and the bottom cell produces more current than the top cell, which needs to be matched as much as possible. In Alice Springs, the perovskite already produces more photocurrent than the silicon bottom cell. Hence, a thinner absorber is needed. The variation of energy yield is less acute than in Reykjavik, and so is the PR. From these results, manufacturers of tandem modules can take into consideration how performance can vary around the globe and to what extent customization of tandem design might be needed to exploit better performances. A proper answer to this can only be given considering the economical aspect of differentiating production based on the location. Some other considerations on how to further increase energy yield maximization were also provided.

6.4. Recommendations

The tools and methods utilised to conduct this research work have been thoroughly described throughout this report. Although results and conclusions reached have been analysed and validated, the aim of this section is to provide recommendations on improvements to be adopted in the simulation models and methodology in order to overcome some limitations. Moreover, a

few recommendations are given on how to extend and further deepen the topic of perovskite/c-Si tandem PV systems energy yield prediction through future research.

PVMD Toolbox models

- **Irradiance model**: as it's been pointed out in Chapter 2, the irradiance model that the PVMD Toolbox employs to simulate real-world illumination and variations is developed in a quite simplified fashion. It is based on the SMARTS spectral reconstruction model, where the spectrum is approximated using the position and altitude of the sun. As a tandem structure is very sensible to spectral variations, a more accurate version of the illumination spectrum simulation method would be needed to obtain results that are more precise. In addition, the Perez sky model implemented in the Toolbox could be substituted with a more complex method (such as the Preetham model) that takes into account more factors influencing spectral composition.
- **Parameter extraction method**: the employed parameter extraction method has lead to good final results in terms of energy yield. However, for a more precise reconstruction of the J-V curves at variable operating conditions, future Toolbox operators could look into expanding the extraction model possibly even considering different methods. In particular, if spectral variations J-V measurements are available, it would be more accurate to base the parameter extraction method on photogenerated current variations rather than irradiance, as the former is dependent on the incident spectrum. Using irradiance in the parameter extraction however justifies the use of scaled down irradiance intensities to measure J-V curves. Moreover, the parameter extraction model could be integrated within the Toolbox system in order to offer the user a more complete experience. At the moment, the user has to adapt the already implemented Matlab® code to their J-V curves dataset.

Experimental measurements

- **Perovskite top cell**: in this study, the variable irradiance/temperature J-V curves utilized in the parameter extraction model ahead of the Electric simulation have been retrieved from previously ASA simulated curves. Although the parameters obtained allow for valid final tandem module energy yield results, it would be more realistic to obtain such J-V curves from an actual physical cell as it's been done for the c-Si bottom cell. Moreover, with the aim of optimizing real-world performance, measurements of J-V curves for cells with different perovskite thicknesses if possible would further increase precision of results. It would in fact get rid of the assumption that all cell parameters remain constant while only the photogenerated current varies at varying thickness, which is a limitation in this study.
- **Irradiance measurements**: it is recommendable to increase the number of irradiance filters employed in the variable irradiance measurements on the c-Si cell. More filters allow for a higher number of J-V curves available for an even more precise parameter extraction process. Possibly, a solar simulator featuring an integrated illumination intensity variation system would serve the purpose. This would also solve some equipment set-up issues (see Appendix C) as well as the error induced by the back-and-forth reflection

between the cell and filter.

- **Spectral variations**: for both variable irradiance and temperature measurements, the illumination spectrum considered is the same throughout the datasets, and it is equal to the WACOM simulator spectrum. It is only scaled down when irradiance filters are placed over the cell. In other words, the ratio between red and blue light content in the spectrum is not varying. To study the tandem's behavior it would be of great importance to have availability of measurements in which such ratio is variable, as it happens in real-world conditions, considering that each sub-cell responds differently when one part of the spectrum is more relevant than the other. This is possible for example when using light sources (such as LED-based simulators) where the spectrum can be varied. This would provide many insights on current mismatching and fill factor effect conditions.

Further steps in tandem energy yield analysis

- **AC yield**: to complete the yield analysis for tandem PV modules applications in real-world conditions, future researchers can study how the optimization and maximization of the performance is influenced when considering the final AC yield of the system. Therefore, after application of AC cabling and inverters. This will also affect the calculations of system performance ratio, which can then be obtained from an AC point of view. The resulting values would be lower than the ones presented in this work and more consistent with typical PV systems PRs.
- **Tandem cell/module**: the cell considered features EVA in the encapsulation. A new type of structure utilizing polyolefin could be implemented in GenPro4 and its behavior simulated. Moreover, the PVMD Toolbox doesn't include any degradation effect on either sub-cell, but particularly the perovskite top cell considering that its durability is currently a major issue in research. Future studies analysing yields over different time spans could look into implementing a degradation effect model to take performance worsening into consideration. Then, this study has only considered 2T tandem architectures. To make this analysis more comprehensive, 4T, 3T and bifacial technology could be considered for tandem energy yield prediction and optimization. Finally, yield predictions with location-specific optimal module tilt angles should be considered and its performance ratio results compared to the standard 27°ones. Solar-tracking systems can also be implemented to further maximize annual energy yield production.
- **Financial analysis**: to justify research on tandem structures, PV systems financial analysis can also be employed. This can be done by looking at the levelized cost of electricity (LCOE). Such parameter also takes into consideration degradation rates for the system, as mentioned before. An LCOE analysis over different world areas and climates and its comparison to established PV technologies can provide useful insights on the future development of tandem modules.

A

Optical properties of reference cells

In the following Tables, the exact values of thicknesses utilised in the GenPro4 optical simulation of the tandem structure are reported. For each layer type, the reference from which the optical characterization was retrieved from (namely, the *n, k* data of the complex refractive index) is also shown. For the single sub-cell simulation carried out and analysed in Chapter 4, the silicon cell implemented on GenPro4 is the same as it is described in the bottom-cell table.

Layer	**Thickness [um]**	**Optical data reference (n,k values)**
MgF_2	0.134	[102]
Glass	3000 (front & back)	[103]
EVA	300 (front & back)	[104]

Table A.1: Layer thicknesses and optical data reference for the front ARC and encapsulation.

Layer	**Thickness [um]**	**Optical data reference (n,k values)**
IZO	0.110	[105]
SnO_2	0.010	[106]
$C60$	0.035	[107]
perovskite	variable	[107]
Spiro-OMeTAD	0.012	[108]
nc-Si (n and p)	0.020	[18]

Table A.2: Layer thicknesses and optical data reference for the top cell.

Layer	**Thickness [um]**	**Optical data reference (n,k values)**
poly-SiO_x (n)	0.030	[18]
c-Si bulk	280	[105]
poly-SiO_x (p)	0.020	[18]
IZO	0.120	[105]
Ag	3	[18]

Table A.3: Layer thicknesses and optical data reference for the bottom cell.

B

Module geometry specifications

The following are the specifications adopted to construct the module geometry ahead of the Module simulation with the PVMD Toolbox through the Lux software. Most of these specifications are taken equal to the default values implemented in the Toolbox, as they are adopted for common module geometries and metallization techniques [109], [110], [111].

Cell rows	12
Cell columns	6
Total number of cells	72
Module thickness	0.5 cm
Cell spacing	0.3 cm
Edge spacing	1 cm
Module tilt	27°
Module azimuth	South = 0°(Rome, Reykjavik), North = 180°(Alice Springs)
Height to ground	50 cm
Module side spacing	100 cm
Module row spacing	800 cm

Cell length	15.675 cm
Cell width	15.675 cm
Cell area	245.7 cm^2
Module area	1.89 m^2
Albedo	0.2
Busbars	3 / cell
Fingers spacing	10 / cm
Busbar thickness	100 um
Fingers thickness	50 um
Bypass diodes	0

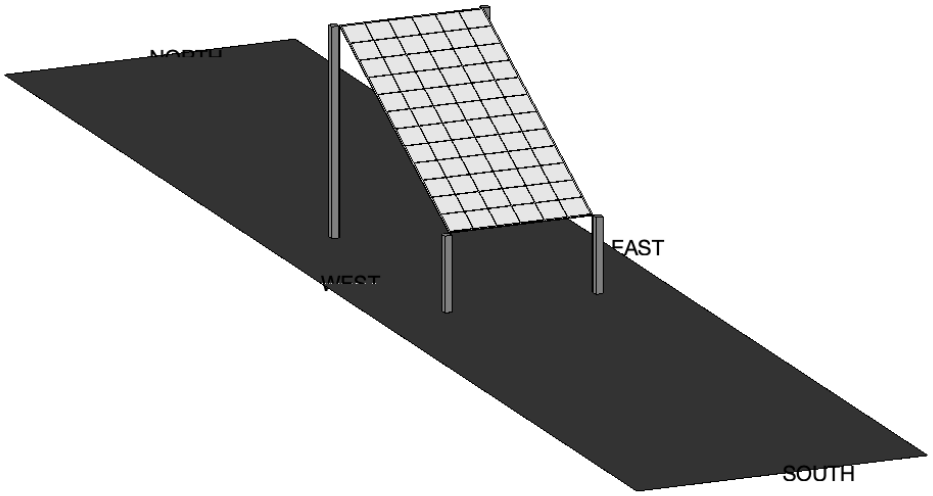

Figure B.1: The digital model of the module as implemented on the Toolbox (south-orientation).

C

Notes on measurements experiment

In this Appendix chapter, the procedure adopted for the measurements experiment with the c-Si poly-SiOx cell produced at TUDelft is briefly described in its practical details. Some recommendations are also provided for future studies that will employ the same measurement methodology.

C.1. General notes

The c-Si cell utilized for this experiment is depicted in the Figure reported in Chapter 3 (Fig. 3.6. It is the number 4 die among the ones printed on the circular silicon wafer, as it is the better performing one. As it can be seen from the picture, the cell is decorated with a white square frame that is the metallization used for front contact of the cell. This metallization collects the current produced in the cell from the line fingers printed over it. Behind the cell, on the bottom side of the wafer, each cell is covered with a white layer of metallization that serves the purpose of back contact. When performing measurements with this type of structure, it is necessary to place the contact arms that are connected to the WACOM stage correctly on each of the two front and back contacts. Ahead of the simulations, it is first necessary to calibrate the WACOM with the 2 reference cells, as explained in Chapter 3. Then, the resistance on the contacts needs to be measured as well to make sure it is at an acceptable value and not too high. Typically, this is in the range between a few hundreds of ohms and 1k ohm. This check is done directly through the LabView GUI.

Obviously, particular care has to be put in placing the contact arms in a way that they don't alter the incident light on the cell. Otherwise, the results would be invalid. Moreover, the rest of the wafer that is not used for measurements (i.e. the other cells and the remaining silicon exposed) have to be covered with black canvases/masks in order to avoid extra photogenerated current to be produced and collected in the measurement. The user should also plan ahead the range of voltage/current that the software will employ to perform the J-V sweep. They have to make sure it is comfortable enough for the maximum value of current to be allowed,

but also for the whole voltage range to be allowed. For a silicon solar cell of these dimensions, typically a range of voltage between 0.8 V and -0.2 V, and a maximum current value of 1 A or 2 A is enough to get good measurements. Finally, the more datapoints the user decides to collect, the more precise the J-V curve will be. It is recommendable to choose this value to be in the few hundreds, as J-V sweep measurements are anyway quite fast with WACOM.

C.2. Temperature measurements notes

As described in Chapter 3, temperature variation measurements are made possible when placing the cell wafer on a gold-plate NIP stage. This stage is temperature controlled by the WACOM's Julabo Cooler, and the plate can vary its temperature through an user-set command sent from the GUI. The maximum allowed temperature is 55℃ while the minimum is 15℃. This has to be taken into account when deciding the range of temperature measurements and number of J-V curves needed. As the variation of temperature takes a quite long time (up to 1 h and half for a 5 degree step), it is recommendable to plan the experiment carefully in order to make it as time-efficient as possible. Typically, it is easier for the plate to be heated up rather than cooled down. One workaround that can be adopted to speed up the process, although quite mechanical, is to turn the controlling PC off and back on again after a few sets of measurements. Apparently, resetting the software helps the WACOM adjust the temperatures to the user-set ones faster this way. The gold-plated stage also has a built-in vacuum function. Its use is highly recommended as it helps the silicon wafer stay in place during setting of the equipment and prevents unwanted modifications in such setting during the handling phase. This improves quality and reproducibility of measurements.

C.3. Irradiance measurements notes

For variable irradiance measurements, the setting is slightly more complicated than for STC or temperature variable measurements. This is because more items need to be employed. Firstly, after placing the silicon wafer on the cell, the irradiance filters 3D printed holder needs to be carefully placed over the cell mask. This procedure is quite delicate as it is necessary to avoid covering any parts of the cell's active area, while not having a great deal of visibility on the cell itself during the movements. Then, the contact arms are inserted through the holes featured in the holder, and again the user has to be careful not to create any shadow on the cell or touch any other unwanted item with the contacts, causing extra resistance in the current collection. When the holder is correctly placed, the filters used can be inserted one by one and the measurements carried out.

Before this however, it is recommendable to run a few J-V sweeps without employing any filter (hence at 1000 W/m^2) and validate the results with the previously obtained STC J-V curves. If the results are sensibly different, it means that something in the equipment used wasn't placed correctly, hence the procedure has to be repeated. It is also recommendable to carefully and delicately clean the irradiance filters with isopropyl alcohol to make sure the surfaces are

free from dust or any other particle.

D

Supplement to measurements experiment

In this Appendix, the functions of external quantum efficiency (EQE) and reflectance of the silicon TOPCon cell adopted in this study are shown as function of the wavelength (Fig. D.1). The measured transmittance of the irradiance filters utilized to gather variable irradiance J-V curves (Chapter 3) are also shown (Fig. D.2). A comparison with another typical filter used for this task is provided, in order to show the accuracy of the polka dots filters in the irradiance scaling effect.

D.1. EQE and reflectance of c-Si TOPCon cell

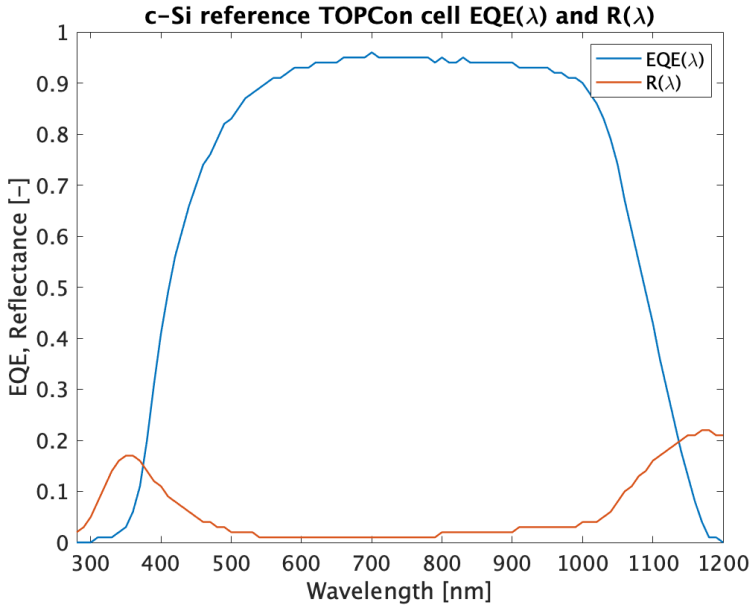

Figure D.1: The measured EQE and reflectance of the single-side textured c-Si TOPCon solar cell featuring poly-SiOx CSPCs, as adopted in this study.

D.2. Transmittance of employed "polka dots" irradiance filters

Below is a plot of the transmittance functions of the filters and the reference ND-filter. The polka dots filters feature a very consistent transmittance function that confirms the intensity value reported on the filter. The 500 W and 800 W filters are however slightly more sensible to lower wavelengths, but we are still within a 1% deviation error so it's very precise. The peak that the transmittance functions feature between 800 and 900 nm is due to an automatic measurement system adjustment that happens in the LAMBDA 1050 machine, hence it can be ignored when using transmittance functions in calculations. The comparison to the 500 W neutral density filter shows the superiority of polka dots filters in terms of irradiance scaling down capabilities. The transmittance of the former is much more wavelength-dependent and it therefore alters the spectrum of the incoming radiation, before it reaches the cell underneath.

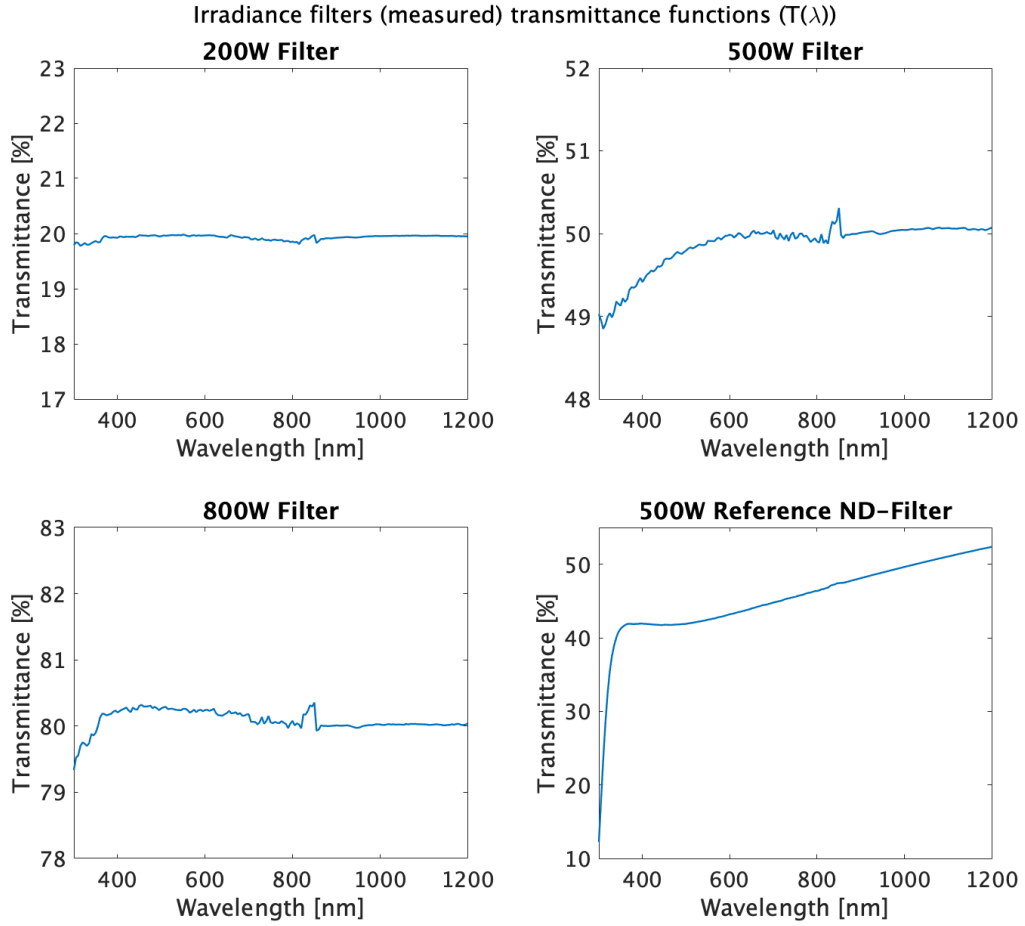

Figure D.2: The transmittance of the 3 irradiance filters (200 W, 500 W, 800 W) utilized to scale down the irradiance while measuring J-V curves with the WACOM solar simulator. As a comparison, a 50% neutral density filter transmittance has also been measured and reported here. The latter features a much more wavelength-dependent transmittance function, sensibly varying at lower wavelengths.

E

Supplement to simulation results

For ease of representation, some results of the tandem structure with the PVMD Toolbox have not been shown for all three locations considered within the previous Chapters. Although this doesn't affect validity of the analysis of the device performance as carried out in the report, in this Appendix some further results of the energy yield simulations location-specific results have been reported.

E.1. Thermal simulation

The following graphs represent the yearly module temperature variations in the locations of Reykjavik (Figure E.1) and Alice Springs (Figure E.2), in addition to the Rome graph shown in Chapter 2.

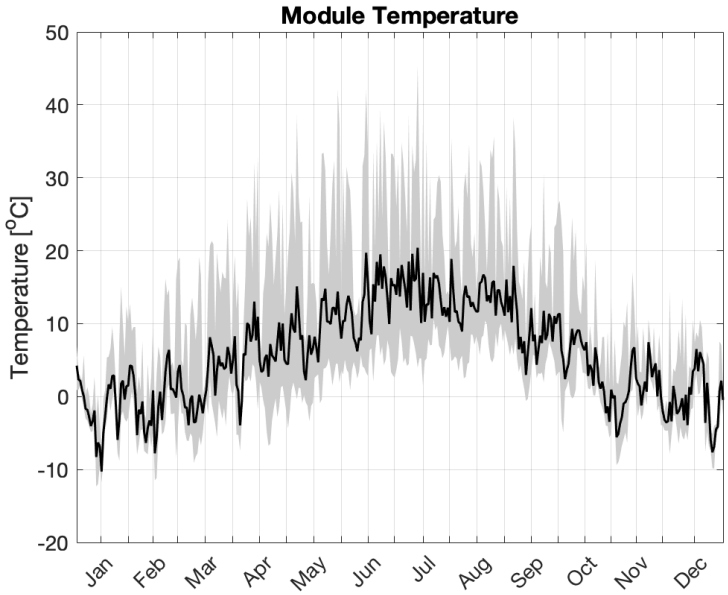

Figure E.1: Module average daily temperature in Reykjavik.

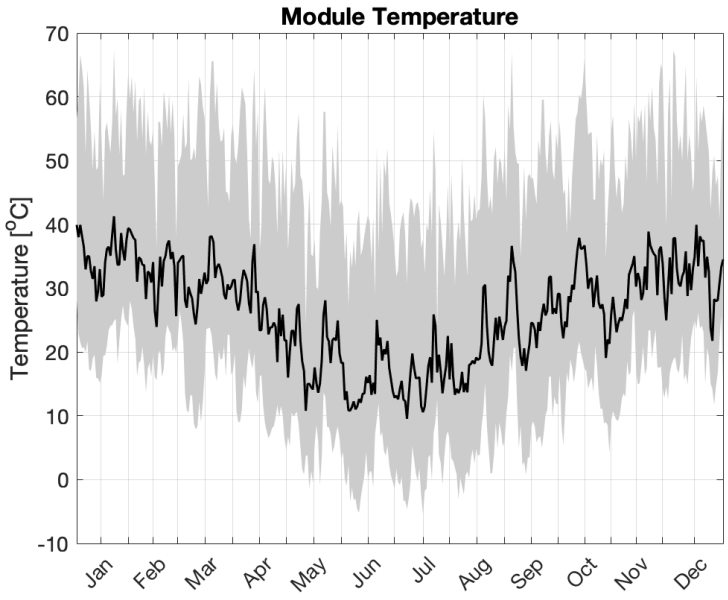

Figure E.2: Module daily average temperature in Alice Springs.

E.2. Energy yield simulation

The plots in this section are a simulation output of the Electric model in the Toolbox. They represent the daily DC yield and irradiation for each of the three locations.

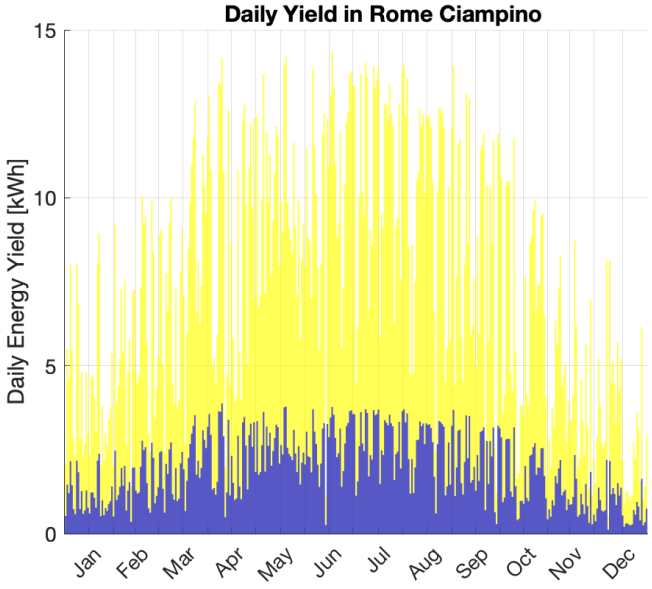

Figure E.3: Module daily yield in Rome Ciampino.

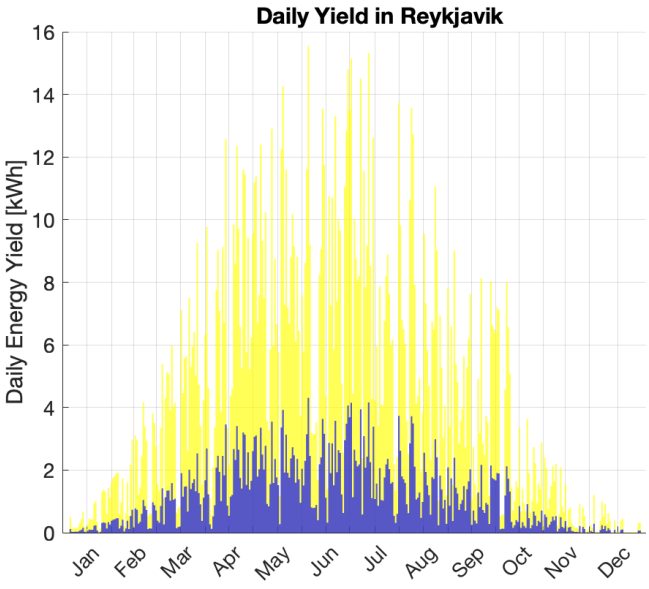

Figure E.4: Module daily yield in Reykjavik.

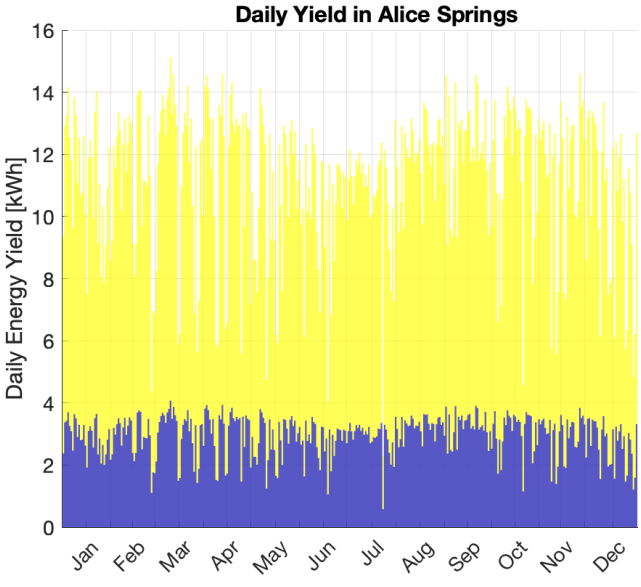

Figure E.5: Module daily yield in Alice Springs.

References

[1] Wallace S. Broecker. "Climatic Change: Are We on the Brink of a Pronounced Global Warming?" In: *New Series* 189 (4201 1975), pp. 460–463.

[2] National Aeronautics and Space Administration. "What's in a Name? Global Warming vs. Climate Change". In: (). URL: https://www.nasa.gov/topics/earth/features/climate_by_any_other_name.html.

[3] U.S. Environmental Protection Agency. "Sources of Greenhouse Gas Emissions | US EPA". In: (). URL: https://www.epa.gov/ghgemissions/sources-greenhouse-gas-emissions.

[4] U.S. Environmental Protection Agency. "Climate Change Indicators: Greenhouse Gases | US EPA". In: (). URL: https://www.epa.gov/climate-indicators/greenhouse-gases.

[5] International Energy Agency. "Global Energy Review 2021 Analysis - IEA". In: (). URL: https://www.iea.org/reports/global-energy-review-2021?mode=overview.

[6] Richard Perez and Marc Perez. "A fundamental look at energy reserves for the planet". In: 50 (Jan. 2009).

[7] David Chandler. "Shining brightly | MIT News | Massachusetts Institute of Technology". In: (). URL: https://news.mit.edu/2011/energy-scale-part3-1026.

[8] SolarPower Europe. "Global Market Outlook For Solar Power". In: (2021). URL: https://www.solarpowereurope.org/insights/market-outlooks/global-market-outlook-for-solar-power.

[9] David Feldman et al. *U.S. Solar Photovoltaic System and Energy Storage Cost Benchmark: Q1 2020*. 2020. URL: www.nrel.gov/publications..

[10] Britannica. "silicon | Element, Atom, Properties, Uses & Facts | Britannica". In: (). URL: https://www.britannica.com/science/silicon.

[11] Jason Svarc. "Most efficient solar panels 2022 Clean Energy Reviews". In: (). URL: https://www.cleanenergyreviews.info/blog/most-efficient-solar-panels.

[12] Jianhua Zhao, Aihua Wang, and Martin Green. "High-efficiency PERL and PERT silicon solar cells on FZ and MCZ substrates". In: *Solar Energy Materials and Solar Cells* 65 (Jan. 2001), pp. 429–435. DOI: 10.1016/S0927-0248(00)00123-9.

[13] National Renewable Energy Laboratory. "Best Research-Cell Efficiency Chart | Photovoltaic Research | NREL". In: (). URL: https://www.nrel.gov/pv/cell-efficiency.html.

[14] Kunta Yoshikawa et al. “Silicon heterojunction solar cell with interdigitated back contacts for a photoconversion efficiency over 26%”. In: *Nature Energy* 2 (Mar. 2017), p. 17032. DOI: 10.1038/nenergy.2017.32.

[15] C. E. Chan, B. J. Hallam, and S. R. Wenham. “Simplified interdigitated back contact solar cells”. In: *Energy Procedia* 27 (2012), pp. 543–548. ISSN: 18766102. DOI: 10.1016/J.EGYPRO.2012.07.107. URL: www.sciencedirect.com.

[16] Yuqiang Liu et al. “High-Efficiency Silicon Heterojunction Solar Cells: Materials, Devices and Applications”. In: *Materials Science and Engineering R: Reports* 142 (Oct. 2020). ISSN: 0927796X. DOI: 10.1016/J.MSER.2020.100579. URL: https://doi.org/10.1016/j.mser.2020.100579.

[17] F Feldmann et al. “A Passivated Rear Contact For High-Efficiency n-Type Silicon Solar Cells Enabling High Voc and FF>82%”. In: (2013).

[18] Manvika Singh et al. “Comparing optical performance of a wide range of perovskite/silicon tandem architectures under real-world conditions”. In: *Nanophotonics* 10 (8 June 2021), pp. 2043–2057. ISSN: 21928614. DOI: 10.1515/NANOPH-2020-0643/ASSET/GRAPHIC/J_NANOPH-2020-0643_FIG_010.JPG. URL: https://www.degruyter.com/document/doi/10.1515/nanoph-2020-0643/html.

[19] Solar Builder. “JinkoSolar topped its world record for TOPcon solar cell efficiency | Solar Builder”. In: (). URL: https://solarbuildermag.com/news/jinkosolar-topped-its-world-record-for-topcon-solar-cell-efficiency/.

[20] Fraunhofer Institute for Solar Energy Systems. “TOPCon Overcoming Fundamental Bottlenecks to a New World-Record Silicon Solar Cell - Fraunhofer ISE”. In: (). URL: https://www.ise.fraunhofer.de/en/research-projects/topcon.html.

[21] William Shockley and Hans J. Queisser. “Detailed Balance Limit of Efficiency of p-n Junction Solar Cells”. In: *Journal of Applied Physics* 32.3 (Mar. 1961), pp. 510–519. DOI: 10.1063/1.1736034.

[22] Armin Richter, Martin Hermle, and Stefan Glunz. “Reassessment of the Limiting Efficiency for Crystalline Silicon Solar Cells”. In: *IEEE Journal of Photovoltaics* 3 (July 2013), pp. 1184–1191. DOI: 10.1109/JPHOTOV.2013.2270351.

[23] Armin Richter et al. “n-Type Si solar cells with passivating electron contact: Identifying sources for efficiency limitations by wafer thickness and resistivity variation”. In: *Solar Energy Materials and Solar Cells* 173 (Dec. 2017), pp. 96–105. ISSN: 0927-0248. DOI: 10.1016/J.SOLMAT.2017.05.042.

[24] Martin A. Green et al. “Solar cell efficiency tables (Version 58)”. In: *Progress in Photovoltaics: Research and Applications* 29 (7 July 2021), pp. 657–667. ISSN: 1099-159X. DOI: 10.1002/PIP.3444. URL: https://onlinelibrary.wiley.com/doi/full/10.1002/pip.3444%20https://onlinelibrary.wiley.com/doi/abs/10.1002/pip.3444%20https://onlinelibrary.wiley.com/doi/10.1002/pip.3444.

[25] Ashwith Chilvery et al. “A perspective on the recent progress in solution-processed methods for highly efficient perovskite solar cells”. In: *Science and Technology of Advanced Materials* 17 (1 Jan. 2016), pp. 650–658. ISSN: 18785514. DOI: 10.1080/14686996.2016.1226120.

[26] Minu Mohan. “Perovskite photovoltaics”. In: *Perovskite Photovoltaics: Basic to Advanced Concepts and Implementation* (Jan. 2018), pp. 447–480. DOI: 10.1016/B978-0-12-812915-9.00014-9.

[27] Stefaan De Wolf et al. “Organometallic Halide Perovskites: Sharp Optical Absorption Edge and Its Relation to Photovoltaic Performance”. In: (2000). DOI: 10.1021/jz500279b. URL: https://pubs.acs.org/sharingguidelines.

[28] Sayantan Mazumdar, Ying Zhao, and Xiaodan Zhang. “Stability of Perovskite Solar Cells: Degradation Mechanisms and Remedies”. In: *Frontiers in Electronics* 0 (Aug. 2021), p. 8. ISSN: 2673-5857. DOI: 10.3389/FELEC.2021.712785.

[29] Bin Chen et al. “A critical review on the moisture stability of halide perovskite films and solar cells”. In: *Chemical Engineering Journal* 430 (Feb. 2022), p. 132701. ISSN: 1385-8947. DOI: 10.1016/J.CEJ.2021.132701.

[30] Casey Crownhart. “Can the most exciting new solar material live up to its hype? | MIT Technology Review”. In: (). URL: https://www.technologyreview.com/2021/06/29/1027451/perovskite-solar-panels-hype-commercial-debut/.

[31] Arno Smets et al. *Solar Energy: The physics and engineering of photovoltaic conversion, technologies and systems*. English. UIT Cambridge Limited, 2016. ISBN: 978-1-906860-32-5.

[32] A. De Vos. “Detailed balance limit of the efficiency of tandem solar cells”. In: *Journal of Physics D: Applied Physics* 13 (5 May 1980), p. 839. ISSN: 0022-3727. DOI: 10.1088/0022-3727/13/5/018. URL: https://iopscience.iop.org/article/10.1088/0022-3727/13/5/018%20https://iopscience.iop.org/article/10.1088/0022-3727/13/5/018/meta.

[33] Giles E. Eperon, Maximilian T. Hörantner, and Henry J. Snaith. “Metal halide perovskite tandem and multiple-junction photovoltaics”. In: *Nature Reviews Chemistry 2017 1:12* 1 (12 Nov. 2017), pp. 1–18. ISSN: 2397-3358. DOI: 10.1038/s41570-017-0095. URL: https://www.nature.com/articles/s41570-017-0095.

[34] Erkan Aydin et al. “Interplay between temperature and bandgap energies on the outdoor performance of perovskite/silicon tandem solar cells”. In: *Nature Energy* 5 (11 Nov. 2020), pp. 851–859. ISSN: 20587546. DOI: 10.1038/S41560-020-00687-4.

[35] P. Faine et al. “The influence of spectral solar irradiance variations on the performance of selected single-junction and multijunction solar cells”. In: *Solar Cells* 31 (3 June 1991), pp. 259–278. ISSN: 0379-6787. DOI: 10.1016/0379-6787(91)90027-M.

[36] Niraj N. Lal et al. “Perovskite Tandem Solar Cells”. In: *Advanced Energy Materials* 7 (18 Sept. 2017). ISSN: 16146840. DOI: 10.1002/AENM.201602761.

[37] Emily L. Warren et al. “Maximizing tandem solar cell power extraction using a three-terminal design”. In: *Sustainable Energy and Fuels* 2 (6 2018), pp. 1141–1147. ISSN: 23984902. DOI: 10.1039/C8SE00133B.

[38] Xingliang Li et al. “Silicon heterojunction-based tandem solar cells: Past, status, and future prospects”. In: *Nanophotonics* 10 (8 June 2021), pp. 2001–2022. ISSN: 21928614. DOI: 10.1515/NANOPH-2021-0034.

[39] Florent Sahli et al. “Fully textured monolithic perovskite/silicon tandem solar cells with 25.2% power conversion efficiency”. In: *Nature Materials 2018 17:9* 17 (9 June 2018), pp. 820–826. ISSN: 1476-4660. DOI: 10.1038/s41563-018-0115-4. URL: https://www.nature.com/articles/s41563-018-0115-4.

[40] Manoj Jaysankar et al. “Four-Terminal Perovskite/Silicon Multijunction Solar Modules”. In: *Advanced Energy Materials* 7 (15 Aug. 2017), p. 1602807. ISSN: 1614-6840. DOI: 10.1002/AENM.201602807. URL: https://onlinelibrary.wiley.com/doi/full/10.1002/aenm.201602807%20https://onlinelibrary.wiley.com/doi/abs/10.1002/aenm.201602807%20https://onlinelibrary.wiley.com/doi/10.1002/aenm.201602807.

[41] Stephanie Essig et al. “Raising the one-sun conversion efficiency of IIIV/Si solar cells to 32.8% for two junctions andă35.9% for three junctions”. In: *Nature Energy 2017 2:9* 2 (9 Aug. 2017), pp. 1–9. ISSN: 2058-7546. DOI: 10.1038/nenergy.2017.144. URL: https://www.nature.com/articles/nenergy2017144.

[42] Yuqiang Liu et al. “High-Efficiency Silicon Heterojunction Solar Cells: Materials, Devices and Applications”. In: *Materials Science and Engineering R: Reports* 142 (Oct. 2020). ISSN: 0927796X. DOI: 10.1016/J.MSER.2020.100579.

[43] Yiliang Wu et al. “Monolithic perovskite/silicon-homojunction tandem solar cell with over 22% efficiency”. In: *Energy & Environmental Science* 10 (11 Nov. 2017), pp. 2472–2479. ISSN: 1754-5706. DOI: 10.1039/C7EE02288C. URL: https://pubs.rsc.org/en/content/articlehtml/2017/ee/c7ee02288c%20https://pubs.rsc.org/en/content/articlelanding/2017/ee/c7ee02288c.

[44] Armin Richter et al. “Tunnel oxide passivating electron contacts as full-area rear emitter of high-efficiency p-type silicon solar cells”. In: *Progress in Photovoltaics: Research and Applications* 26 (8 Aug. 2018), pp. 579–586. ISSN: 1099-159X. DOI: 10.1002/PIP.2960. URL: https://onlinelibrary.wiley.com/doi/full/10.1002/pip.2960%20https://onlinelibrary.wiley.com/doi/abs/10.1002/pip.2960%20https://onlinelibrary.wiley.com/doi/10.1002/pip.2960.

[45] Fabian Wagner. *MSc Thesis. Fabrication of high temperature carrier-selective passivating contact solar cells for application in monolithic perovskite/c-Si tandem devices.* 2022. URL: http://resolver.tudelft.nl/uuid:07802aad-4c8e-428f-9d90-eb5466829e1c.

[46] Sino Voltaics. “Standard Test Conditions (STC): definition and problems”. In: (). URL: https://sinovoltaics.com/learning-center/quality/standard-test-conditions-stc-definition-and-problems/.

[47] Maximilian T. Hörantner and Henry J. Snaith. "Predicting and optimising the energy yield of perovskite-on-silicon tandem solar cells under real world conditions". In: *Energy & Environmental Science* 10 (9 Sept. 2017), pp. 1983–1993. ISSN: 1754-5706. DOI: 10.1039/C7EE01232B. URL: https://pubs.rsc.org/en/content/articlehtml/2017/ee/c7ee01232b%20https://pubs.rsc.org/en/content/articlelanding/2017/ee/c7ee01232b.

[48] Haohui Liu et al. "A Worldwide Theoretical Comparison of Outdoor Potential for Various Silicon-Based Tandem Module Architecture". In: *Cell Reports Physical Science* 1 (4 Apr. 2020), p. 100037. ISSN: 2666-3864. DOI: 10.1016/J.XCRP.2020.100037.

[49] M. Villoz and A. Mermoud. "PVsyst Logiciel Photovoltaïque". In: (). URL: https://www.pvsyst.com/.

[50] Nate Blair et al. "System Advisor Model (SAM) General Description (Version 2017.9.5)". In: (2018). URL: www.nrel.gov/publications..

[51] HOMER Energy. "Welcome to HOMERUL Logo". In: (). URL: https://www.homerenergy.com/products/pro/docs/latest/index.html.

[52] Technische Universiteit Delft - SolarUrban. "Comprehensive PV Systems Modelling Toolbox". In: (). URL: https://www.tudelft.nl/solarurban/research/projects/comprehensive-pv-systems-modelling-toolbox.

[53] Rudi Santbergen et al. "GenPro4 Optical Model for Solar Cell Simulation and Its Application to Multijunction Solar Cells". In: *IEEE Journal of Photovoltaics* 7 (3 May 2017), pp. 919–926. ISSN: 21563381. DOI: 10.1109/JPHOTOV.2017.2669640.

[54] K. Jäger et al. "A scattering model for nano-textured interfaces and its application in opto-electrical simulations of thin-film silicon solar cells". In: *Journal of Applied Physics* 111 (8 Apr. 2012), p. 083108. ISSN: 0021-8979. DOI: 10.1063/1.4704372. URL: https://aip.scitation.org/doi/abs/10.1063/1.4704372.

[55] R. Santbergen et al. "Calculation of irradiance distribution on PV modules by combining sky and sensitivity maps". In: *Solar Energy* 150 (July 2017), pp. 49–54. ISSN: 0038-092X. DOI: 10.1016/J.SOLENER.2017.04.036.

[56] Zidan Wang. *Improvements and Experimental Validation of the PVMD Toolbox-an Energy Yield Prediction Model for PV Systems*. URL: http://repository.tudelft.nl/..

[57] R. Perez, R. Seals, and J. Michalsky. "All-weather model for sky luminance distribution-Preliminary configuration and validation". In: *Solar Energy* 50 (3 Mar. 1993), pp. 235–245. ISSN: 0038-092X. DOI: 10.1016/0038-092X(93)90017-I.

[58] E Garcia Goma. *Development of Cell to System Annual Energy Yield Toolbox for Bifacial Modules*. 2018. URL: http://repository.tudelft.nl/..

[59] M. R. Vogt et al. *Manuscript in Preparation*. 2022.

[60] Abdallah Nour and El Din. *Improved Electrical Model and Experimental Validation of the PVMD Toolbox Extending the Energy Yield Prediction Model to Tandem PV Modules*. URL: http://repository.tudelft.nl/..

[61] Mahesh Jayan. *MSc Thesis. Energy yield simulations of perovskite/c-Si tandem modules in real-world conditions*. 2021. URL: http://resolver.tudelft.nl/uuid:07802aad-4c8e-428f-9d90-eb5466829e1c.

[62] Na Liu et al. "Recent Progress in Developing Monolithic Perovskite/Si Tandem Solar Cells". In: *Frontiers in Chemistry* 8 (Dec. 2020), p. 1120. ISSN: 22962646. DOI: 10.3389/FCHEM.2020.603375/BIBTEX.

[63] PV Education.org. "Mismatch for Cells Connected in series | PVEducation". In: (). URL: https://www.pveducation.org/pvcdrom/modules-and-arrays/mismatch-for-cells-connected-in-series.

[64] "Matching of silicon thin-film tandem solar cells for maximum power output". In: *International Journal of Photoenergy* 2013 (2013). ISSN: 1110662X. DOI: 10.1155/2013/314097.

[65] Baojie Yan et al. "Correlation of current mismatch and fill factor in amorphous and nanocrystalline silicon based high efficiency multi-junction solar cells". In: *Conference Record of the IEEE Photovoltaic Specialists Conference* (2008). ISSN: 01608371. DOI: 10.1109/PVSC.2008.4922607.

[66] Rongrong Cheacharoen et al. "Encapsulating perovskite solar cells to withstand damp heat and thermal cycling Journal: Sustainable Energy & Fuels Title: Encapsulating perovskite solar cells to withstand damp heat and thermal cycling". In: ().

[67] PV Education.org. "Anti-Reflection Coatings | PVEducation". In: (). URL: https://www.pveducation.org/pvcdrom/design-of-silicon-cells/anti-reflection-coatings.

[68] Farzaneh Ahangarani Farahani et al. "Enhancement in Power Conversion Efficiency of CdS Quantum Dot Sensitized Solar Cells Through a Decrease in Light Reflection The International Occultation Timing Association Middle East section, Iran". In: ().

[69] M. Singh et al. "Supplementary information for: Comparing optical performance of a wide range of perovskite / silicon tandem architectures under real world conditions". In: ().

[70] Florent Sahli et al. "Fully textured monolithic perovskite/silicon tandem solar cells with 25.2% power conversion efficiency". In: *Nature Materials 2018 17:9* 17 (9 June 2018), pp. 820–826. ISSN: 1476-4660. DOI: 10.1038/s41563-018-0115-4. URL: https://www.nature.com/articles/s41563-018-0115-4.

[71] Dong Zhang et al. "High efficiency 4-terminal perovskite/c-Si tandem cells". In: *Solar Energy Materials and Solar Cells* 188 (Dec. 2018), pp. 1–5. ISSN: 0927-0248. DOI: 10.1016/J.SOLMAT.2018.07.032.

[72] Florine M. Rombach, Saif A. Haque, and Thomas J. Macdonald. "Lessons learned from spiro-OMeTAD and PTAA in perovskite solar cells". In: *Energy & Environmental Science* 14 (10 Oct. 2021), pp. 5161–5190. ISSN: 1754-5706. DOI: 10.1039/D1EE02095A. URL: https://pubs.rsc.org/en/content/articlehtml/2021/ee/d1ee02095a%20https://pubs.rsc.org/en/content/articlelanding/2021/ee/d1ee02095a.

[73] Jérémie Werner et al. “Sputtered rear electrode with broadband transparency for perovskite solar cells”. In: *Solar Energy Materials and Solar Cells* 141 (June 2015), pp. 407–413. ISSN: 0927-0248. DOI: 10.1016/J.SOLMAT.2015.06.024. URL: https://research.utwente.nl/en/publications/sputtered-rear-electrode-with-broadband-transparency-for-perovski.

[74] Solargis. “Global Solar Atlas”. In: (). URL: https://globalsolaratlas.info/map.

[75] Photovoltaic Materials and Devices TUDelft. “ASA Software”. In: (). URL: https://www.tudelft.nl/ewi/over-de-faculteit/afdelingen/electrical-sustainable-energy/photovoltaic-materials-and-devices/software-platform/asa-software.

[76] Isabel Mesquita, Luísa Andrade, and Adélio Mendes. “Temperature Impact on Perovskite Solar Cells Under Operation”. In: *ChemSusChem* 12 (10 May 2019), pp. 2186–2194. ISSN: 1864564X. DOI: 10.1002/CSSC.201802899.

[77] Erkan Aydin et al. “Interplay between temperature and bandgap energies on the outdoor performance of perovskite/silicon tandem solar cells”. In: *Nature Energy 2020 5:11* 5 (11 Sept. 2020), pp. 851–859. ISSN: 2058-7546. DOI: 10.1038/s41560-020-00687-4. URL: https://www.nature.com/articles/s41560-020-00687-4.

[78] Qi Meng et al. “Effect of temperature on the performance of perovskite solar cells”. In: *Journal of Materials Science: Materials in Electronics 2020 32:10* 32 (10 Feb. 2020), pp. 12784–12792. ISSN: 1573-482X. DOI: 10.1007/S10854-020-03029-Y. URL: https://link.springer.com/article/10.1007/s10854-020-03029-y.

[79] Taylor Moot et al. “Temperature Coefficients of Perovskite Photovoltaics for Energy Yield Calculations”. In: *ACS Energy Letters* 6 (5 May 2021), pp. 2038–2047. ISSN: 23808195. DOI: 10.1021/ACSENERGYLETT.1C00748/SUPPL_FILE/NZ1C00748_SI_001.PDF. URL: https://pubs.acs.org/doi/abs/10.1021/acsenergylett.1c00748.

[80] Worldwide Technology Co. Ltd Shangai. “WACOM Solar Simulator”. In: (). URL: http://www.worldwide-china.com/en/productDetails.php?serial=157.

[81] Futurasun. “What is the temperature coefficient of solar panels”. In: (). URL: https://www.futurasun.com/en/temperature-coefficient/.

[82] Sinovoltaics. “Measuring the temperature coefficient of a PV module”. In: (). URL: https://sinovoltaics.com/solar-basics/measuring-the-temperature-coefficients-of-a-pv-module/.

[83] JinkoSolar. “TOPCon- Preferred in high temperature areas”. In: *PV Magazine International* (). URL: https://www.pv-magazine.com/press-releases/preferred-in-high-temperature-areas-jinkosolar-tiger-neo-series/.

[84] ACDC Research Group. “Research on Temperature Coefficient of PV devices”. In: *University of New South Wales* (). URL: https://www.acdc-pv-unsw.com/research-temperature-coefficient.

[85] W. Li et al. “Six-parameter electrical model for photovoltaic cell/module with compound parabolic concentrator”. In: *Solar Energy* 137 (Nov. 2016), pp. 551–563. ISSN: 0038-092X. DOI: 10.1016/J.SOLENER.2016.08.050.

[86] Amit Jain and Avinashi Kapoor. “Exact analytical solutions of the parameters of real solar cells using Lambert W-function”. In: *Solar Energy Materials and Solar Cells* 81 (2 Feb. 2004), pp. 269–277. ISSN: 0927-0248. DOI: 10.1016/J.SOLMAT.2003.11.018.

[87] Youri Blom. *MSc Thesis. Energy loss analysis of tandem PV modules under realistic operating conditions*. 2022. URL: http://resolver.tudelft.nl/uuid:07802aad-4c8e-428f-9d90-eb5466829e1c.

[88] A. De Vos. “Detailed balance limit of the efficiency of tandem solar cells”. In: *Journal of Physics D: Applied Physics* 13 (5 May 1980), p. 839. ISSN: 0022-3727. DOI: 10.1088/0022-3727/13/5/018. URL: https://iopscience.iop.org/article/10.1088/0022-3727/13/5/018%20https://iopscience.iop.org/article/10.1088/0022-3727/13/5/018/meta.

[89] Franz Urbach. “The Long-Wavelength Edge of Photographic Sensitivity and of the Electronic Absorption of Solids”. In: *Physical Review* 92 (5 Dec. 1953), p. 1324. ISSN: 0031899X. DOI: 10.1103/PhysRev.92.1324. URL: https://journals.aps.org/pr/abstract/10.1103/PhysRev.92.1324.

[90] Ingrid Haedrich et al. “Minimizing the optical cell-to-module losses for MWT-modules”. In: *Energy Procedia* 38 (2013), pp. 355–361. DOI: 10.1016/j.egypro.2013.07.289. URL: www.sciencedirect.com.

[91] Jeff Shepard. *Cell-to-Module Losses Key to Improving PV Efficiencies - News*. 2016. URL: https://eepower.com/news/cell-to-module-losses-key-to-improving-pv-efficiencies/.

[92] Eike Köhnen et al. “Highly efficient monolithic perovskite silicon tandem solar cells: analyzing the influence of current mismatch on device performance”. In: *Sustainable Energy & Fuels* 3 (8 July 2019), pp. 1995–2005. ISSN: 2398-4902. DOI: 10.1039/C9SE00120D. URL: https://pubs.rsc.org/en/content/articlehtml/2019/se/c9se00120d%20https://pubs.rsc.org/en/content/articlelanding/2019/se/c9se00120d.

[93] Hasnain Yousuf et al. “A Review on TOPCon Solar Cell Technology”. In: *Current Photovoltaic Research* 9 (3 2021), pp. 2288–3274. DOI: 10.21218/CPR.2021.9.3.075. URL: https://doi.org/10.21218/CPR.2021.9.3.075.

[94] Hukseflux. “How to calculate PV performance ratio and performance index”. In: (). URL: https://www.hukseflux.com/applications/solar-energy-pv-system-performance-monitoring/how-to-calculate-pv-performance-ratio.

[95] Nils H. Reich et al. “Performance ratio revisited: is PR>90% realistic?” In: *Progress in Photovoltaics: Research and Applications* 20 (6 Sept. 2012), pp. 717–726. ISSN: 1099-159X. DOI: 10.1002/PIP.1219. URL: https://onlinelibrary.wiley.com/doi/full/10.1002/pip.1219%20https://onlinelibrary.wiley.com/doi/abs/10.1002/pip.1219%20https://onlinelibrary.wiley.com/doi/10.1002/pip.1219.

[96] Fraunhofer Institute of Solar Energy Systems. “Photovoltaics Report”. In: (). URL: www.ise.fraunhofer.de.

[97] Antonio Parretta, Angelo Sarno, and Luciano R.M. Vicari. “Effects of solar irradiation conditions on the outdoor performance of photovoltaic modules”. In: *Optics Communications* 153 (1-3 July 1998), pp. 153–163. ISSN: 00304018. DOI: 10.1016/S0030-4018(98)00192-8.

[98] K. Bücher. “Site dependence of the energy collection of PV modules”. In: *Solar Energy Materials and Solar Cells* 47 (1-4 Oct. 1997), pp. 85–94. ISSN: 0927-0248. DOI: 10.1016/S0927-0248(97)00028-7.

[99] Makrides George et al. “Performance assessment of different photovoltaic systems under identical field conditions of high irradiation”. In: *PV RES Conference* (2007). URL: https://www.researchgate.net/publication/256080198_Performance_assessment_of_different_photovoltaic_systems_under_identical_field_conditions_of_high_irradiation.

[100] Solar Mango. “Performance Ratio of Solar Power Plant - Definition, Glossary, Details”. In: (). URL: https://www.solarmango.com/dictionary/performance-ratio/.

[101] Giles E. Eperon et al. “Perovskite-perovskite tandem photovoltaics with optimized band gaps”. In: *Science* 354 (6314 Nov. 2016), pp. 861–865. ISSN: 10959203. DOI: 10.1126/SCIENCE.AAF9717.

[102] Marilyn J. Dodge. “Refractive properties of magnesium fluoride”. In: *Applied Optics, Vol. 23, Issue 12, pp. 1980-1985* 23 (12 June 1984), pp. 1980–1985. ISSN: 2155-3165. DOI: 10.1364/AO.23.001980. URL: https://opg.optica.org/viewmedia.cfm?uri=ao-23-12-1980%5C&seq=0%5C&html=true%20https://opg.optica.org/abstract.cfm?uri=ao-23-12-1980%20https://opg.optica.org/ao/abstract.cfm?uri=ao-23-12-1980.

[103] Malte R. Vogt et al. “Measurement of the Optical Constants of Soda-Lime Glasses in Dependence of Iron Content and Modeling of Iron-Related Power Losses in Crystalline Si Solar Cell Modules”. In: *undefined* 6 (1 Jan. 2016), pp. 111–118. ISSN: 21563381. DOI: 10.1109/JPHOTOV.2015.2498043.

[104] Malte R. Vogt et al. “Optical Constants of UV Transparent EVA and the Impact on the PV Module Output Power under Realistic Irradiation”. In: *Energy Procedia* 92 (Aug. 2016), pp. 523–530. ISSN: 18766102. DOI: 10.1016/J.EGYPRO.2016.07.136.

[105] Jérémie Werner et al. “Sputtered rear electrode with broadband transparency for perovskite solar cells”. In: *Solar Energy Materials and Solar Cells* 141 (June 2015), pp. 407–413. ISSN: 0927-0248. DOI: 10.1016/J.SOLMAT.2015.06.024. URL: https://research.utwente.nl/en/publications/sputtered-rear-electrode-with-broadband-transparency-for-perovski.

[106] Rudi Santbergen et al. “Optimization of Three-Terminal Perovskite/Silicon Tandem Solar Cells”. In: *IEEE Journal of Photovoltaics* 9 (2 Mar. 2019), pp. 446–451. ISSN: 2156-3381. DOI: 10.1109/JPHOTOV.2018.2888832. URL: https://research.tudelft.nl/en/publications/optimization-of-three-terminal-perovskitesilicon-tandem-solar-cel.

[107] Dong Zhang et al. “High efficiency 4-terminal perovskite/c-Si tandem cells”. In: *Solar Energy Materials and Solar Cells* 188 (Dec. 2018), pp. 1–5. ISSN: 09270248. DOI: 10.1016/J.SOLMAT.2018.07.032.

[108] Bjoern Niesen et al. “CH3NH3PbI3 perovskite / silicon tandem solar cells: characterization based optical simulations”. In: *Optics Express, Vol. 23, Issue 7, pp. A263-A278* 23 (7 Apr. 2015), A263–A278. ISSN: 1094-4087. DOI: 10.1364/OE.23.00A263. URL: https://opg.optica.org/viewmedia.cfm?uri=oe-23-7-A263%5C&seq=0%5C&html=true%20https://opg.optica.org/abstract.cfm?uri=oe-23-7-A263%20https://opg.optica.org/oe/abstract.cfm?uri=oe-23-7-A263.

[109] Institution of Engineering and Technology. “Silicon Solar Cell Metallization and Module Technology”. In: *Silicon Solar Cell Metallization and Module Technology* (Dec. 2021). DOI: 10.1049/PBPO174E.

[110] Wonje Oh et al. “Metallization of crystalline silicon solar cells for shingled photovoltaic module application”. In: *Solar Energy* 195 (Jan. 2020), pp. 527–535. ISSN: 0038092X. DOI: 10.1016/J.SOLENER.2019.11.095.

[111] Guy Beaucarne et al. “Summary of the 8th Workshop on Metallization and Interconnection for Crystalline Silicon Solar Cells”. In: 2156 (2019), p. 10001. DOI: 10.1063/1.5125866. URL: https://doi.org/10.1063/1.5125866.